

ABSTRACT

DINOVA, VINCENT ANTHONY. Automated Variable Selection of Gamma-Ray Spectra by Utilization of LASSO and Elastic Net Techniques for Use in Nuclear Security Applications. (Under the direction of Dr. Robin Gardner).

In the aftermath of the disasters of September 11th, 2001, new security measures were taken to prevent future attacks. Due to the extreme destructive physical and psychological power of nuclear weapons and radiation dispersal devices, a large effort has been spent in preventing the proliferation of nuclear weapons and materials. Soft targets, such as oil well logging radiochemical sources, have been identified as a commonly used radioactive source that can be replaced by non-active sources such as D-T or D-D pulsed neutron generators.

An experiment at Kansas State University was conducted, using a D-T pulsed neutron generator and test facility to replicate different scenarios commonly found in oil wells. D-T pulsed neutron generators have the ability to generate neutrons at a comparable rate to AmBe and Cf-252 neutron sources. These neutrons then bombard surrounding materials to release gamma rays by inelastic scattering and absorption commonly referred to as prompt gamma neutron activation analysis. D-T pulsed neutron generators produce neutrons at a higher energy than traditional sources, allowing for additional inelastic scattering schemes to be unlocked. Additionally, pulse timing sequences can be manipulated utilizing a digitizer to separate prompt and delayed responses.

This dissertation is devoted to investigating new supervised machine learning algorithms, LASSO and Elastic Net, that are used to automatically perform variable selection and model prediction. MCNP generated libraries are simulated to estimate the detector response using the geometry and material composition of the tool, testing chamber, and surrounding materials and compared to experiments performed at Kansas State University.

During the preliminary work on the oil well logging application, it was discovered that the same techniques could be used as an aid in radioisotope identification devices (RIIDs). Handheld RIIDs are used by first responders and radiation safety personnel to identify radioactive materials found in situ. Simulations of six radioisotopes of similar energy (<1.5 MeV) were generated to investigate how well LASSO and Elastic Net perform in masking and convolution problems in a shielded and unshielded situation.

Preliminary results for each method are promising. Overall, each method accurately selects the correct variables at a rate that should entice oil well logging companies to further investigate integrating these methods into their coding packages to reduce analysis times for their operators. LASSO performs better than Elastic Net in almost every trial conducted during this dissertation and is likely better suited for most radiation detection problems. Elastic Net performs best in applications where the data is highly correlated, and therefore should be considered for any application or situation where the data is correlated.

© Copyright 2019 by Vincent DiNova

All Rights Reserved

Automated Variable Selection of Gamma-Ray Spectra by Utilization of LASSO and Elastic Net
Techniques for Use in Nuclear Security Applications

by
Vincent A. DiNova, Jr.

A dissertation submitted to the Graduate Faculty of
North Carolina State University
in partial fulfillment of the
requirements for the degree of
Doctor of Philosophy

Nuclear Engineering

Raleigh, North Carolina
2019

APPROVED BY:

Dr. Robin Gardner
Committee Chair

Dr. Steven Shannon

Dr. Ge Yang

Dr. Ralph Smith

DEDICATION

This dissertation is dedicated to my mother, father, and sister for their constant support and encouragement. To my girlfriend, Stevie, and stepson, Speed, who inspire me to be a Rockstar in every aspect of my life.

BIOGRAPHY

Vincent DiNova was born in Orlando, Florida and traveled the world as the son of a naval officer. After completing high school at Apex High School, he went on to study Nuclear Engineering at NC State University. He completed his B.S. in Nuclear Engineering in 2009 and his M.S. in Nuclear Engineering under the direction of Dr. Robin P. Gardner in 2011. After working 3 years for Bechtel, Vincent returned to NC State University in 2014 to complete his PhD in Nuclear Engineering under the direction of Dr. Robin P. Gardner.

ACKNOWLEDGMENTS

There are so many people who have impacted me on this journey, I hope to capture them all, and I sincerely apologize if I forget any single person. If you read this and think you should have been listed here, believe me that although you are not listed, your impact has been noticed.

The people who have had the largest impact on my life and subsequent work is my family. To my mother and father, Vince and Kay, you have inspired me to be the best man I can be and to push myself to continue to improve every day. To my sister, Kristina, my brother-in-law, Tommy, and my nephew, Jack, my aunts and uncles, Karen, Joe, Nico and Lisa, my memaw and pepaw, and to all my cousins, you have all given me inspiration, examples to follow, and much help when needed. I thank and love you all.

To all my childhood friends who helped shape who I am. I want to especially acknowledge my wonderful friends from Apex High School and their families: Sean Roberts, Matt Baldiga, Kyle Beaulieu, Charlotte Florez, Jill Guyton, Nancy Andrews, Darah Willey, Vicki Tucci, Hanna Zombek, Claire Wagner, Meredith Caley, Christine Reed, and Jenna Ready. All of you helped bring me out of my shell. You and your families became family to me, I think of you all often, and I want you to know I would not have made it here without meeting each of you.

So many people helped me out during my undergraduate degree. To all my professors: Dr. Bourham, Dr. Hawari, Dr. Hankins, Dr. Anistratov, Dr. Doster, and Dr. Turinsky, you all gave me the skills I needed to carry forward to this point. To my classmates, thank you for making life more enjoyable during that period, especially, Aimee Smith, Alison Koeppel, Richard Mongold, and Chris Courtenay.

To all of the NC State bowling team for giving me the best times of my life. I especially want to thank Zack Brown, Jon Scorano, Nick Davis, Brian James, Wes Wheless, Eric Moore, Mike Flitcraft, Rachel Judd, AJ Van Fleet, Kyle Burns, and Craig Nursey. To our coach Irwyn Atkinson, who spent over 30 years coaching the NC State bowling team, you deserve to be immortalized in this work for the contribution you have made to the university and on my life. I thank you for your friendship and mentorship.

To my other bowling team and coworkers, Jimmy Martin, TJ Pocalyko, Bryan Callier, Chris Alexander, Kristin Brown, Dan Moore, Hal Odom, Marge Way, Ben Rose, Teddy, and

Julie Thomas, you are all amazing people, who I try to emulate the best I can. You have been tremendous friends for so long, and I thank you for all of your help over the years.

To all my peers during graduate school, you have all made these years fun and exciting. I especially want to thank Wes Holmes, Aaron Feinberg, Richard Howard, Adan Calderon, Sean O'brien, Brandon Burns, Andrew Petrarca, Josh Novak, Kyoung Lee, and Rob Weldon.

To my coworkers during my time at Bechtel, for providing me with professional and personal growth, I thank you. I especially want to thank Sarah Fafard, Fotios Raftelis, Hagan Baturay, Dave Dinse, Evan Fredo, Sam Watson, Grant Whitfield, Thomas Ramis, Dan Triplett, and Kenny Hearn.

There are a few people who helped keep me focused during my return to graduate school, Ashley Stancil and her family, Dara O'Sullivan, Rachel Helscher, and Kim Nguyen-Dinh. I thank you for all keeping me on a path that has led me here.

To my new family, Speed and Stevie, you give me the motivation to be the best I can be. This is as much for you, as any other person. I love you both.

Finally, to my committee, Dr. Shannon, Dr. Yang, and Dr. Smith, you have all been amazing mentors over the years. The impact you have had on my professional and personal growth cannot be measured. Lastly, I want to thank Dr. Gardner for calling me out of the blue in 2014 to get me to return to complete my studies. You have been a tremendous influence on my life for over 12 years and have touched so many lives over the 55+ years at NC State.

There will be more people who will come into my life and have an impact after this moment. This section is for you, I thank you in advance, and look forward to what is to come!

TABLE OF CONTENTS

LIST OF TABLES	viii
LIST OF FIGURES	x
Chapter 1: Introduction	1
1.1 Background	1
1.2 Benchmarking Tool and Facility	3
1.3 Monte Carlo Library Least Squares	5
1.4 Radioisotope Identification Devices	6
Chapter 2: Nuclear Reactions.....	8
2.1 Neutron Transport.....	8
2.1.1 Neutron Inelastic Scatter ($n, n'\gamma$)	8
2.1.2 Neutron Capture (n, γ)	9
2.2 Photon Transport.....	10
2.3 Detector Response	13
2.3.1 Spectral Features.....	13
Chapter 3: Machine Learning Enhancements	18
3.1 Supervised Machine Learning	18
3.1.1 Linear Least Squares.....	18
3.1.2 Least Absolute Selection and Shrinkage Operator (LASSO).....	19
3.1.3 Elastic Net.....	20
3.1.4 Coordinate Descent Solutions for LASSO and Elastic Net.....	21
3.1.4.1 LASSO Single Variable Case	22
3.1.4.2 Coordinate Descent for LASSO.....	23
3.1.4.3 Coordinate Descent for Elastic Net.....	25
3.1.5 Cross Validation.....	27
Chapter 4: Kansas State Experiment.....	29
4.1 Data Collection	29
4.1.1 Kansas State Experimental Data.....	29
4.1.2 Simulated Data.....	30
4.1.3 Simulated Example	30
4.2 Methods and Improvements.....	34
4.2.1 Full Procedure.....	34
4.2.2 Early Lessons Learned.....	35
4.3 Kansas State Experimental Results.....	38
4.3.1 Water Trial	39
4.3.2 Sand Trial.....	50
4.3.3 Sand with Water Trial.....	61
4.3.4 Limestone Trial.....	72
4.3.5 Limestone with Water Trial	83
4.4 Discussion.....	94

Chapter 5: Radioisotope Identification Device Algorithm.....	95
5.1 Data Collection	95
5.2 Masking Without Shielding	96
5.3 Convolution Without Shielding	101
5.4 Masking with Shielding	105
5.5 Convolution with Shielding	109
Chapter 6: Discussion and Conclusions	114
References.....	116
Appendix A: MCNP Sample Deck – KSU Application	119
Appendix B: LASSO Code Sample	124
Appendix C: Elastic Net Code Sample.....	127

LIST OF TABLES

Table 1-1	NAS findings.....	1
Table 2-1	Non-elastic scattering reactions and threshold energies.....	9
Table 3-1	Full LASSO Coordinate Descent Algorithm.....	25
Table 3-2	Full Elastic Net Coordinate Descent Algorithm.....	27
Table 4-1	Relative error of the two methods	34
Table 4-2	Optimal normalization parameters for water trial	47
Table 4-3	Linear coefficients and error for water near detector	49
Table 4-4	Linear coefficients and error for water far detector	50
Table 4-5	Optimal normalization parameters for sand trial.....	59
Table 4-6	Linear coefficients and error for sand near detector.....	61
Table 4-7	Linear coefficients and error for sand far detector	61
Table 4-8	Optimal normalization parameters for sand and water trial	70
Table 4-9	Linear coefficients and error for sand and water near detector	72
Table 4-10	Linear coefficients and error for sand and water far detector	72
Table 4-11	Optimal normalization parameters for limestone trial	81
Table 4-12	Linear coefficients and error for limestone near detector	83
Table 4-13	Linear coefficients and error for limestone far detector.....	83
Table 4-14	Optimal normalization parameters for limestone and water trial	92
Table 4-15	Linear coefficients and error for limestone and water near detector.....	94
Table 4-16	Linear coefficients and error for limestone and water far detector	94
Table 5-1	Masking coefficients and total count.....	97
Table 5-2	Masking trial prediction accuracy for LASSO and Elastic Net with varying count rates	100

Table 5-3 Convolution coefficients and total counts	101
Table 5-4 Convolution trial prediction accuracy for LASSO and Elastic Net with varying count rates	105
Table 5-5 Masking with shielding coefficients and total counts	106
Table 5-6 Masking with shielding trial prediction accuracy for LASSO and Elastic Net with varying count rates	109
Table 5-7 Convolution with shielding coefficients and total counts	110
Table 5-8 Convolution with shielding trial prediction accuracy for LASSO and Elastic Net with varying count rates.....	113

LIST OF FIGURES

Figure 1-1 Prompt and delayed gamma ray emission process	2
Figure 1-2 KSU benchmarking tool.....	3
Figure 1-3 Data acquisition scheme.....	3
Figure 1-4 KSU design facility	4
Figure 1-5 Test chamber	4
Figure 1-6 a. Open borehole tube, b. Capped borehole tube.....	5
Figure 2-1 Depiction of the Photoelectric Effect	10
Figure 2-2 Depiction of the Compton Scattering process	11
Figure 2-3 Illustration of the Compton edge and continuum.....	11
Figure 2-4 Depiction of interaction of gamma-rays with a detector medium and their resultant spectra.....	12
Figure 2-5 Energy dependence of photon interactions in NaI	13
Figure 2-6 Infinite resolution detector response	14
Figure 3-1 Soft-thresholding function.....	22
Figure 3-2 Holdout method for test-train split	28
Figure 3-3 Cross validation holdout.....	28
Figure 4-1 F8 tally simulated response and Gaussian broadened detector response	30
Figure 4-2 Cross validation normalization parameter selection for LASSO	31
Figure 4-3 LASSO model selection coefficients by changing normalization parameter.....	31
Figure 4-4 LASSO salt water simulation fit	32
Figure 4-5 Cross validation normalization parameter selection for Elastic Net	32
Figure 4-6 Elastic Net model selection by changing normalization parameter	33
Figure 4-7 Elastic Net salt water simulation fit	33

Figure 4-8 Full procedure.....	35
Figure 4-9 Pure water first fit.....	36
Figure 4-10 Pure water fit with NaI activation libraries added.....	36
Figure 4-11 Firing sequence and measured response	37
Figure 4-12 Time dependent format distributed by Kansas State University	38
Figure 4-13 Cross validation normalization parameter selection for the LASSO near detector water trial	39
Figure 4-14 LASSO model selection coefficients by changing the normalization parameter for the near detector water trial	40
Figure 4-15 LASSO fit for the near detector water trial	40
Figure 4-16 LASSO full fit for the near detector water trial.....	41
Figure 4-17 Cross validation normalization parameter selection for the Elastic Net near detector water trial	41
Figure 4-18 Elastic Net model selection coefficients by changing the normalization parameter for the near detector water trial	42
Figure 4-19 Elastic Net fit for the near detector water trial	42
Figure 4-20 Elastic Net full fit for the near detector water trial	43
Figure 4-21 Cross validation normalization parameter selection for the LASSO far detector water trial.....	43
Figure 4-22 LASSO model selection coefficients by changing the normalization parameter for the far detector water trial.....	44
Figure 4-23 LASSO fit for the far detector water trial	44
Figure 4-24 LASSO full fit for the far detector water trial.....	45
Figure 4-25 Cross validation normalization parameter selection for the Elastic Net far detector water trial.....	45
Figure 4-26 Elastic Net model selection coefficients by changing the normalization parameter for the far detector water trial.....	46

Figure 4-27 Elastic Net fit for the far detector water trial	46
Figure 4-28 Elastic Net full fit for the far detector water trial	47
Figure 4-29 Linear least squares fit and residual for the near detector water trial	48
Figure 4-30 Linear least squares fit and residual for the far detector water trial.....	48
Figure 4-31 Linear least squares fit for near and far detector water trials	49
Figure 4-32 Cross validation normalization parameter selection for the LASSO near detector sand trial.....	51
Figure 4-33 LASSO model selection coefficients by changing the normalization parameter for the near detector sand trial	51
Figure 4-34 LASSO fit for the near detector sand trial.....	52
Figure 4-35 LASSO full fit for the near detector sand trial	52
Figure 4-36 Cross validation normalization parameter selection for the Elastic Net near detector sand trial.....	53
Figure 4-37 Elastic Net model selection coefficients by changing the normalization parameter for the near detector sand trial	53
Figure 4-38 Elastic Net fit for the near detector sand trial	54
Figure 4-39 Elastic Net full fit for the near detector sand trial	54
Figure 4-40 Cross validation normalization parameter selection for the LASSO far detector sand trial	55
Figure 4-41 LASSO model selection coefficients by changing the normalization parameter for the far detector sand trial	55
Figure 4-42 LASSO fit for the far detector sand trial.....	56
Figure 4-43 LASSO full fit for the far detector sand trial	56
Figure 4-44 Cross validation normalization parameter selection for the Elastic Net far detector sand trial	57
Figure 4-45 Elastic Net model selection coefficients by changing the normalization parameter for the far detector sand trial	57

Figure 4-46 Elastic Net fit for the far detector sand trial	58
Figure 4-47 Elastic Net full fit for the far detector sand trial	58
Figure 4-48 Linear least squares fit and residual for the near detector sand trial.....	59
Figure 4-49 Linear least squares fit and residual for the far detector sand trial	60
Figure 4-50 Linear least squares fit for near and far detector sand trials.....	60
Figure 4-51 Cross validation normalization parameter selection for the LASSO near detector sand and water trial	62
Figure 4-52 LASSO model selection coefficients by changing the normalization parameter for the near detector sand and water trial	62
Figure 4-53 LASSO fit for the near detector sand and water trial.....	63
Figure 4-54 LASSO full fit for the near detector sand and water trial	63
Figure 4-55 Cross validation normalization parameter selection for the Elastic Net near detector sand and water trial	64
Figure 4-56 Elastic Net model selection coefficients by changing the normalization parameter for the near detector sand and water trial	64
Figure 4-57 Elastic Net fit for the near detector sand and water trial.....	65
Figure 4-58 Elastic Net full fit for the near detector sand and water trial	65
Figure 4-59 Cross validation normalization parameter selection for the LASSO far detector sand and water trial.....	66
Figure 4-60 LASSO model selection coefficients by changing the normalization parameter for the far detector sand and water trial.....	66
Figure 4-61 LASSO fit for the far detector sand and water trial	67
Figure 4-62 LASSO full fit for the far detector sand and water trial.....	67
Figure 4-63 Cross validation normalization parameter selection for the Elastic Net far detector sand and water trial.....	68
Figure 4-64 Elastic Net model selection coefficients by changing the normalization parameter for the far detector sand and water trial.....	68

Figure 4-65 Elastic Net fit for the far detector sand and water trial	69
Figure 4-66 Elastic Net full fit for the far detector sand and water trial.....	69
Figure 4-67 Linear least squares fit and residual for the near detector sand and water trial	70
Figure 4-68 Linear least squares fit and residual for the far detector sand and water trial.....	71
Figure 4-69 Linear least squares fit for near and far detector sand and water trials	72
Figure 4-70 Cross validation normalization parameter selection for the LASSO near detector limestone trial.....	73
Figure 4-71 LASSO model selection coefficients by changing the normalization parameter for the near detector limestone trial.....	73
Figure 4-72 LASSO fit for the near detector limestone trial	74
Figure 4-73 LASSO full fit for the near detector limestone trial.....	74
Figure 4-74 Cross validation normalization parameter selection for the Elastic Net near detector limestone trial.....	75
Figure 4-75 Elastic Net model selection coefficients by changing the normalization parameter for the near detector limestone trial.....	75
Figure 4-76 Elastic Net fit for the near detector limestone trial	76
Figure 4-77 Elastic Net full fit for the near detector limestone trial.....	76
Figure 4-78 Cross validation normalization parameter selection for the LASSO far detector limestone trial	77
Figure 4-79 LASSO model selection coefficients by changing the normalization parameter for the far detector limestone trial	77
Figure 4-80 LASSO fit for the far detector limestone trial.....	78
Figure 4-81 LASSO full fit for the far detector limestone trial	78
Figure 4-82 Cross validation normalization parameter selection for the Elastic Net far detector limestone trial	79
Figure 4-83 Elastic Net model selection coefficients by changing the normalization parameter for the far detector limestone trial	79

Figure 4-84 Elastic Net fit for the far detector limestone trial.....	80
Figure 4-85 Elastic Net full fit for the far detector limestone trial	80
Figure 4-86 Linear least squares fit and residual for the near detector limestone trial.....	81
Figure 4-87 Linear least squares fit and residual for the far detector limestone trial	82
Figure 4-88 Linear least squares fit for near and far detector limestone trials.....	82
Figure 4-89 Cross validation normalization parameter selection for the LASSO near detector limestone and water trial	84
Figure 4-90 LASSO model selection coefficients by changing the normalization parameter for the near detector limestone and water trial	84
Figure 4-91 LASSO fit for the near detector limestone and water trial.....	85
Figure 4-92 LASSO full fit for the near detector limestone and water trial	85
Figure 4-93 Cross validation normalization parameter selection for the Elastic Net near detector limestone and water trial.....	86
Figure 4-94 Elastic Net model selection coefficients by changing the normalization parameter for the near detector limestone and water trial	86
Figure 4-95 Elastic Net fit for the near detector limestone and water trial.....	87
Figure 4-96 Elastic Net full fit for the near detector limestone and water trial	87
Figure 4-97 Cross validation normalization parameter selection for the LASSO far detector limestone and water trial	88
Figure 4-98 LASSO model selection coefficients by changing the normalization parameter for the far detector limestone and water trial	88
Figure 4-99 LASSO fit for the far detector limestone and water trial	89
Figure 4-100 LASSO full fit for the far detector limestone and water trial	89
Figure 4-101 Cross validation normalization parameter selection for the Elastic Net far detector limestone and water trial	90
Figure 4-102 Elastic Net model selection coefficients by changing the normalization parameter for the far detector limestone and water trial	90

Figure 4-103 Elastic Net fit for the far detector limestone and water trial	91
Figure 4-104 Elastic Net full fit for the far detector limestone and water trial	91
Figure 4-105 Linear least squares fit and residual for the near detector limestone and water trial.....	92
Figure 4-106 Linear least squares fit and residual for the far detector limestone and water trial	93
Figure 4-107 Linear least squares fit for near and far detector limestone and water trials.....	93
Figure 5-1 Vised depiction of detector geometry	96
Figure 5-2 MCNP generated radioisotope libraries	96
Figure 5-3 LASSO masking low count rate fit	97
Figure 5-4 Elastic Net masking low count rate fit	98
Figure 5-5 LASSO masking medium count rate fit	98
Figure 5-6 Elastic Net masking medium count rate fit	99
Figure 5-7 LASSO masking high count rate fit	99
Figure 5-8 Elastic Net masking high count rate fit	100
Figure 5-9 LASSO convolution low count rate fit.....	102
Figure 5-10 Elastic Net convolution low count rate fit.....	102
Figure 5-11 LASSO convolution medium count rate fit.....	103
Figure 5-12 Elastic Net convolution medium count rate fit.....	103
Figure 5-13 LASSO convolution high count rate fit.....	104
Figure 5-14 Elastic Net convolution high count rate fit.....	104
Figure 5-15 LASSO masking with shielding low count rate fit.....	106
Figure 5-16 Elastic Net masking with shielding low count rate fit.....	107
Figure 5-17 LASSO masking medium count rate fit	107

Figure 5-18 Elastic Net masking with shielding medium count rate fit	108
Figure 5-19 LASSO masking with shielding high count rate fit	108
Figure 5-20 Elastic Net masking with shielding high count rate fit	109
Figure 5-21 LASSO convolution with shielding low count rate fit.....	110
Figure 5-22 Elastic Net convolution with shielding low count rate fit	111
Figure 5-23 LASSO convolution with shielding medium count rate fit.....	111
Figure 5-24 Elastic Net convolution with shielding medium count rate fit	112
Figure 5-25 LASSO convolution with shielding high count rate fit.....	112
Figure 5-26 Elastic Net convolution with shielding high count rate fit.....	113

CHAPTER 1

Introduction

1.1 Background

Shortly after the tragedies of September 11, 2001, the National Academies of Science commissioned a study on the dangers of long-lived radioisotope sources. The study concluded that there exist several commonly used sources that could potentially be used as a dirty bomb or terror weapon (Table 1-1). The Consortium for Nonproliferation Enabling Capabilities (CNEC) was funded in 2014 to research innovative ways to address nuclear security problems including finding suitable replacements for dangerous radiological sources.

Table 1-1: NAS findings

Radionuclide	Half-life (yr)	Particles-Energies (MeV)	Principal Applications	US Inventory (Ci)
Cs-137	30.17	β -0.518 max; β -1.18 max; γ -0.662	Industrial gauging, Irradiators, Well logging	2,800,000
Co-60	5.27	γ -1.173; γ -1.333	Sterilization, Irradiators, Teletherapy	198,000,000
Am-241	432.2	α -5.64; γ -0.060	Well logging, Gauging	6,482
Pu-238	87.7	α -5.59; γ -0.043	RTGs	937
Sr-90	28.9	β -0.546 max	RTGs	1,730,000
Se-75	119.8 d	γ -0.28 (ave), 0.8 max	Radiography	261
Ir-192	74 d	β -1.46 max] γ -0.38 ave, 1.378 max	Radiography	146,922
Cf-252	2.645	α -6.22; n -2 ave; γ -various; fission products	Well logging Research	7

Devices used in the oil well logging industry were identified as a major point of interest as they utilize high activity Cs-137 and AmBe sources for density, porosity, and elemental composition measurements. A testing facility and benchmarking tool were designed and built at Kansas State University to test the viability of replacing traditional active sources with a D-T Pulsed Neutron Generator (PNG). A PNG operates by receiving a signal to initialize a pulse

firing sequence that propels Deuterons and Tritons on a collision path releasing 14.1 MeV neutrons. These high-energy neutrons are used as an alternative to AmBe neutrons in a traditional prompt gamma neutron activation analysis (PGNAA) application. PGNAA is a nondestructive method that relies on (n, γ) neutron capture, and $(n, n'\gamma)$ neutron inelastic scattering reactions to produce gamma photons, each having distinct characteristics of the target nuclei. Using a near and far NaI scintillator detector, each spectral detector response can be analyzed for elemental composition.

PGNAA suffers from a low signal to noise ratio caused by the delayed activation of nuclei or neutron activation analysis (NAA). Neutron activation analysis utilizes the delayed gamma rays from radioactive daughters, while PGNAA exploits the prompt gamma rays (Fig. 1-1). The neutron cross sections for both prompt and delayed reactions compete and create a mixed signal that is often difficult to process. Additional sources of interference include:

- 1) γ rays produced by the PNG
- 2) γ rays from activation inside the detector medium (Gardner, 2000)
- 3) γ rays from background sources
- 4) γ rays produced by the activation of construction materials in the benchmarking tool.

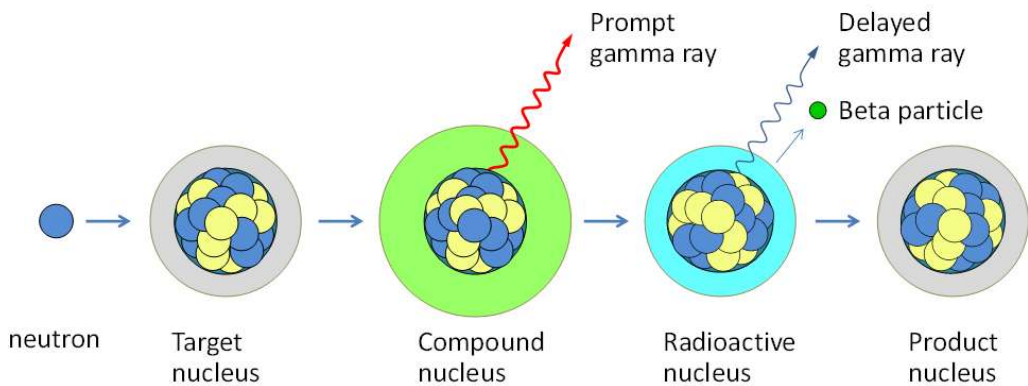


Figure 1-1: Prompt and delayed gamma ray emission process

The PNG offers a unique solution to this problem by exploiting the pulsing time responses with a digitizer allowing the prompt and delayed responses to be extracted and separated. This critical step allows for supervised machine learning variable selection techniques such as LASSO and Elastic Net to be applied to the prompt and delayed responses, offering an on-line analysis in a changing environment with improved capabilities over traditional linear least squares methods.

1.2 Benchmarking tool and facility

The benchmarking tool and design facility were designed and constructed at Kansas State University. The tool consists of near and far gamma and neutron detectors separated from a D-T PNG source by a 2" lead divider (Fig. 1-2). A CAEN 5730 digitizer acts to both send the pulse firing sequence to the PNG and to collect the responses from the gamma and neutron detectors (Fig. 1-3).

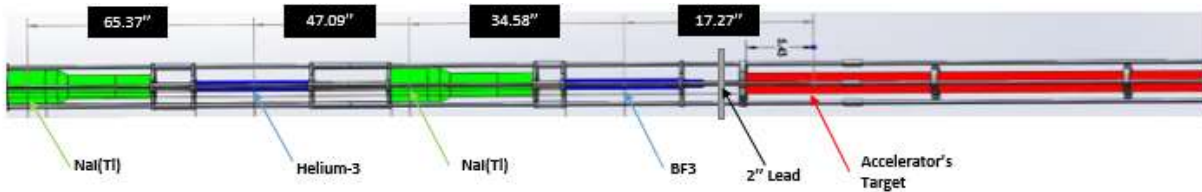


Figure 1-2: KSU benchmarking tool

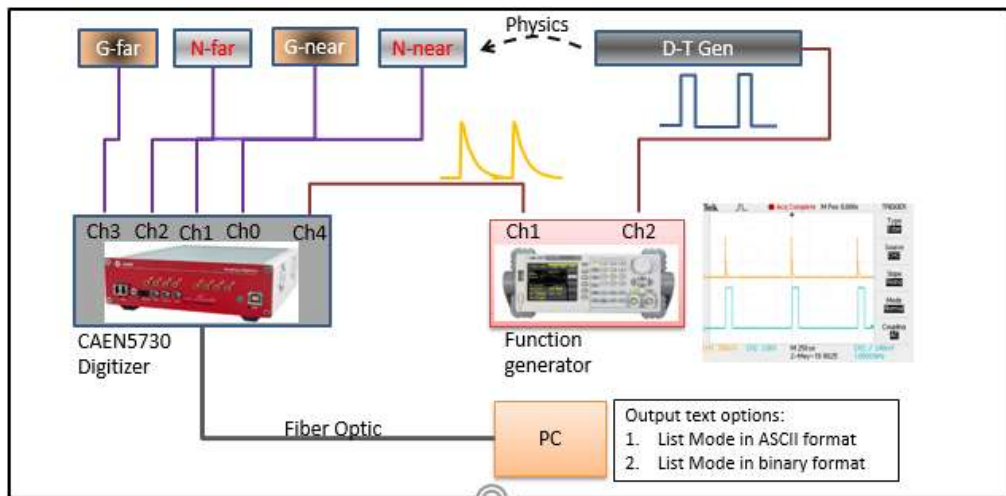


Figure 1-3: Data acquisition scheme

The design facility (Fig. 1-4) is located at King Hall Annex at Kansas State University. Special accelerator enabling systems were required to gain approval from the Kansas Safety Board to prevent inadvertent neutron production and entries into the facility. These safeguards include audio and video surveillance, controlled access points, intercommunication systems, warning lights, and detailed operating procedures to minimize unnecessary dosage to bystanders.

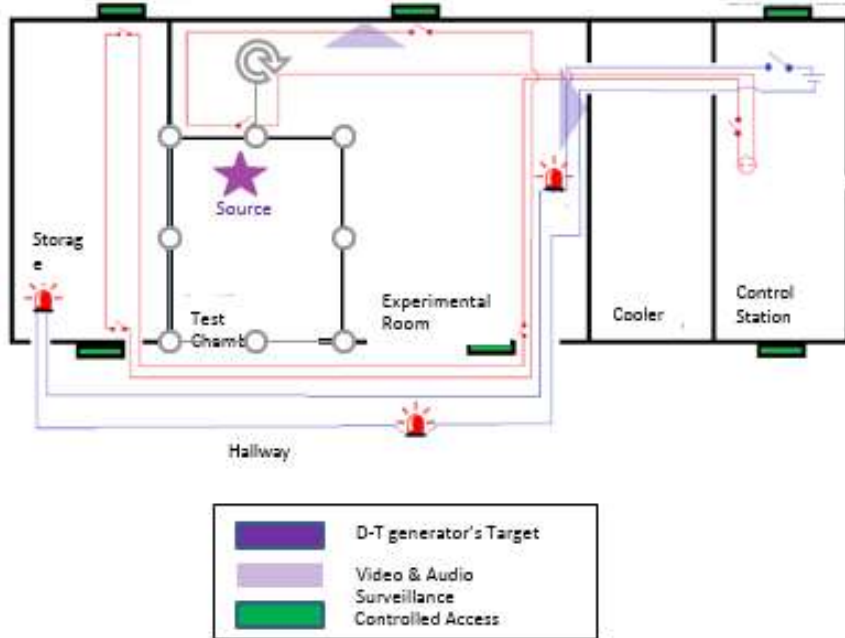


Figure 1-4: KSU design facility

The test chamber (Figs. 1-5, 1-6) is 6'8" high by 6'6" wide and 8' deep with a total volume of roughly 2,500 gallons. These dimensions ensure that when fully filled with water, the test chamber presents an effectively infinite medium to the 14.1 MeV neutrons. During the data collection process, the benchmarking tool is loaded into the borehole tube and enclosed by a cap. Borated polyethylene (green material) has been fitted both inside and outside the test chamber to reduce neutron escape and dosage.

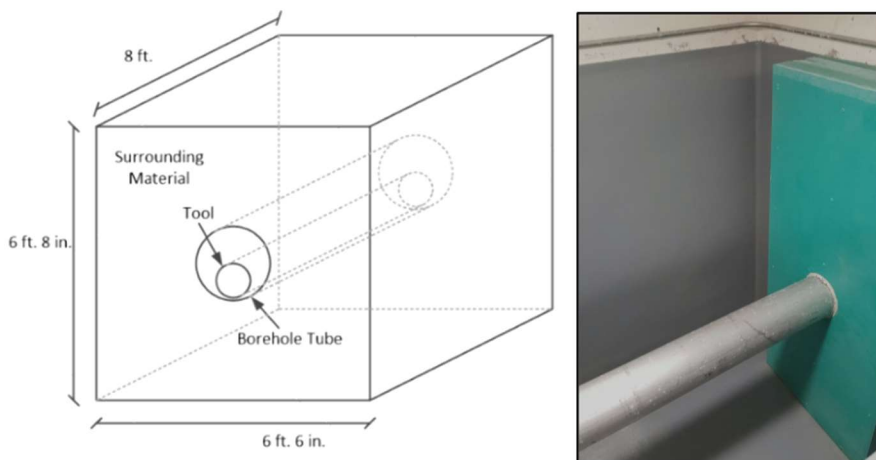


Figure 1-5: Test chamber

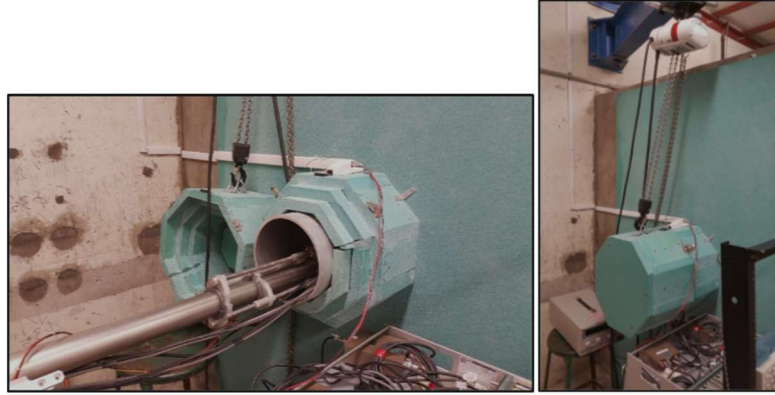


Figure 1-6: a. Open borehole tube

b. Capped borehole tube

1.3 Monte Carlo Library Least Squares

In order to quantitatively analyze measured PGNAA γ spectra, Monte Carlo Library Least Squares (MCLLS) has been shown to be an effective method over single peak analysis (Gardner, 1997). MCLLS requires extremely accurate forward model simulations to represent the expected pulse-height spectrum obtained with a PGNAA system with a known geometry and compositional makeup. Previous studies have demonstrated the effectiveness on bulk coal (Shyu et al., 1988, 1998) and PGNAA applications (Han, 2005 and Hou, 2017). The MCLLS approach consists of:

- 1) Generating pulse-height spectra with MCNP or similar coding packages using assumed or known geometry and compositions.
- 2) Utilizing each prompt γ -ray pulse-height spectrum as a library input variable for model selection.
- 3) Adjusting all non-linear parameters between simulated and experimental response to treat the problem as a sum of linear responses.
- 4) Perform a linear library least-squares (LLS) analysis.

Assuming all non-linear physical components are correctly adjusted, the library least-squares method treats an unknown sample as the sum of the products of an elemental amount with the library spectrum of each element for each channel as given by equation 1.1.

$$y_i = \sum_{j=1}^m a_j x_{ij} + e_j \quad i = 1, 2, 3, \dots, n \quad (1.1)$$

Where,

- y_i is the counts per channel i of an unknown spectrum
- a_j are linear coefficients for each element j
- x_{ij} are the library spectra, or counts in channel i of element j
- e_i is random error in counts in channel i

Equation 1.1 is solved for x_j by minimizing the reduced Chi-Square χ^2_v given by equation 1.2.

$$\chi^2_v = \sum_{i=1}^n \frac{e_i^2}{(n - m)\sigma_i^2} \quad (1.2)$$

Where,

- $(n - m)$ is the number of degrees of freedom
- e_i is random error in counts in channel i
- σ_i^2 is the variance of the random error in counts in each channel i

1.4 Radioisotope Identification Devices

During this investigation using LASSO and Elastic Net variable selection techniques on oil well logging devices, radioisotope identification devices (RIIDs) were targeted as another application that could be improved by the use of these algorithms. RIIDs are handheld instruments designed to identify radioactive materials by their emitted gamma ray energies. RIID algorithm development is necessary to ensure that potential threats are correctly identified by field agents and first responders. A study from 2003 concluded that only 30%-50% of medical, industrial, NORM, and threat isotopes were correctly identified (Blackadar et. al).

RIID algorithms measure similarities between measured characteristics of test spectrum and reference spectra, whether experimental or simulated. Many challenges emerge as a result of variations that occur naturally (Burr and Hamada, 2009) including:

- Absorbers can attenuate counts differentially with respect to energy, causing distorted pulse height distributions.

- Voltage calibrations can be nonlinear, and electronic gain shift effects can be nonlinear and unstable over time due to environmental effects.
- Procedural protocols can complicate the required measurements. Temperature and spatial factors can impact the calibration and collection time necessary to collect accurate measurements.
- There can be hundreds of isotopes in the isotope library, each with numerous example spectra.
- Detector dead time and pulse pile up can distort the test spectra.

Due to inadequate RIID algorithm performance, the U.S. Department of Energy (DOE) requires trained spectroscopists to be on call to resolve alarms as rapidly as possible. It was identified that human experts outperform even the best RIID algorithms, leading to the study of supervised machine learning techniques established by experts to help address these shortcomings.

CHAPTER 2

Nuclear Reactions

Prompt gamma-ray neutron activation analysis (PGNAA) is a nondestructive, near real time technique used for bulk material identifications. PGNAA relies on neutron inelastic scatter and capture reactions to produce characteristic γ -rays used to identify minute amounts of elements in a bulk sample. Due to low cross sections for these reactions, background sources from natural radiation, activation of the NaI detector, and γ -rays from the decay of the neutron source a low signal to noise ratio (SNR) is common.

2.1 Neutron Transport

There are a number of different mechanisms by which neutrons can interact with nuclei. For the prompt gamma neutron activation analysis application, only two are considered.

2.1.1 Neutron Inelastic Scatter ($n, n'\gamma$)

Neutron inelastic scatter involves an incoming neutron colliding with a target nucleus and exiting with less energy and at a different angle than it entered. The energy deposited on the target nucleus causes it to reach an excited state and rapidly releases a γ -ray to return to its normal energy state represented in equation 2.1 as follows:



The inelastic scattering reaction requires an incoming neutron to have enough energy to break the threshold energy derived from the Q value formula shown in equation 2.2.

$$T_n \geq E_{L1} \frac{A+1}{A} \quad (2.2)$$

Where,

- T_n is the kinetic energy of the incident neutron
- E_{L1} is the energy of the target nucleus' first excited level
- A is the atomic number of the target nucleus

The PNG is advantageous for this decay scheme, as the 14.1 MeV neutrons allow a greater number of isotopes to undergo inelastic scattering and unlock higher energy states. Table 2-1 (Kim et al. 2006) below lists some common inelastic scatter threshold energies and cross sections.

Table 2-1: Non-elastic scattering reactions and threshold energies

Reaction	Gamma Ray Energy, keV	Threshold, MeV	Peak Cross Section, mb	Energy of Peak, MeV
$^{12}\text{C}(\text{n},\text{n}\gamma)^{12}\text{C}$	4438.0	4.8	450.	8.1
$^{16}\text{O}(\text{n},\text{n}\gamma)^{16}\text{O}$	6128.6	6.6	265.	7.5–9.0
$^{16}\text{O}(\text{n},\text{p})^{16}\text{N}$	6128.6	10.6	50.	11.5
$^{16}\text{O}(\text{n},\text{np}\gamma)^{15}\text{N}$	5269.2	16.5	40.	27.5
$^{16}\text{O}(\text{n},\text{n}\alpha\gamma)^{12}\text{C}$	4438.0	12.3	130.	19.
$^{24}\text{Mg}(\text{n},\text{n}\gamma)^{24}\text{Mg}$	1368.6	1.4	600.	2.5–6.0
$^{27}\text{Al}(\text{n},\text{n}\gamma)^{27}\text{Al}$	1014.4	1.1	220.	2.5–6.7
$^{27}\text{Al}(\text{n},\text{n}\gamma)^{27}\text{Al}$	2211.	2.25	210.	7.0–9.5
$^{28}\text{Si}(\text{n},\text{n}\gamma)^{28}\text{Si}$	1779.0	1.8	770.	4.5–6.0
$^{32}\text{S}(\text{n},\text{n}\gamma)^{32}\text{S}$	2230.1	2.3	440.	6.7–10.0
$^{40}\text{Ar}(\text{n},\text{n}\gamma)^{40}\text{Ar}$	1460.8	1.5	800.	3.–10.
$^{40}\text{Ar}(\text{n},\text{p})^{40}\text{Cl}$	1460.8	8.0	20.	14.5
$^{40}\text{Ca}(\text{n},\text{n}\gamma)^{40}\text{Ca}$	3736.5	3.8	130.	7.0
$^{56}\text{Fe}(\text{n},\text{n}\gamma)^{56}\text{Fe}$	846.8	0.9	1150.	6.
$^{56}\text{Fe}(\text{n},\text{n}\gamma)^{56}\text{Fe}$	1238.3	2.1	475.	16.5

2.1.2 Neutron Capture (n, γ)

Neutron capture, also denoted as (n, γ) , can occur over a wide range of energies and has the highest probability at thermal energies. The (n, γ) reaction begins when a neutron interacts with a target nucleus and is absorbed. The newly formed nucleus is placed in an excited state, and in order to form a new ground state, at least one γ photon is emitted as shown in eq. 2.3 below.



Each nucleus (apart from Helium-4) gives off a distinct signature of intensities and energies, allowing for the identification of the sample from the γ photon emissions.

2.2 Photon Transport

2.2.1 Photon Reactions

The benchmarking tool analysis relies on three main photon reactions: photoelectric absorption, Compton scattering, and pair production. Although there are other photon reactions, none are an important focus to this work.

Photoelectric Absorption

During photoelectric absorption, a photon interacts with a target atom's electron, departs all of its energy, disappears, and ejects the electron from its bound shell. The photoelectron carries an energy given by equation 2.4 and illustrated by figure 2-1.

$$E_{e^-} = h\nu - E_b \quad (2.4)$$

Where,

- E_b is the binding energy of the photoelectron in its original shell
- E_{e^-} is the energy of the exited photoelectron
- $h\nu$ is the energy of the incoming photon

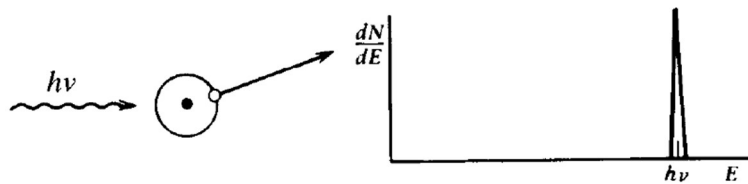


Figure 2-1: Depiction of the Photoelectric Effect

Compton Scattering

Compton scattering takes place when a photon interacts with an electron in an atom, it deflected while imparting some of its original energy, and ejects an electron from its orbit. Depending on the scattering angle, the energy transferred to the electron can range from zero to a large fraction of the total photon energy. The energy of the scattered photon and kinetic energy of the scattered electron can be calculated if the energy of the incident photon and incident angle are known by

$$E'_\gamma = \frac{E_\gamma}{1 + (1 - \cos\theta)E_\gamma/m_e c^2} \quad (2.5)$$

Where,

- E'_γ is the scattered photon energy
- E_γ is the energy of the incident photon
- $\cos\theta$ is the scattering angle in the lab frame
- m_e is the mass of the electron
- c is the speed of light



Figure 2-2: Depiction of the Compton Scattering process

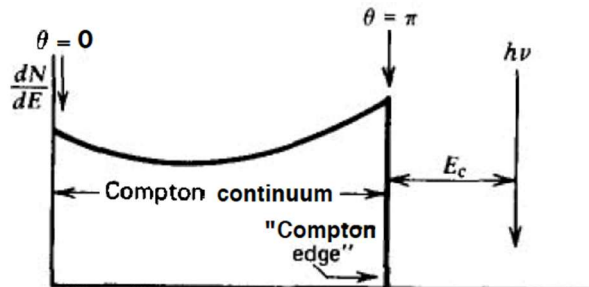


Figure 2-3: Illustration of the Compton edge and continuum

Pair Production

When an incoming photon exceeds 1.02 MeV, a photon can disappear and create an electron-positron pair. All additional energy carried by the photon above 1.02 MeV is converted into kinetic energy shared by the positron and electron. Although possible at any energy above 1.02 MeV, pair production does not become the dominant reaction until photon energies exceed 5 MeV as shown in Figure 2-5.

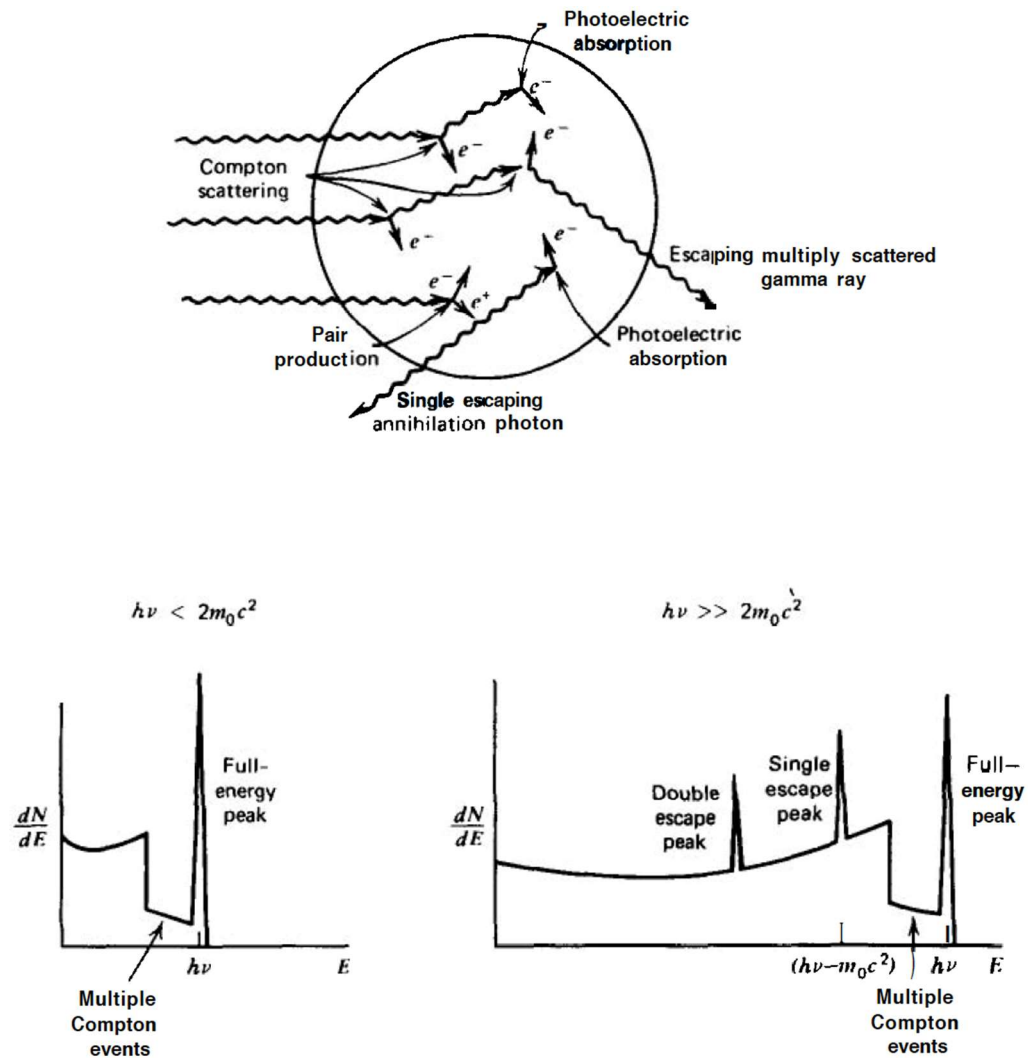


Figure 2-4: Depiction of interaction of gamma-rays with a detector medium and their resultant spectra

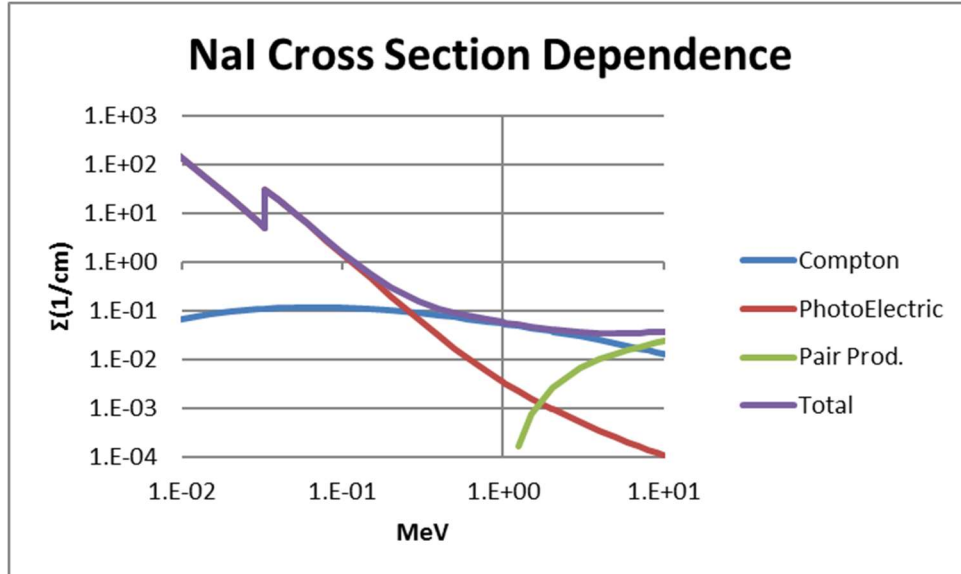


Figure 2-5: Energy dependence of photon interactions in NaI

2.3 Detector Response

Incident radiation interacting with the detector are modeled in MCNP 6.1 and carry distinct physical signatures (Knoll, 2011). The first order physics alone do not provide a genuine representation of the response from a detector. In order to accurately reproduce a detector response, a detector response function (DRF) must be applied. A detector response function is the expected detector response provided an incoming particle (Gardner and Sood, 2004). During this stage, all non-linear characteristics are removed, allowing the problem to be solved by linear methods.

2.3.1 Spectral Features

Figure 2-6 will serve as an example of the expected features produced by a monoenergetic photon on a detector. The response simulates a 0% resolution detector response from an incoming 6.13 MeV Oxygen-16 decay γ -ray.

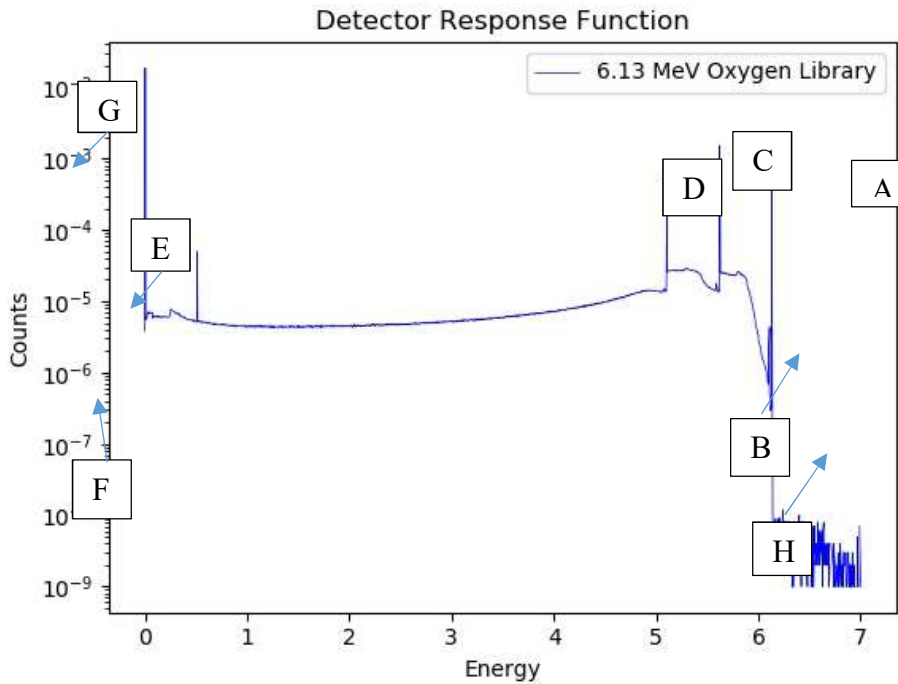


Figure 2-6: Infinite resolution detector response

A: Full Energy Peak

The full energy peak is equal to the incoming photon energy, 6.13 MeV for this example. The pulse signals that produce this signature occur when the particle enters the detector and deposits all its energy with no escaping secondary particles. This can occur in a singular photoelectric absorption or by a series of reactions. For this reason, the full energy peak can be referred to as the “photoelectric peak”.

B: Compton Edge

Not all events result in full energy deposition. The Compton edge occurs once a photon undergoes a Compton scattering reaction, and then exits the detector without depositing additional energy. The scattering angle determines the energy that is deposited in the detector, ranging from 0° to 180° . From equation 2.6, the maximum energy deposited by a Compton scattering identified as the Compton edge is

$$\Delta E = E_\gamma - E'_{\gamma} = 6.13 - \frac{6.13}{1 + (1 - \cos\pi) * \frac{6.13}{0.511}} = 5.88 \text{ MeV} \quad (2.6)$$

C: Single Escape Peak

In the event a photon creates a pair production reaction, an electron-positron pair is created. The positron will then annihilate inside the detector, creating a 0.511 MeV photon. If the annihilation photon exits the detector without depositing its energy and the full energy of the incoming photon is deposited inside the detector, the result is the single escape peak. The energy of the peak is equal to the full energy peak minus the resting mass energy of an electron, 0.511 MeV.

D: Double Escape Peak

The double escape peak is the result of both annihilation photons escaping the detector. As a result, the detected energy is equal to that of the full energy peak minus the resting mass energy of two electrons, 1.022 MeV.

E: Annihilation Peak

In the event that the incoming particle interacts with a material outside of the detector by a pair production reaction, a resulting annihilation photon can enter the detector and deposit its energy. The annihilation peak appears when the detector is surrounded by a dense material and is equal to 0.511 MeV.

F: Backscattering Peak

The backscattering peak is created when a Compton scattering event occurs outside the detector and the scattered photon reaches the detector and deposits its full energy. The scattering angle occurs over a small range of angles around 180°. This causes the peak to be a range of energies instead of a singular energy peak. The energy for backscattering peak is usually between 200 and 300 KeV. For the case of 180° scatter, the energy of the incoming scattered photon would be

$$E'_{\gamma} = \frac{6.13}{1 + (1 - \cos\pi) * \frac{6.13}{0.511}} = 0.245 \text{ MeV} \quad (2.7)$$

G: X-Ray Fluorescence Peaks

X-ray fluorescence peaks are not of interest to prompt gamma neutron activation analysis and contributes to a collection of noise signatures that collect below 100 KeV. These peaks are generated by interactions that occur in the surrounding medium by exciting the target atom. During the de-excitation, characteristic X-ray photons are emitted and enter the detector and deposit their full energy. These peaks complicate the fitting functions, as they can be orders of magnitude higher than other signatures within the spectrum.

H: X-Ray Escape Peaks

When the excited atoms discussed above are created within the detector, an X-ray photon can exit the detector. The resulting energy response is equal to the full energy peak minus the energy carried by the exited photon. If the detector material is larger than 1", these events happen infrequently and do not affect the total response substantially.

Energy Resolution

Unfortunately, Figure 2-6 does not accurately represent the true response of even the highest resolution detectors. The energy resolution is dependent on the characteristics of the detector material and electronics. For scintillation detectors, the energy peaks are Gaussian distributed and can be described by the normal distribution

$$f(E|\mu, \sigma^2) = \frac{1}{\sqrt{2\pi\sigma^2}} * \exp^{-\frac{(E-\mu)^2}{2\sigma^2}} \quad (2.8)$$

Where,

- E is the energy
- μ is the peak centroid
- σ is the standard deviation

The common way of determining the standard deviation is by measuring the full width at half maximum (FWHM), or the width of the peak at half of the amplitude. The standard deviation can be calculated by solving for

$$FWHM \approx 2.355\sigma \quad (2.9)$$

It has been demonstrated (Wang and Gardner, 2012) that a subroutine can fit parameters to simplify the FWHM equation to

$$FWHM = d * E^e \quad (2.10)$$

Where,

- E is the energy
- d, e are empirical fitting parameters

CHAPTER 3

Machine Learning

Enhancements

Many modern-day advancements have been made with the assistance of machine learning techniques. Traditional methods of solving linear least squares (LLS) problems can be enhanced by utilizing ready-made packages available on MATLAB and Python coding platforms. All codes used for this investigation have been modified from the sklearn packages in Python.

3.1 Supervised Machine Learning

3.1.1 Linear Least Squares

The linear model and analysis have been thoroughly used and examined over the last half century and remains important. The linear model, given a vector of inputs X_j , an output Y can be predicted as

$$\hat{Y} = \hat{\beta}_0 + \sum_{j=1}^p X_j \hat{\beta}_j \quad (3.1)$$

Where,

- $\hat{\beta}_0$ is the intercept, also known as the bias in machine learning
- \hat{Y} is the predicted output

$\hat{\beta}_0$ can be included in the vector coefficients and a constant variable 1 in X, allowing equation 3.1 to be rewritten as

$$\hat{Y} = X^T \hat{\beta} + \varepsilon \quad (3.2)$$

Where,

- X^T is the vector or matrix transpose
- \hat{Y} is the predicted output
- $\hat{\beta}$ is the linear coefficient
- ε is the error

Fitting a linear model to a training data set is popularly done by selecting the β coefficients that minimize the residual sum of squares

$$\begin{aligned} RSS(\beta) &= \sum_{i=1}^N (y_i - x_i^T \beta)^2 \\ &= \sum_{i=1}^N (y_i - \beta_0 - \sum_{j=1}^p x_{ij} \beta_j)^2 \end{aligned} \quad (3.3)$$

The ordinary least squares estimator can be computed by using the following equation

$$\hat{\beta}_{OLS} = (X^T X)^{-1} X^T Y \quad (3.4)$$

3.1.2 Least Absolute Selection and Shrinkage Operator (LASSO)

The least absolute selection and shrinkage operator (LASSO) method became popular as a statistical and modeling method to reduce or eliminate unnecessary variables from a model (Tibshirani, 1996). The LASSO method utilizes tuning parameters to shrink and select variables placed in a linear model by reducing predictive error between in and out of sample tests, also known as test/train splitting in machine learning. LASSO is defined as

$$\hat{\beta}^{lasso} = \underset{\beta \in \mathbb{R}^p}{argmin} ||y - X\beta||_2^2 + \lambda \sum_{j=1}^p |\beta_j| \quad (3.5)$$

Or

$$= \underset{\beta \in \mathbb{R}^p}{argmin} ||y - X\beta||_2^2 + \lambda ||\beta||_1$$

Where,

- $\|y - X\beta\|_2^2$ is the loss function
- $\lambda\|\beta\|_1$ is a tuning parameter that serves as a penalty
 - Note: when $\lambda = 0$, eq. 3.4 is identical to linear least squares (LLS)

3.1.3 Elastic Net

LASSO has been thoroughly investigated since its introduction. While offering many benefits over traditional linear least squares, limitations were found in situations where

- a) In a case where the number of observations (n) are less than the number of parameters (p) LASSO can select at most n variables
- b) In a case where there are a large number of predictors that are highly correlated, LASSO tends to select only 1, seemingly at random (grouping effect)
- c) In a case where $n > p$ and the predictors are highly correlated; LASSO is dominated by shrinkage methods like Ridge Regression

To remedy these deficiencies, Elastic Net was proposed (Zou and Hastie, 2005). The Elastic Net variable selection method combines the penalty terms used in LASSO and Ridge Regression as

$$\hat{\beta}^{ElasticNet} = \underset{\beta \in \mathbb{R}^p}{argmin} \|y - X\beta\|_2^2 + \lambda_2\|\beta\|_2^2 + \lambda_1\|\beta\|_1 \quad (3.6)$$

Where,

- $\|y - X\beta\|_2^2$ is the loss function
- $\lambda_1\|\beta\|_1$ is a tuning parameter that serves as a penalty from LASSO
- $\lambda_2\|\beta\|_2^2$ is a quadratic tuning parameter that serves as a penalty from Ridge Regression
 - Note: when $\lambda_2 = 0$, eq. 3.5 is identical to LASSO
 - Note: when $\lambda_1, \lambda_2 = 0$, eq. 3.5 is identical to linear least squares (LLS)

3.1.4 Coordinate Descent Solutions for LASSO and Elastic Net

Before diving into the detailed derivation for coordinate descent solutions to LASSO and Elastic Net, some background information and notations are necessary (Gauraha, 2018). Consider the standard linear regression equation given as equation 3.2, assume the components of the noise vector are independent and identically distributed. Using subscripts j to denote the j th column of a dataset. Assuming that the design matrix \mathbf{X} is fixed, the data is adjusted to be centered, and the predictors are standardized such that

$$\sum_{i=1}^n \mathbf{Y}_i = 0, \sum_{i=1}^n (\mathbf{X}_j)_i = 0 \text{ and } \frac{1}{n} \mathbf{X}_j^T \mathbf{X}_j = 1 \text{ for all } j = 1, \dots, p. \quad (3.7)$$

The $l_{0,1,2}$ -norms are defined as

$$\begin{aligned} ||\beta||_0 &= \sum_{j=1}^p \mathbf{I}(\beta_j \neq 0) \\ ||\beta||_1 &= \sum_{j=1}^p |\beta_j| \\ ||\beta||_2^2 &= \sum_{j=1}^p \beta_j^2 \end{aligned} \quad (3.8)$$

Then, the soft-thresholding operator can be defined as follows

$$S_\lambda(x) = \begin{cases} x + \lambda & \text{if } x < -\lambda \\ 0 & \text{if } |x| \leq \lambda \\ x - \lambda & \text{if } x > \lambda \end{cases} \quad (3.9)$$

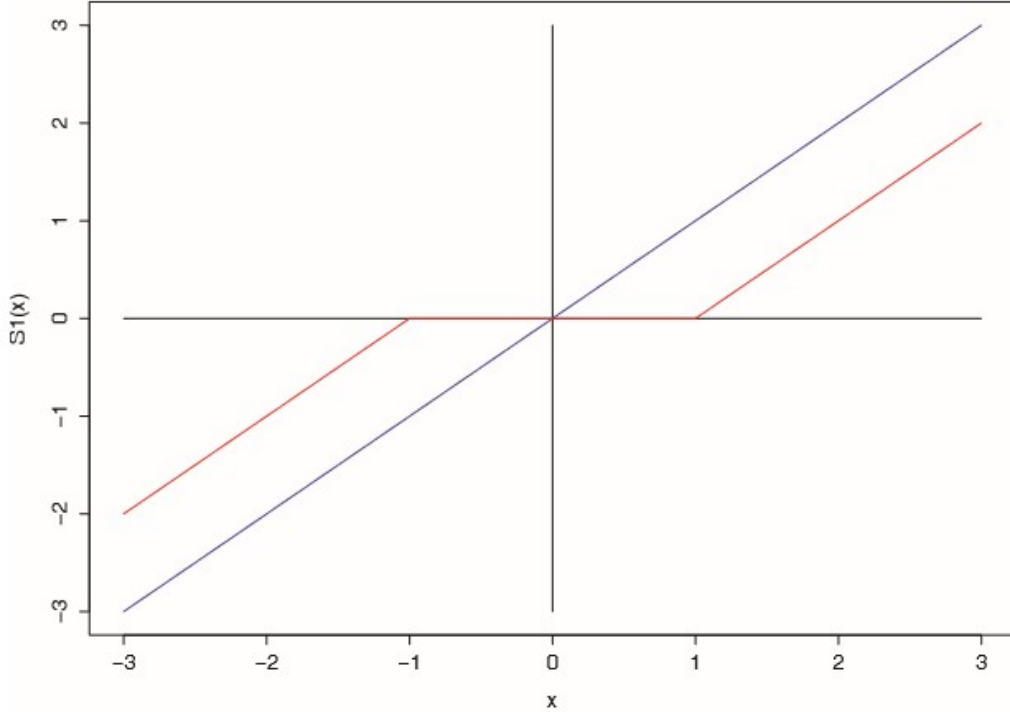


Figure 3-1: Soft-thresholding function

3.1.4.1 LASSO Single Variable Case

Before moving to a case involving multiple variables, a single variable case is considered. For this case, $p=1$ and $\mathbf{Y} = \mathbf{X}_1\boldsymbol{\beta}_1 + \varepsilon$, and the optimization problem can be written as

$$\underset{\boldsymbol{\beta} \in \mathbb{R}^p}{\operatorname{argmin}} \frac{1}{n} \|\mathbf{Y} - \mathbf{X}_1\boldsymbol{\beta}_1\|_2^2 + \lambda |\boldsymbol{\beta}_1| \quad (3.10)$$

Assuming $\hat{\boldsymbol{\beta}}_1$ is a solution to equation 3.10, then the sub-differential must contain zero, meaning

$$-\frac{2}{n} \mathbf{X}_1^T (\mathbf{Y} - \mathbf{X}_1\hat{\boldsymbol{\beta}}_1) + \lambda * \operatorname{sign}(\hat{\boldsymbol{\beta}}_1) = 0, \quad (3.11)$$

Which can be rewritten as

$$\frac{1}{n} \mathbf{X}_1^T (\mathbf{Y} - \mathbf{X}_1\hat{\boldsymbol{\beta}}_1) = \frac{\lambda}{2} \operatorname{sign}(\hat{\boldsymbol{\beta}}_1)$$

Note that since we are assuming the predictors are standardized, $\frac{1}{n} \mathbf{X}_1^T \mathbf{X}_1 = 1$,

$$\hat{\beta}_1 = \frac{1}{n} \mathbf{X}_1^T \mathbf{Y} - \frac{\lambda}{2} \text{sign}(\hat{\beta}_1) \quad (3.12)$$

$$\hat{\beta}_1 = \begin{cases} \frac{1}{n} \mathbf{X}_1^T \mathbf{Y} + \frac{\lambda}{2} & \text{if } \frac{1}{n} \mathbf{X}_1^T \mathbf{Y} < -\frac{\lambda}{2} \\ 0 & \text{if } \frac{1}{n} \mathbf{X}_1^T \mathbf{Y} \leq \frac{\lambda}{2} \\ \frac{1}{n} \mathbf{X}_1^T \mathbf{Y} - \frac{\lambda}{2} & \text{if } \frac{1}{n} \mathbf{X}_1^T \mathbf{Y} > \frac{\lambda}{2} \end{cases}$$

An alternative interpretation is that $\hat{\beta}_1 = \frac{1}{n} \mathbf{X}_1^T \mathbf{Y}$ is soft-thresholded by $\frac{\lambda}{2}$ such that

$$\hat{\beta}_1 = S_{\frac{\lambda}{2}}\left(\frac{1}{n} \mathbf{X}_1^T \mathbf{Y}\right) \quad (3.13)$$

Therefore, the LASSO estimator for a single variable case can be computed by soft-thresholding the OLS estimator by $\frac{\lambda}{2}$ or

$$\hat{\beta}_1 = S_{\frac{\lambda}{2}}(\hat{\beta}_{OLS}) \quad (3.14)$$

Where $\hat{\beta}_{OLS} = \frac{1}{n} \mathbf{X}_1^T \mathbf{Y}$.

3.1.4.2 Coordinate Descent for LASSO

In order to treat LASSO algorithmically, the objective function must be split into a differentiable part $fd = ||\mathbf{Y} - \mathbf{X}_j \beta_j||_2^2$ and a non-differentiable part $fc = \sum_{j=1}^p |\beta_j|$. The non-differentiable component $fc = \sum_{j=1}^p |\beta_j|$ is convex in each coordinate, allowing for a coordinate wise minimization to be utilized (Gauraha, 2018). Section 3.1.4.1 demonstrated that with a single predictor, the LASSO solution has a closed form solution with a soft-threshold version of the ordinary least squares estimate. Building on this, a coordinate descent algorithm for the LASSO can be implemented as follows.

Coordinate descent is an iterative method that solves one variable iteratively, while holding all other variables constant. For each coordinate sub-problem, each component of β is fixed except for the j th component β_j . By denoting \mathbf{X}_j as the j th column of \mathbf{X} and \mathbf{X}_{-j} denote all of the columns except for the j th column, then the problem can be rewritten as

$$\underset{\beta \in \mathbb{R}^p}{\operatorname{argmin}} \left\{ \frac{1}{n} \| \mathbf{Y} - \mathbf{X}_{-j} \beta_{-j} - \mathbf{X}_j \beta_j \|_2^2 + \lambda |\beta_j| + \lambda \sum_{l \neq j} |\beta_l| \right\} \quad (3.15)$$

Next, we define $r_j := \mathbf{Y} - \mathbf{X}_{-j} \beta_{-j}$ as the partial residual or the difference between the actual response \mathbf{Y} and the fitted model that excludes variable \mathbf{X}_j . The solution above becomes the univariate LASSO problem with vector r_j as the response variable

$$\underset{\beta \in \mathbb{R}^p}{\operatorname{argmin}} \left\{ \frac{1}{n} \| r_j - \mathbf{X}_j \beta_j \|_2^2 + \lambda |\beta_j| + \lambda \sum_{l \neq j} |\beta_l| \right\} \quad (3.16)$$

Now suppose $\hat{\beta}_j$ is a solution to the optimization problem above. Then the stationary condition yields the following

$$\begin{aligned} -\frac{2}{n} \mathbf{X}_j^T (r_j - \mathbf{X}_j \hat{\beta}_j) + \lambda * \operatorname{sign}(\hat{\beta}_j) &= 0, \\ \frac{1}{n} r_j^T \mathbf{X}_j - \hat{\beta}_j &= \frac{\lambda}{2} \operatorname{sign}(\hat{\beta}_j) \end{aligned} \quad (3.17)$$

The OLS estimator for the j th variable can then be computed as $\hat{\beta}_{OLS,j} = \frac{1}{n} r_j^T \mathbf{X}_j$. The univariate LASSO solution can then be computed by soft-thresholding the OLS estimator as

$$\hat{\beta}_j = S_{\frac{\lambda}{2}}((\hat{\beta}_{OLS})_j) \quad (3.18)$$

Table 3.1 demonstrates the full coordinate descent algorithm for LASSO. The dataset is loaded and initialized such that $\beta = 0$. Then for each j term, the single variable LASSO solution is computed. The entire process is repeated until $\hat{\beta} = \beta$.

Table 3-1: Full LASSO Coordinate Descent Algorithm

LASSO Coordinate Descent Algorithm**Input:** dataset (\mathbf{Y} , \mathbf{X})**Output:** $\hat{\beta}$:=LASSO estimated vector of regression coefficientsInitialize $\beta = 0$ **repeat** **for each** $j \in \{1, \dots, p\}$ **do** Compute the partial residual r_j , where

$$r_j = \mathbf{Y} - \sum_{l \neq j} \mathbf{X}^l \beta_l$$

Compute the OLS coefficient for single predictor

$$(\hat{B}_{OLS})_j = \frac{1}{n} r_1^T \mathbf{X}_j$$

 Update β_j (LASSO solution: single variable case)

$$\beta_j = S_{\frac{\lambda}{2}}((\hat{B}_{OLS})_j)$$

end**until** convergence; $\hat{\beta} = \beta$ **Return** $\hat{\beta}$ **3.1.4.3 Coordinate Descent for Elastic Net**

The derivation and steps to calculate the Elastic Net penalty via coordinate descent are similar to those taken to calculate the LASSO penalty (Yang, 2013). The second order penalty adds an additional term to the LASSO solution such that

$$\underset{\beta \in \mathbb{R}^p}{\operatorname{argmin}} \frac{1}{n} \|\mathbf{Y} - \mathbf{X}_1 \beta_1\|_2^2 + P_{\lambda, \alpha}(\beta) \quad (3.19)$$

Where $P_{\lambda,\alpha}(\beta)$ is the Elastic Net penalty defined as

$$P_{\lambda,\alpha}(\beta) = \lambda \sum_{j=1}^p p_\alpha(\beta_j) = \lambda \sum_{j=1}^p \left[\frac{1}{2}(1-\alpha)\beta_j^2 + \alpha|\beta_j| \right]$$

Note that when $\alpha = 1$, the Elastic Net reduces to the LASSO equation. When each predictor shows a strong correlation, some $\alpha < 1$ should be used. For each fixed λ , coordinate descent is used to solve the Elastic Net. Once again, we define a current residual $r_j := \mathbf{Y} - \mathbf{X}_{-j}\beta_{-j}$ that excludes the jth term from each calculation. To update the estimate for β_j , the univariate Elastic Net problem is solved by

$$\hat{\beta}_j = \underset{\beta \in \mathbb{R}^p}{\operatorname{argmin}} \left\{ \frac{1}{n} \|r_j - \mathbf{X}_j\beta_j\|_2^2 + \lambda p_\alpha(\beta_j) \right\} \quad (3.20)$$

The soft threshold is applied, leading to

$$\hat{\beta}_j = \frac{S(\frac{1}{n}r^T \mathbf{X}_j + \beta_j, \lambda\alpha)}{1 + \lambda(1 - \alpha)} \quad (3.21)$$

Table 3.2 demonstrates the full coordinate descent algorithm for Elastic Net. The dataset is loaded and initialized such that $\beta = 0$. Then for each j term, the single variable Elastic Net solution is computed. The entire process is repeated until $\hat{\beta} = \beta$.

Table 3.2: Full Elastic Net Coordinate Descent Algorithm

Elastic Net Coordinate Descent Algorithm

Input: dataset (\mathbf{Y}, \mathbf{X})

Output: $\hat{\beta}$:=Elastic Net estimated vector of regression coefficients

Initialize $\beta = 0$

repeat

for each $j \in \{1, \dots, p\}$ **do**

 Compute the partial residual r_j , where

$$r_j = \mathbf{Y} - \sum_{l \neq j} \mathbf{X}^l \beta_l$$

 Update β_j (Elastic Net solution: single variable case)

$$\hat{\beta}_j = \frac{S(\frac{1}{n} r^T \mathbf{X}_j + \beta_j, \lambda\alpha)}{1 + \lambda(1 - \alpha)}$$

end

until convergence;

$\hat{\beta}_j = \beta_j$

Return $\hat{\beta}$

3.1.5 Cross Validation

Cross validation is a method to perform out-of-sample testing to assess the results of statistical analysis on an independent data set. After the experimental and simulated data are processed and separated into \mathbf{X} and \mathbf{Y} vectors, the full data set is split into testing and training subsets via the holdout method shown in figure 3-2. As a result of splitting the data, additional bias is introduced to each solution, as different parts of the data are either included or removed from the model selection process. Cross validation is used to perform the test-train split process multiple times, averaging each solution to provide a less biased solution as seen in figure 3-3. Cross validation is used to find the optimal normalization parameter for both LASSO and Elastic Net.

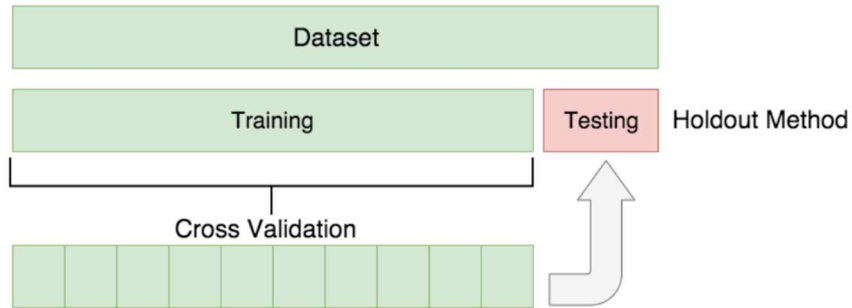


Figure 3-2: Holdout method for test-train split

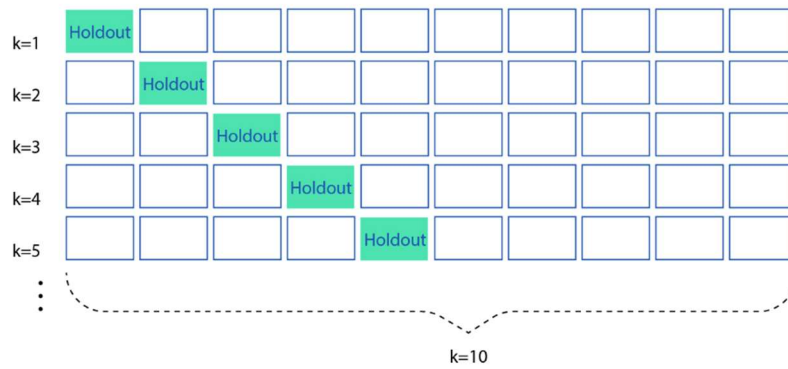


Figure 3-3: Cross validation holdout

CHAPTER 4

Kansas State Experiment

4.1 Data Collection

4.1.1 Kansas State Experimental Data

In section 1.2, the Kansas State University benchmarking tool and experimental facility were described. Five separate experimental runs were conducted for tap water, pure sand, sand with water, pure limestone, and limestone with water. For each of these experimental runs, the data collection sequence involved:

- 1) Source calibration runs to adjust gain on detection systems
- 2) Pre-run background tests (5 minutes)
- 3) Live D-T run (1 hour)
- 4) Post-run background tests (5 minutes)

The data collected during each of these runs was processed by Kansas State University and converted into counts per channel text files for each detector. Additional binary files were provided that have time dependent information for the pulsing sequence and detector responses with respect to time.

The counts per channel data files must be processed and converted to energy to match the simulated responses. A second order polynomial is used for fitting purposes by

$$\text{Energy} = a + b * \text{channel} + c * \text{channel}^2 \quad (4.1)$$

4.1.2 Simulated Data

In order to simulate an accurate detector response, extensive ($\sim 10^9$ particles) MCNP 6.1 calculations were conducted with accurate details of the detector, tool, test chamber, and surrounding medium geometry and materials. Libraries were created by using F8 tallies for each detector and medium (water, sand, limestone, etc.). To accurately model the detector response, Gaussian broadening functions were used in order to take the pulse response and broaden the data to match the FWHM found using the calibration sources.

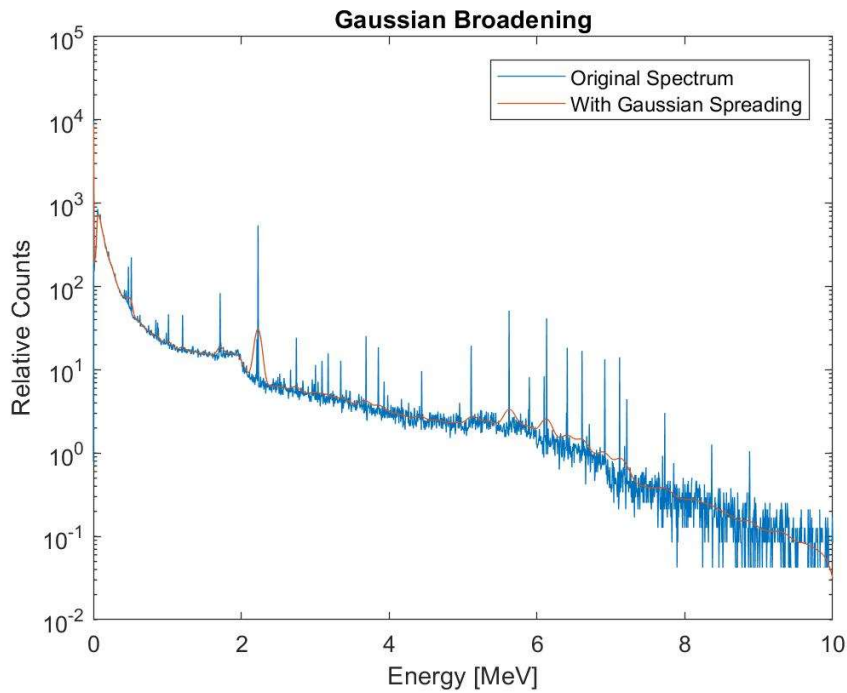


Figure 4-1: F8 tally simulated response and Gaussian broadened detector response

4.1.3 Simulated Example

Prior to running a full example with data from Kansas State University, a simulated example was conducted to demonstrate the capabilities of each code. Using simulated data, a salt water test case was created by combining a combination of water, sodium, and chlorine libraries. Random Poisson distributed noise was then applied to the test case to simulate the random effects found in true examples. Five total libraries were used as training data sets (water, sodium, chlorine, iron, and copper) to train the model versus the test data set containing salt water. Using 10-fold

cross validation, the model was correctly trained to fit only the 3 libraries that contribute to the full spectrum, while providing a zero contribution for the iron and copper libraries. Figures 4-2 thru 4-7 demonstrate how the tuning parameters select the best model and the final fits for LASSO and Elastic Net.

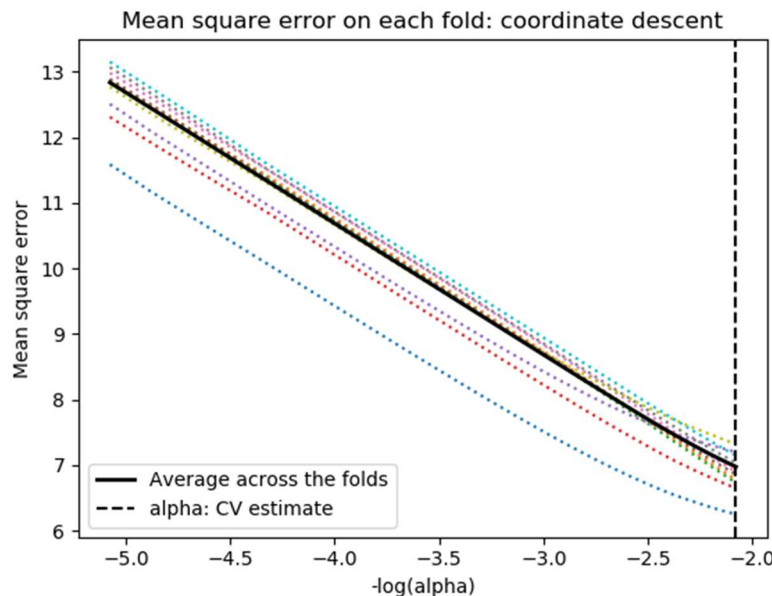


Figure 4-2: Cross validation normalization parameter selection for LASSO

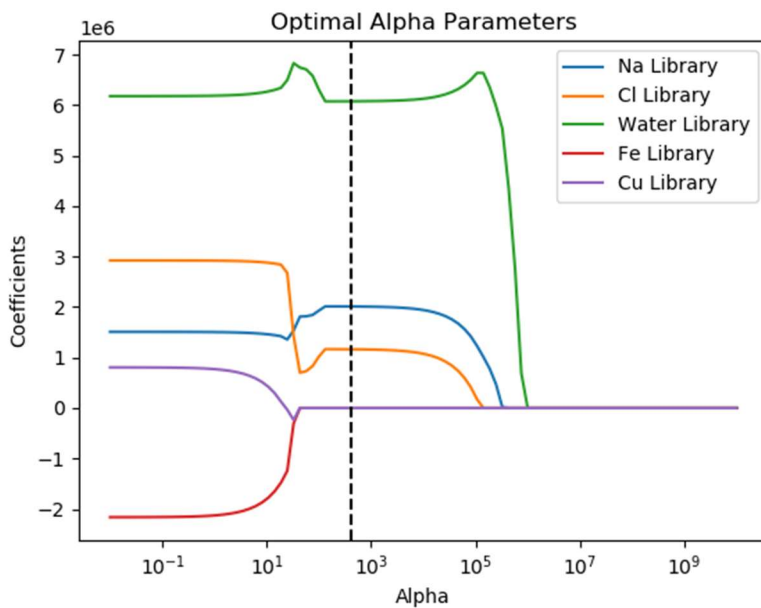


Figure 4-3: LASSO model selection coefficients by changing normalization parameter

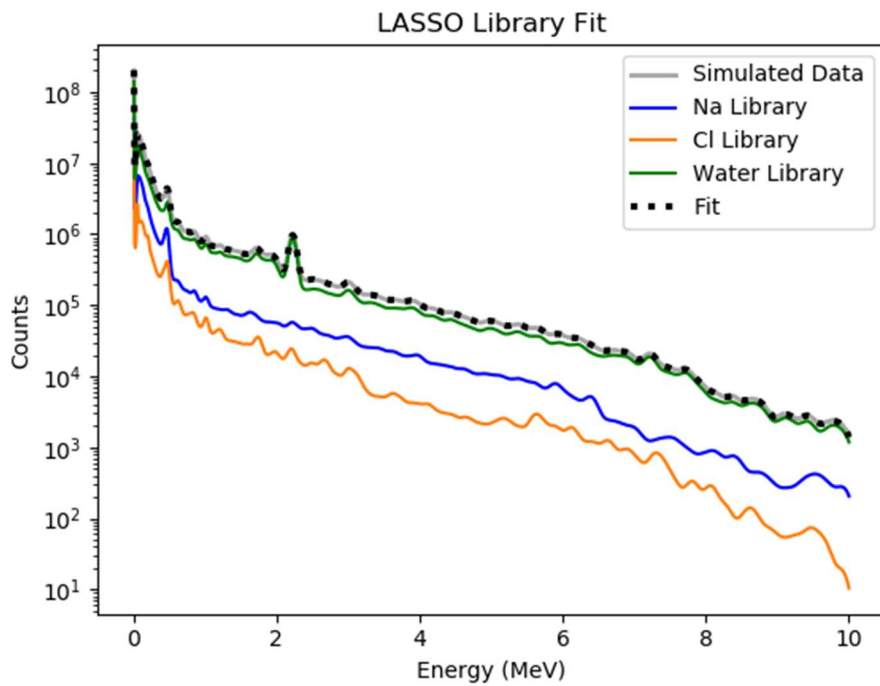


Figure 4-4: LASSO salt water simulation fit

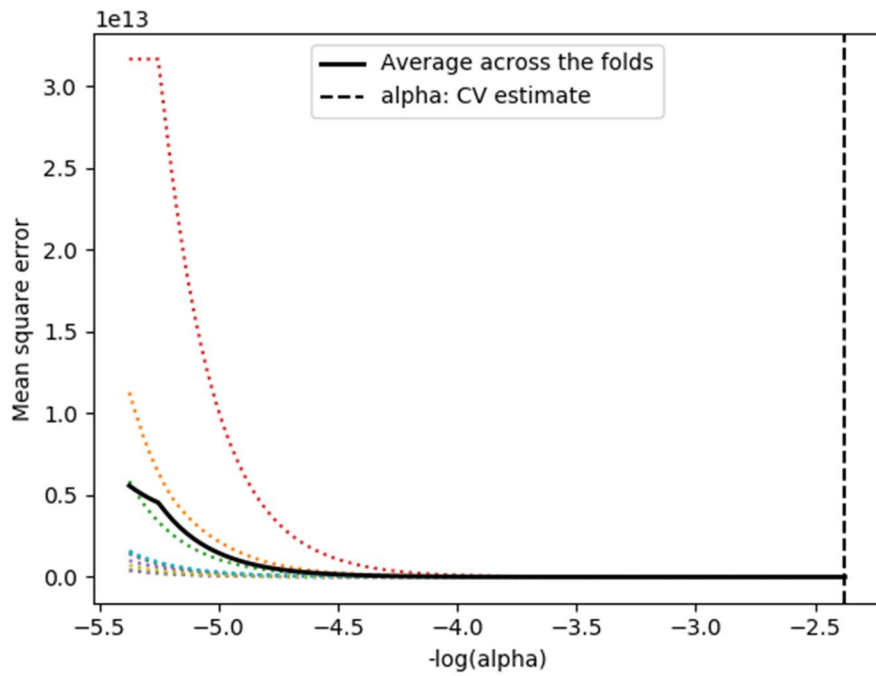


Figure 4-5: Cross validation normalization parameter selection for Elastic Net

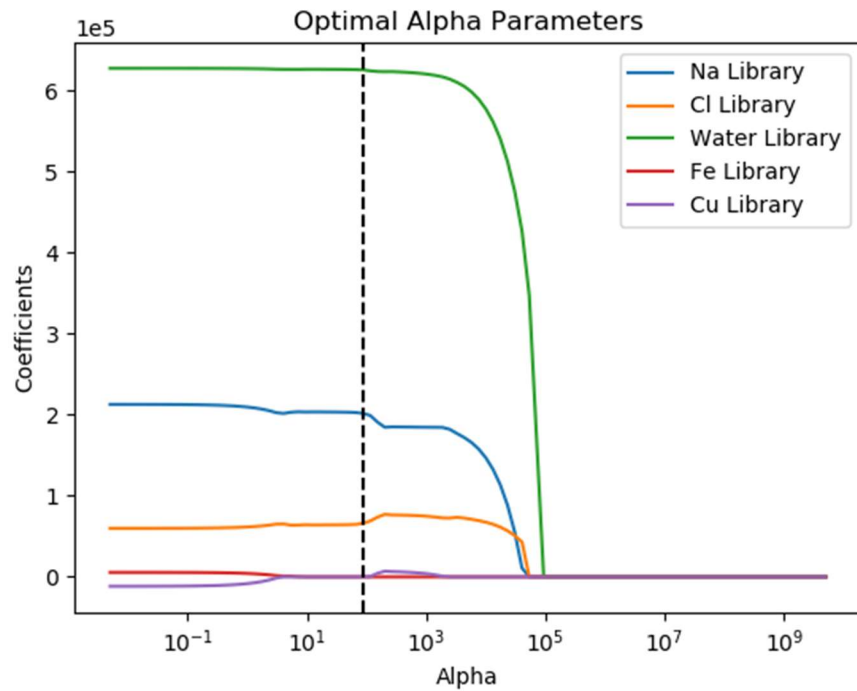


Figure 4-6: Elastic Net model selection by changing normalization parameter

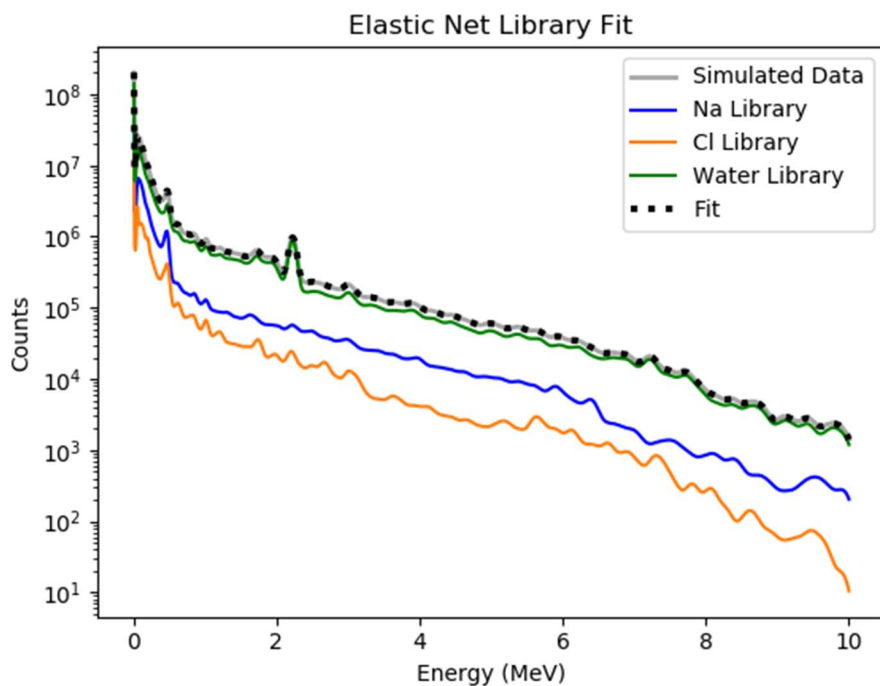


Figure 4-7: Elastic Net salt water simulation fit

When the normalization parameter is increased, the penalty for each term becomes greater, allowing the shrinkage and removal of parameters. The MSE at each alpha parameter is compared, settling on the best overall fit for the final solution. Without putting the output of the LASSO and Elastic Net fits into an OLS program for a final fit, table 4-1 displays the relative error of each method averaged over 10 runs.

Table 4-1: Relative error of the two methods

Relative Error		
	Elastic Net	LASSO
Water	5.01%	0.07%
Na	2.95%	1.32%
Cl	7.95%	3.65%

4.2 Methods and Improvements

4.2.1 Full Procedure

Before any data analysis can take place, a variety of preprocessing and post processing of data is necessary (Fig. 4-8). Experimental and simulated data are generated at Kansas State and North Carolina State, respectively. The experimental data is processed and separated into counts per channel text files for each detector type, as well as binary files with time dependent data. The detector data is converted into energy bins using calibration sources for empirical FWHM calculations.

The simulated data is generated using MCNP 6.1 using the F8 tally. The nonlinear response in the Gaussian broadening detector response function is addressed, resulting in a final library spectrum.

Each library is added to a single file and used to train the fitting model. A 10-fold cross validation process helps reduce the overall bias in model selection. For the test/train split, 90% of the data is used each time for training, while 10% of the data is held out to test the model. LASSO and Elastic Net are applied to select the best model that reduces a loss function (MSE). Once the final solution is reached, the output from LASSO and Elastic Net are used as initial guesses in an ordinary least squares fitting using CEARLLS.

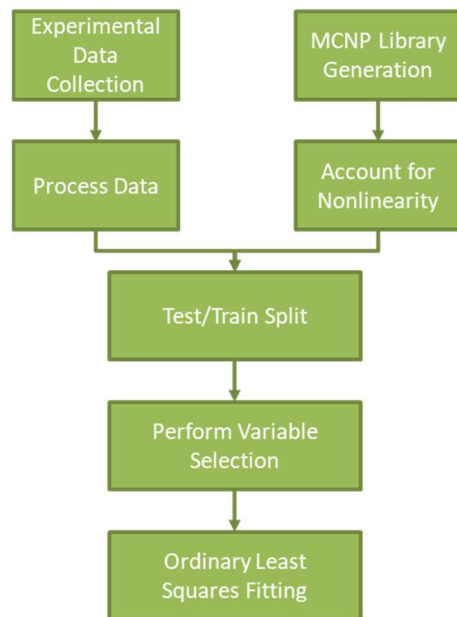


Figure 4-8: Full procedure

4.2.2 Early Lessons Learned

A pure water trial was conducted and processed by the procedure laid out in section 4.2.1. Upon completing the final fitting, several deviations were observed as seen in Figure 4-9. In the high energy range, above 7 MeV, differences between the simulated and experimental response are expected, as the error in each channel is high from the low count rate. The hydrogen peak and oxygen peaks fit well to the simulations, however, the region below 2 MeV does not have a proper fitting. The proposed solution was to look at the activation of the NaI crystal (Gardner, 2000).

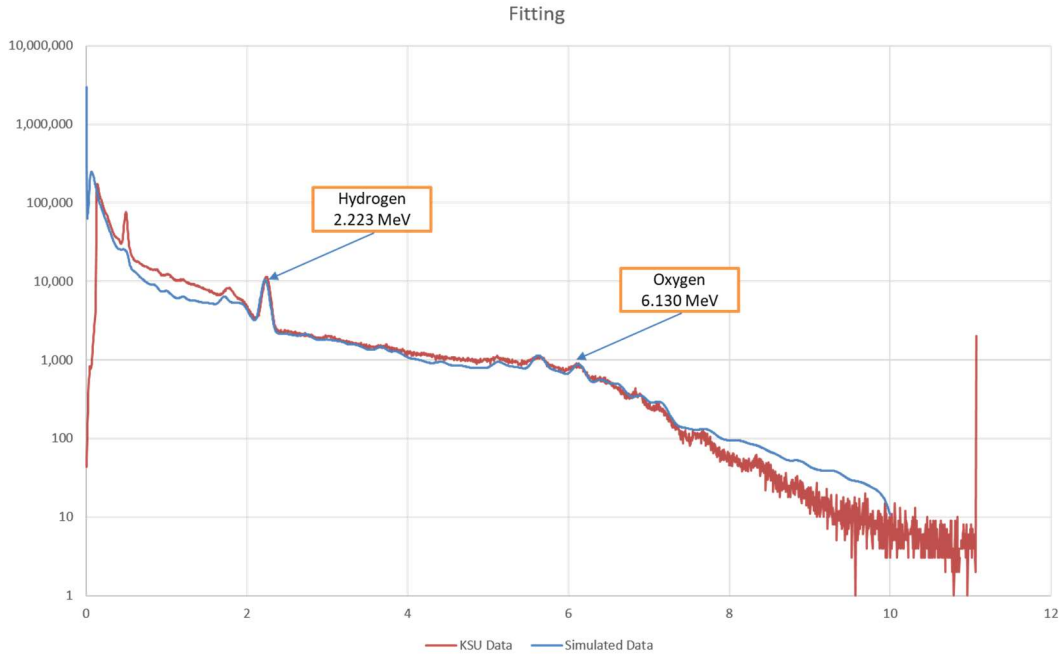


Figure 4-9: Pure water first fit

To test this theory, a library response for activated Sodium and Iodine are added to the fitting libraries (Fig. 4-10). Although this did improve the overall fit, it did not completely resolve the discrepancies.

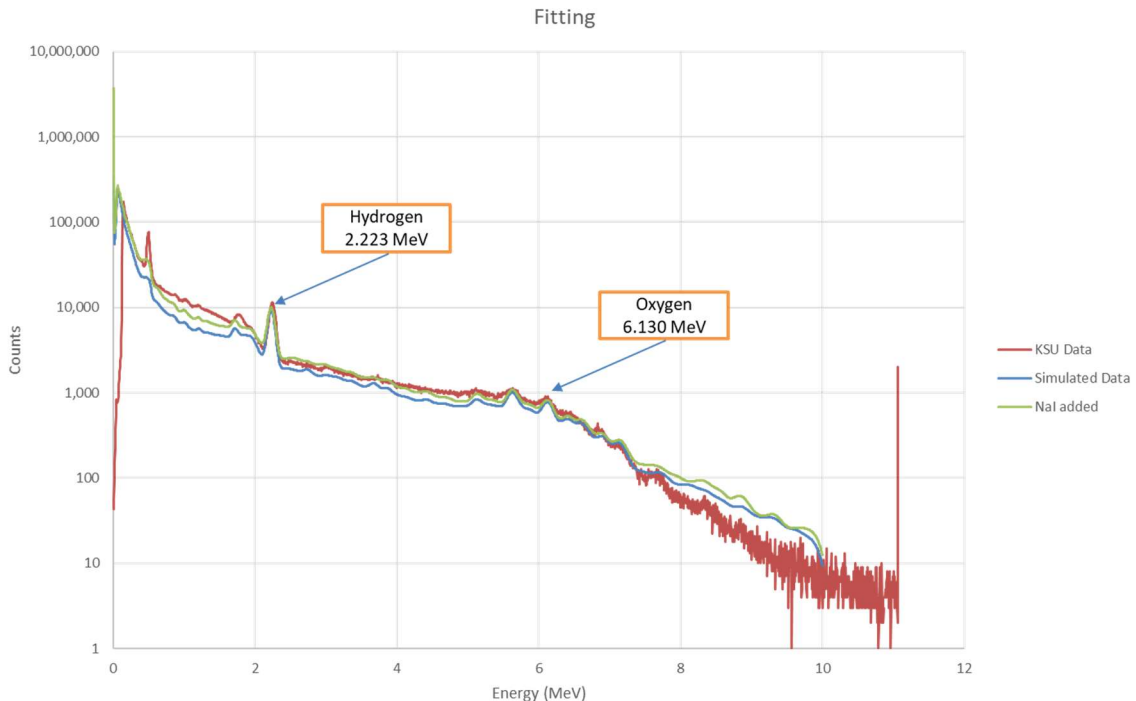


Figure 4-10: Pure water fit with NaI activation libraries added

To completely understand the nature of the activated (delayed) response, the time dependent D-T data is necessary. The primary advantage of using a PNG is the ability to read signatures that are prompt and delayed by the response times. The PNG is triggered using a firing sequence from the generator and a pulse of neutrons is emitted. After the pulse, there is a window of time before the next initialization where the neutrons have died off, and the only remaining signatures are from delayed activation (Figs. 4-11, 4-12).

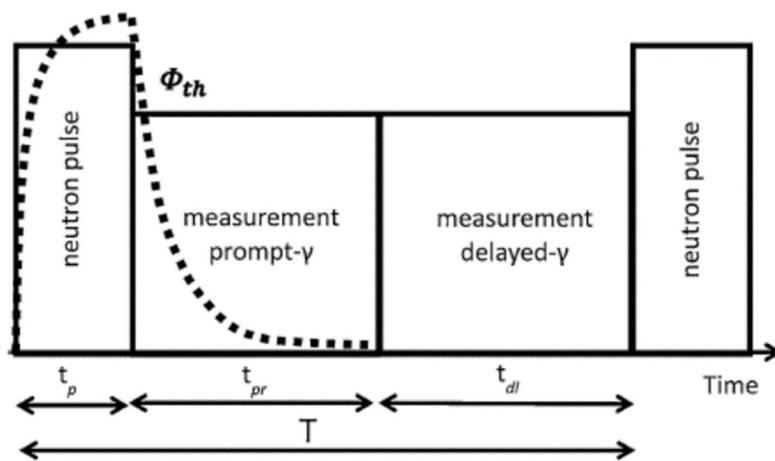


Figure 4-11: Firing sequence and measured response

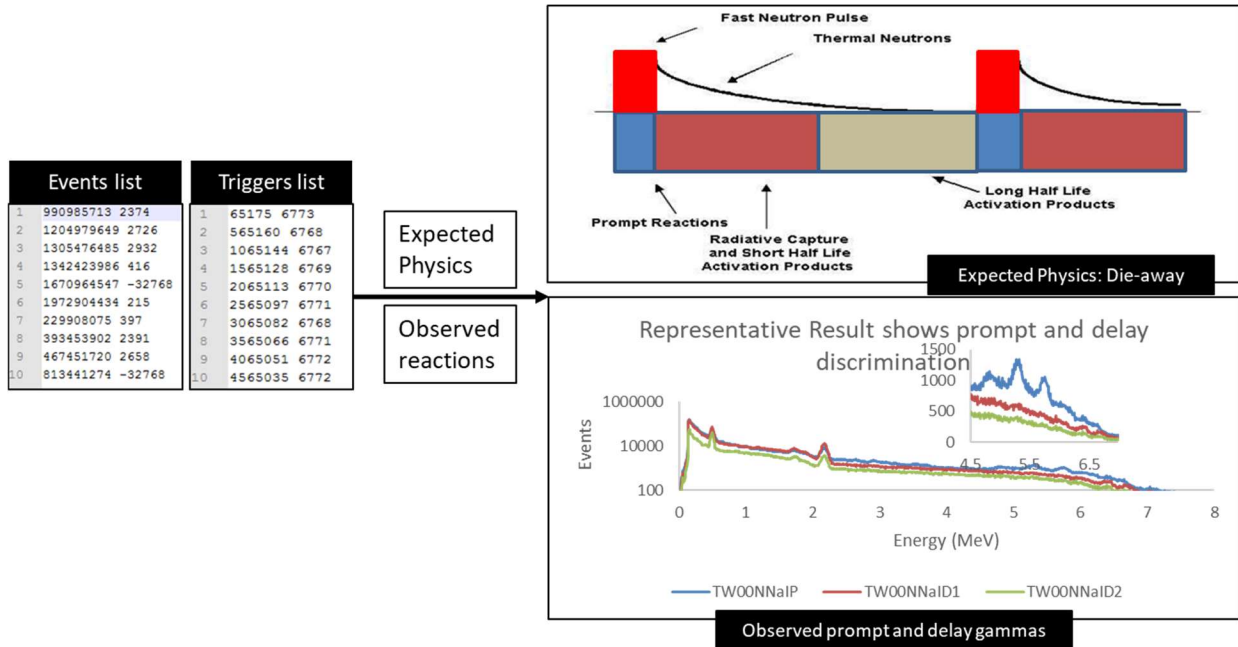


Figure 4-12: Time dependent format distributed by Kansas State University

4.3 Kansas State Experimental Results

Five separate trials were conducted to provide an experimental basis for this investigation. A water, sand, sand with water, limestone, and limestone with water trial were conducted to provide a broad range of materials and conditions to simulate, fit, and compare to methods currently implemented in the oil well logging industry. Using the post run background measurements, the delayed response is extracted and removed from the final response. The gaussian broadening parameters used for each of these trials was extracted by the method described in section 2.3 as

$$FWHM = 0.031 * E^{0.5} \quad (4.2)$$

MCNP simulated responses are separated into water, sand, limestone, iron, and copper libraries for near and far detectors and broadened by the parameters in eq. 4.2. The variable selection codes take the experimental response for each detector separately and provide a model prediction against the five input libraries for that detector. This process is repeated for both the near and far detectors for each trial run, followed by a final ordinary least squares fitting and error analysis.

The first 200 and final 548 channels are ignored from the variable selection and final fitting steps.

4.3.1 Water Trial

The first trial was conducted using tap water. The channel to energy conversion was accomplished by identifying the peak centroids in the sample and adjusting by

$$\text{Energy(MeV)} = -.01 + .005 * \text{channel} + 2e^{-7} * \text{channel}^2 \quad (4.3)$$

The cross-validation curve (figs. 4-13, 4-17, 4-21, 4-25) demonstrates the process by which the normalization parameter is selected by LASSO and Elastic Net for the near and far detectors.

The optimum normalization parameter is presented on the regularization path (figs. 4-14, 4-18, 4-22, 4-26) tracking the coefficients for each library as the normalization parameter changes.

The output from the LASSO and Elastic Net codes are presented in figures 4-15, 4-19, 4-23, and 4-27 using only channels 200 thru 1500. The remaining figures provide the full fit using the coefficients determined using the truncated dataset.

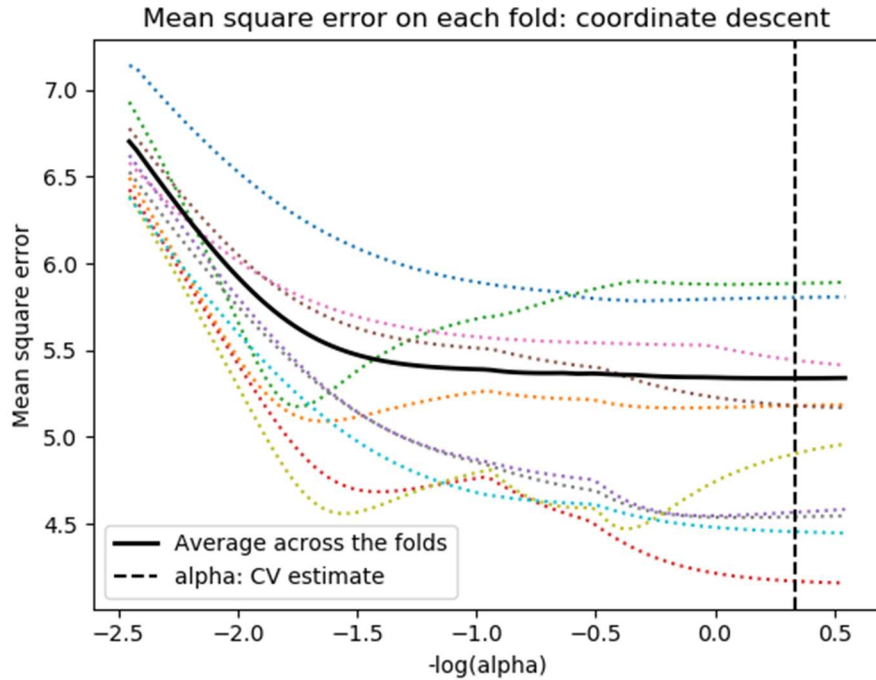


Figure 4-13: Cross validation normalization parameter selection for the LASSO near detector water trial

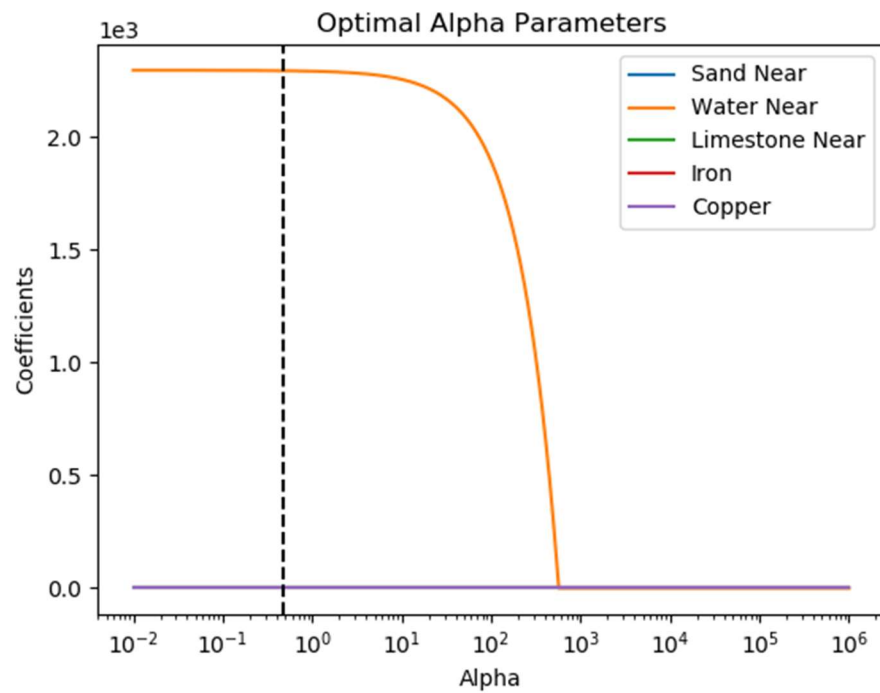


Figure 4-14: LASSO model selection coefficients by changing the normalization parameter for the near detector water trial

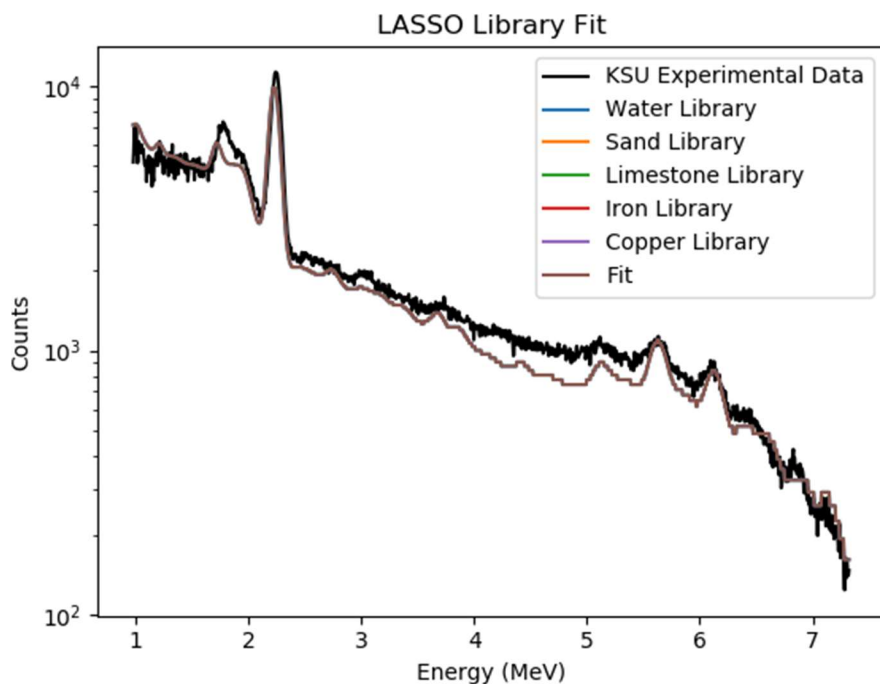


Figure 4-15: LASSO fit for the near detector water trial

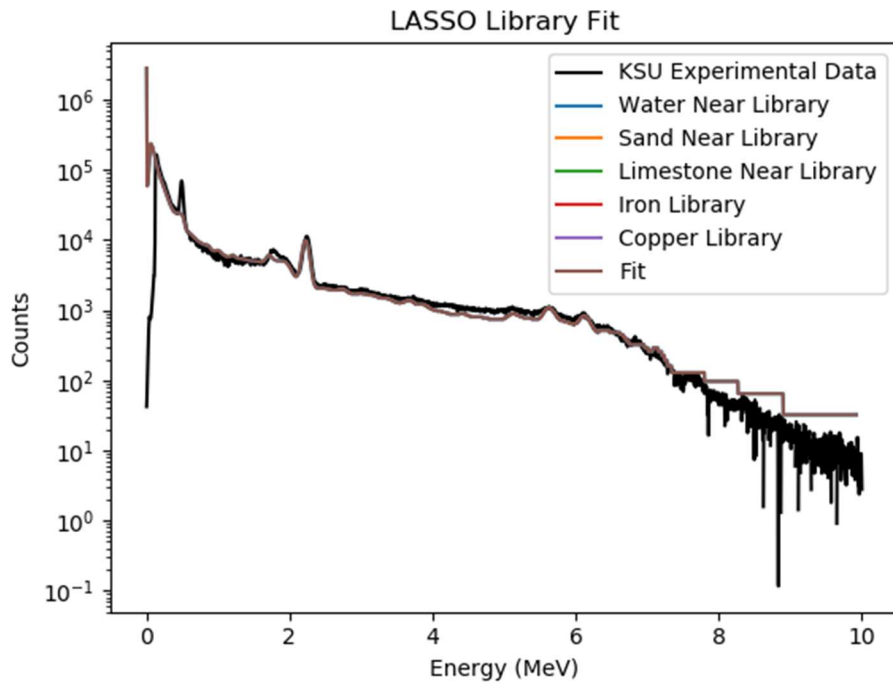


Figure 4-16: LASSO full fit for the near detector water trial

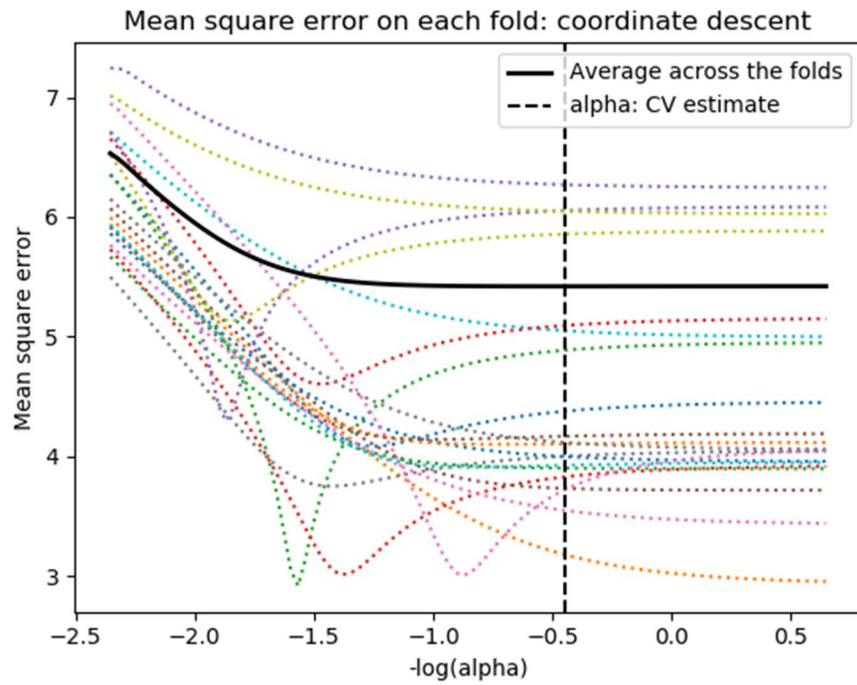


Figure 4-17: Cross validation normalization parameter selection for the Elastic Net near detector water trial

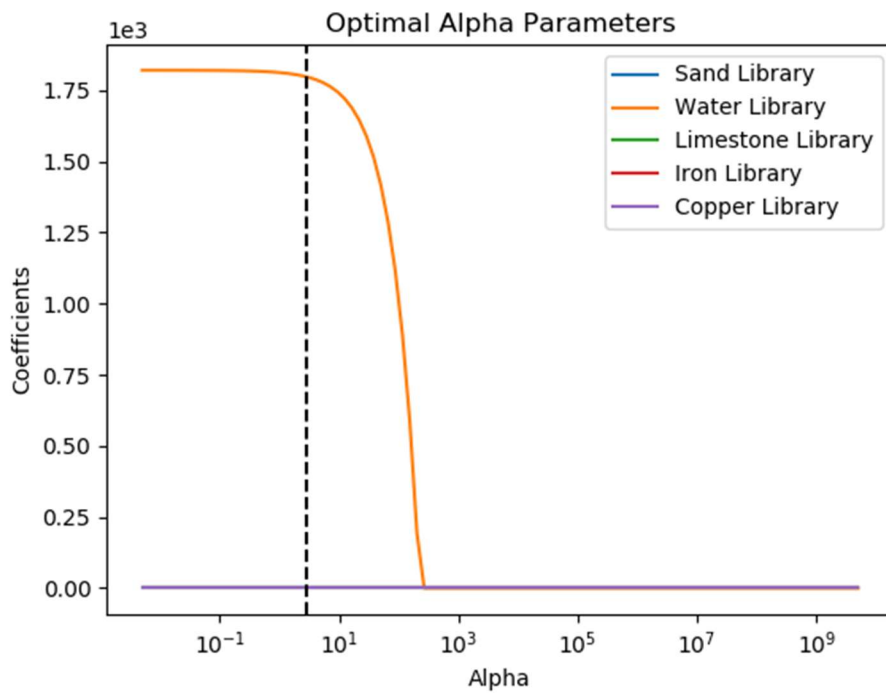


Figure 4-18: Elastic Net model selection coefficients by changing the normalization parameter for the near detector water trial

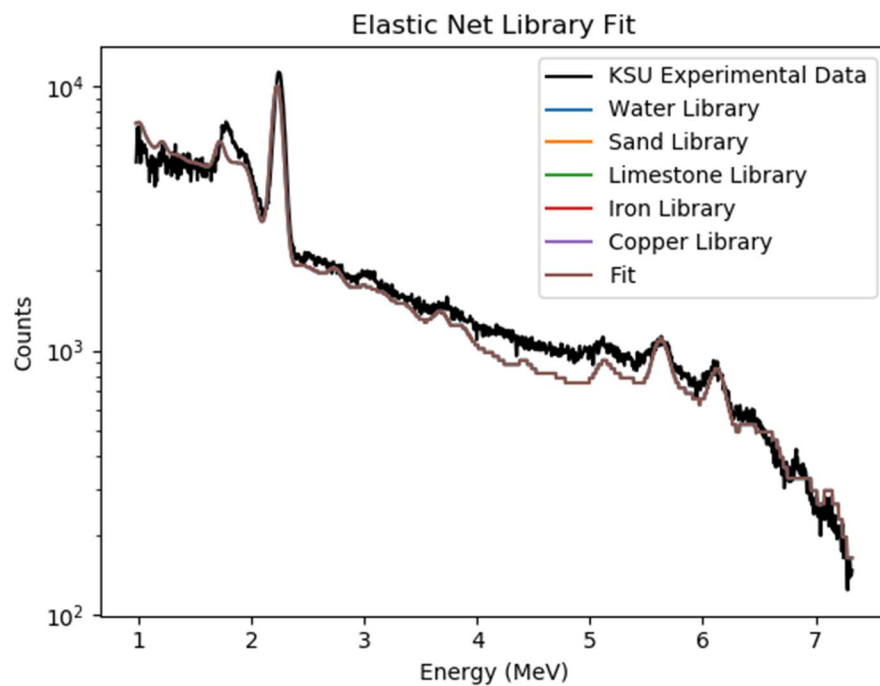


Figure 4-19: Elastic Net fit for the near detector water trial

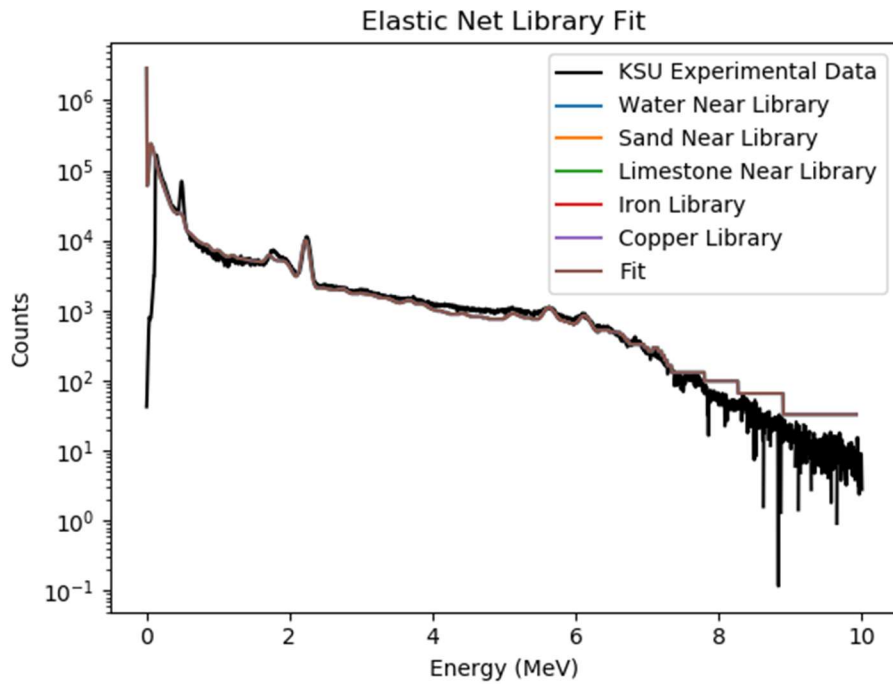


Figure 4-20: Elastic Net full fit for the near detector water trial

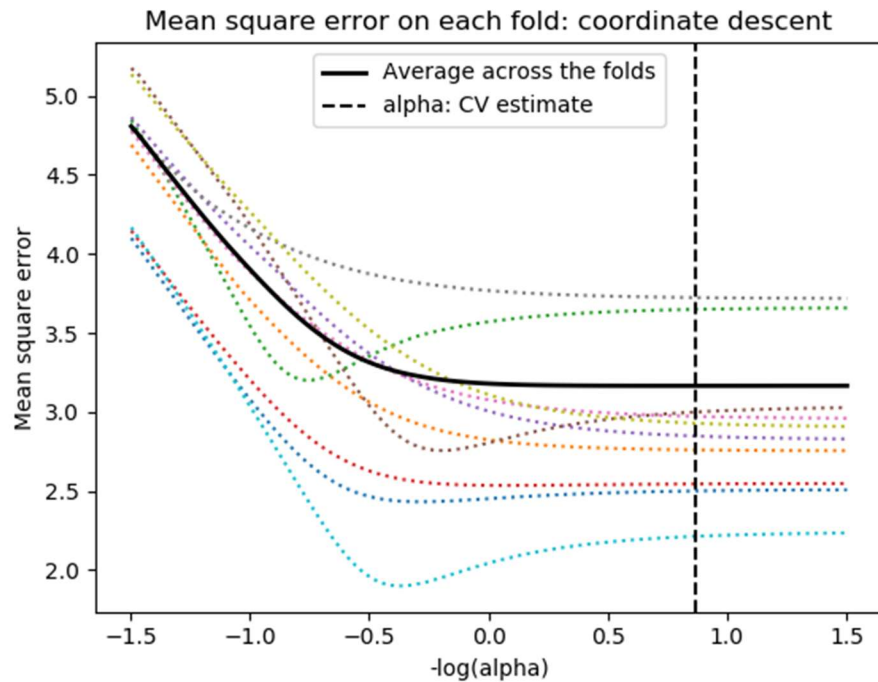


Figure 4-21: Cross validation normalization parameter selection for the LASSO far detector water trial

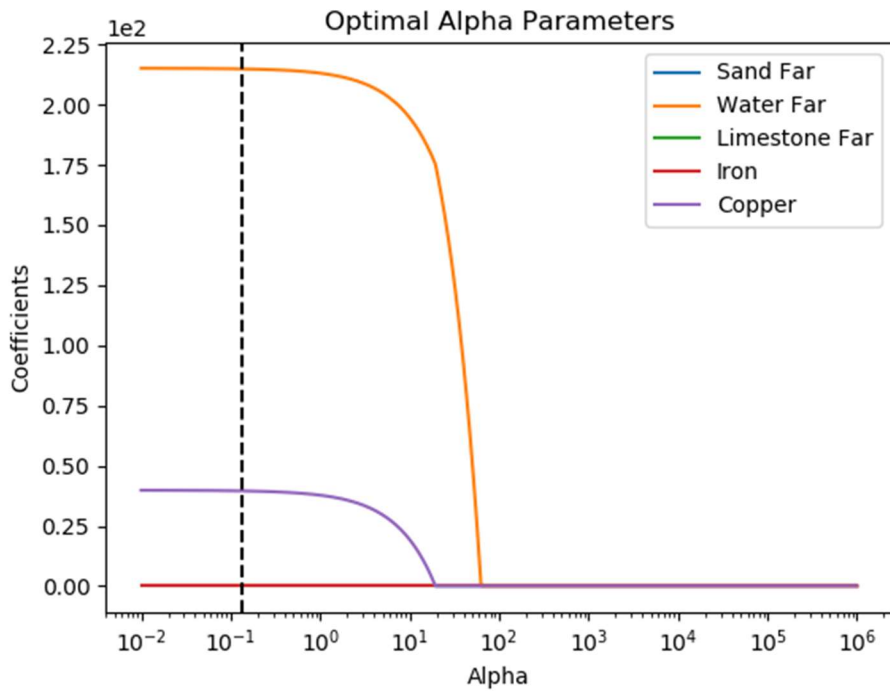


Figure 4-22: LASSO model selection coefficients by changing the normalization parameter for the far detector water trial

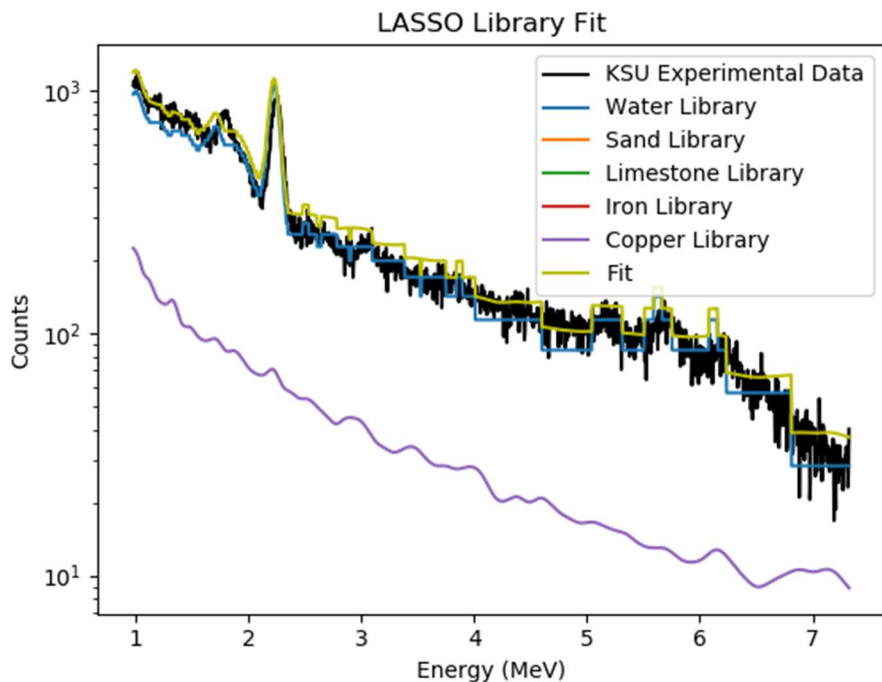


Figure 4-23: LASSO fit for the far detector water trial

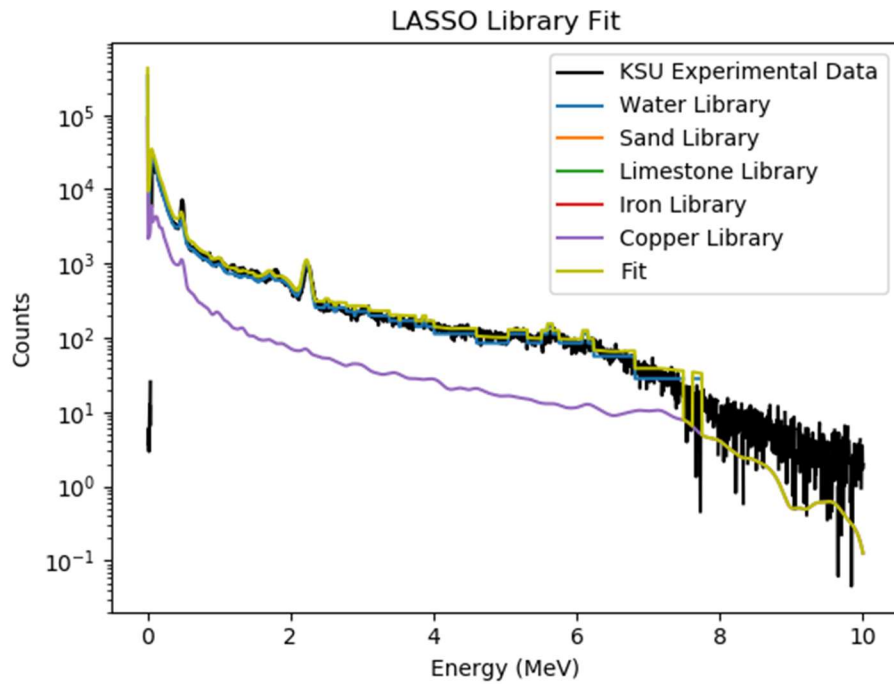


Figure 4-24: LASSO full fit for the far detector water trial

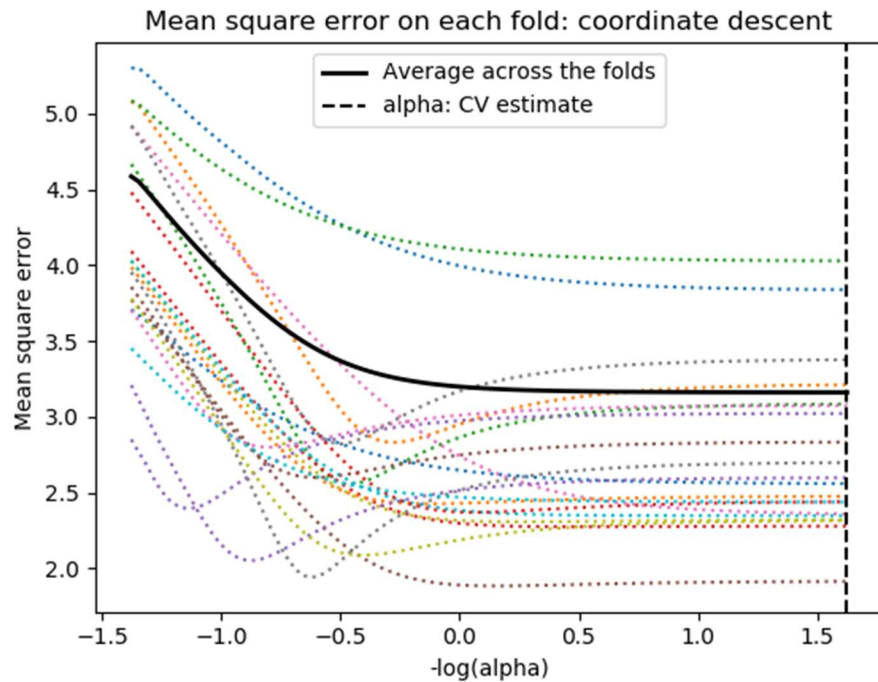


Figure 4-25: Cross validation normalization parameter selection for the Elastic Net far detector water trial

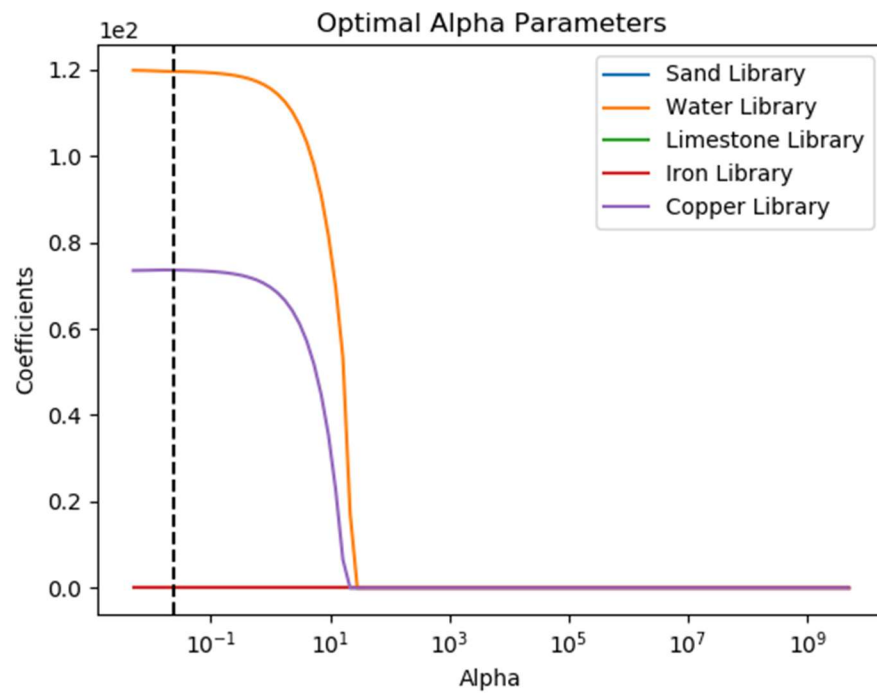


Figure 4-26: Elastic Net model selection coefficients by changing the normalization parameter for the far detector water trial

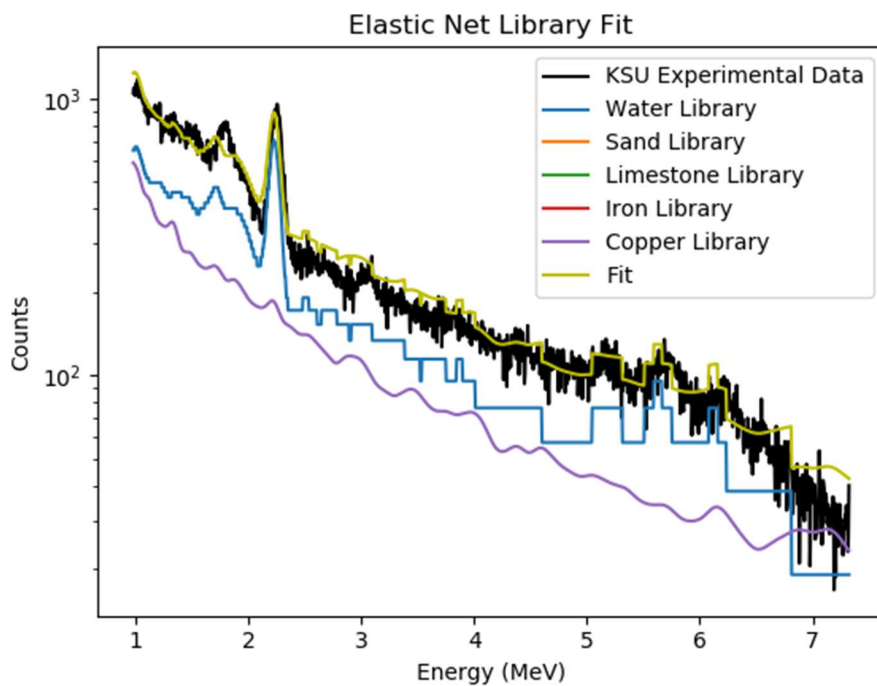


Figure 4-27: Elastic Net fit for the far detector water trial

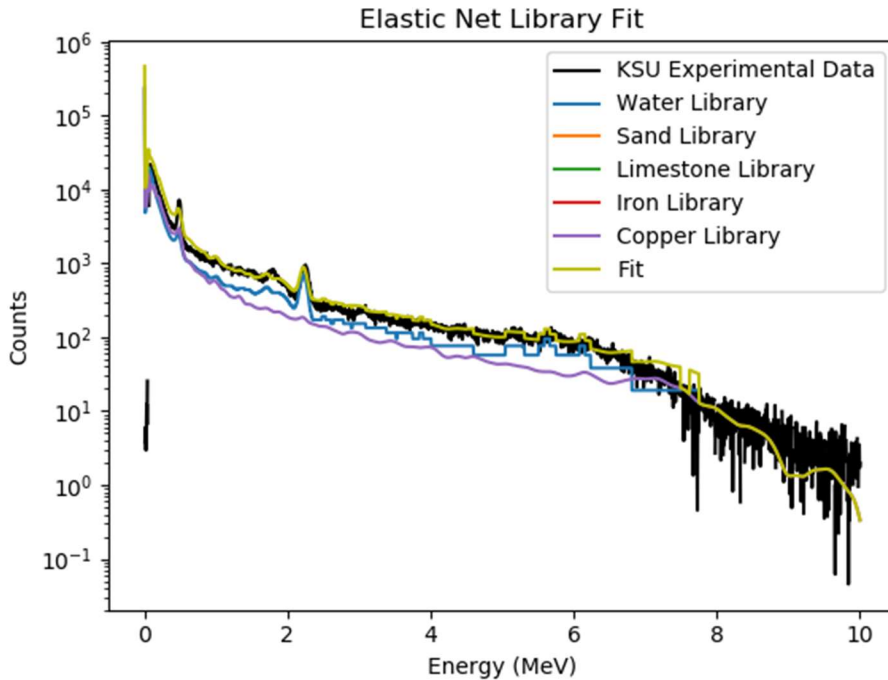


Figure 4-28: Elastic Net full fit for the far detector water trial

The results show that both LASSO and Elastic Net perform similarly for the near and far detectors. Each correctly identifies the presence of water alone for the near detector, while both misidentifying a copper contribution for the far detectors. Table 4-2 lists the optimal normalization parameters for each case identified by cross validation. The results for the variable selection process are used as inputs for the final ordinary least squares fitting using the cearlls code. Figures 4-29 and 4-30 display the final fitting and residuals for the near and far detector, respectively. Figure 4-31 shows the near and far final fits together. Tables 4-3, 4-4 provide the chi-squared value, fitting coefficients, and corresponding error for the near and far detectors.

Table 4-2: Optimal normalization parameters for water trial

Water Normalization Parameters		
	Near Detector	Far Detector
LASSO	0.464	0.136
Elastic Net	2.783	0.024

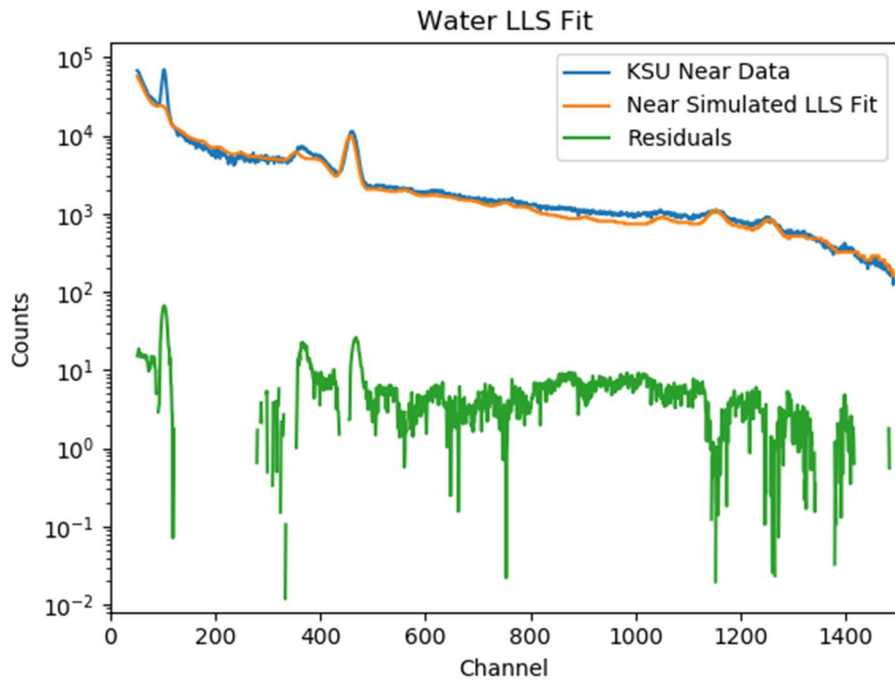


Figure 4-29: Linear least squares fit and residual for the near detector water trial

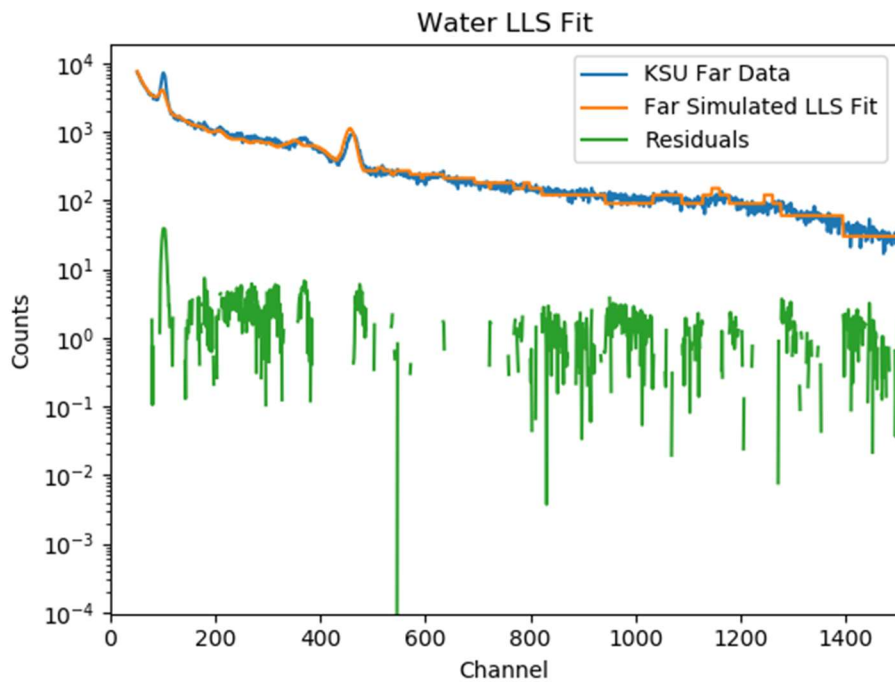


Figure 4-30: Linear least squares fit and residual for the far detector water trial

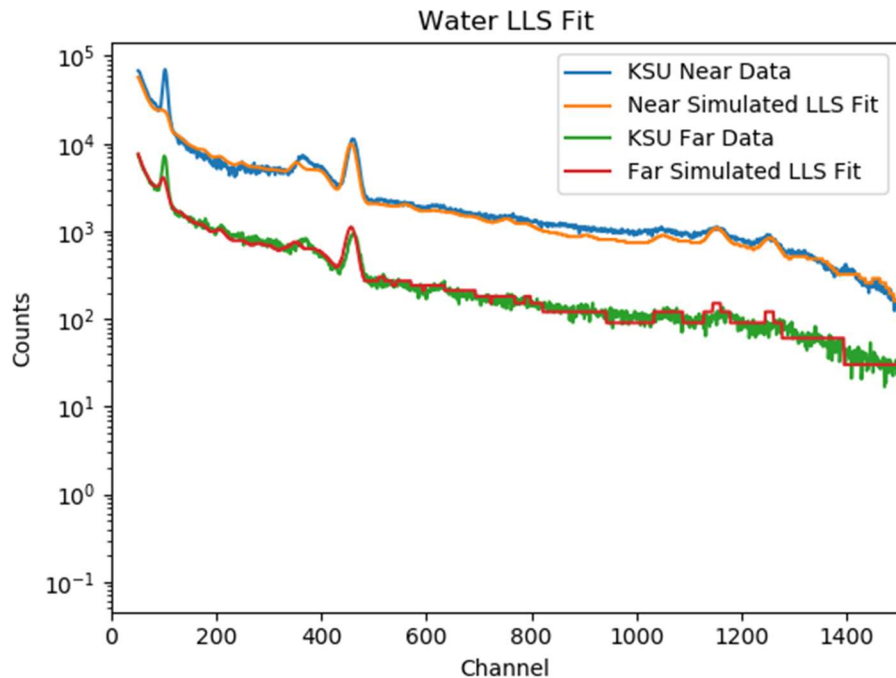


Figure 4-31: Linear least squares fit for near and far detector water trials

Table 4-3: Linear coefficients and error for water near detector

Water Linear Least Squares Results – Near Detector		
Chi-Squared = 99.3	Coefficients	Error
Water	322.6	.051
Sand	NA	NA
Limestone	NA	NA
Iron	NA	NA
Copper	NA	NA

Table 4-4: Linear coefficients and error for water far detector

Water Linear Least Squares Results – Far Detector		
Chi-Squared = 13.3	Coefficients	Error
Water	301.9	.12
Sand	NA	NA
Limestone	NA	NA
Iron	NA	NA
Copper	NA	NA

4.3.2 Sand Trial

The next trial conducted involved pure sand. No chemical or other analysis was performed on the material, so it is assumed that the makeup is SiO₂. The channel to energy conversion was accomplished by identifying the peak centroids in the sample and adjusting by

$$\text{Energy(MeV)} = -.051 + .00511 * \text{channel} + 1e^{-7} * \text{channel}^2 \quad (4.4)$$

All other parameters and order of figures are consistent with those from section 4.3.1. As a test to the versatility of LASSO and Elastic Net, each spectrum was shifted by 5 channels in the sand trial to demonstrate how each solves an ill conditioned case.

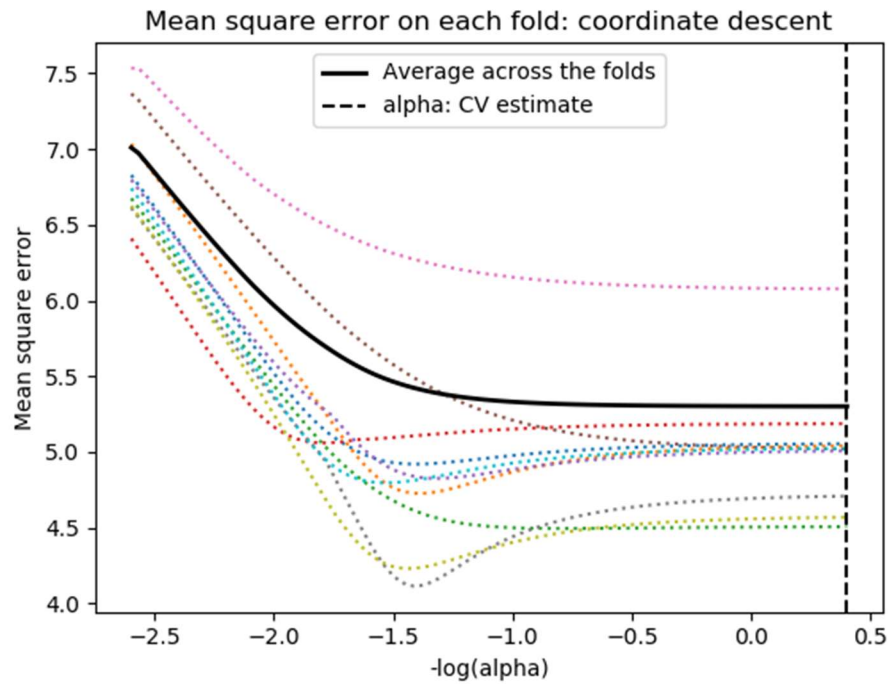


Figure 4-32: Cross validation normalization parameter selection for the LASSO near detector sand trial

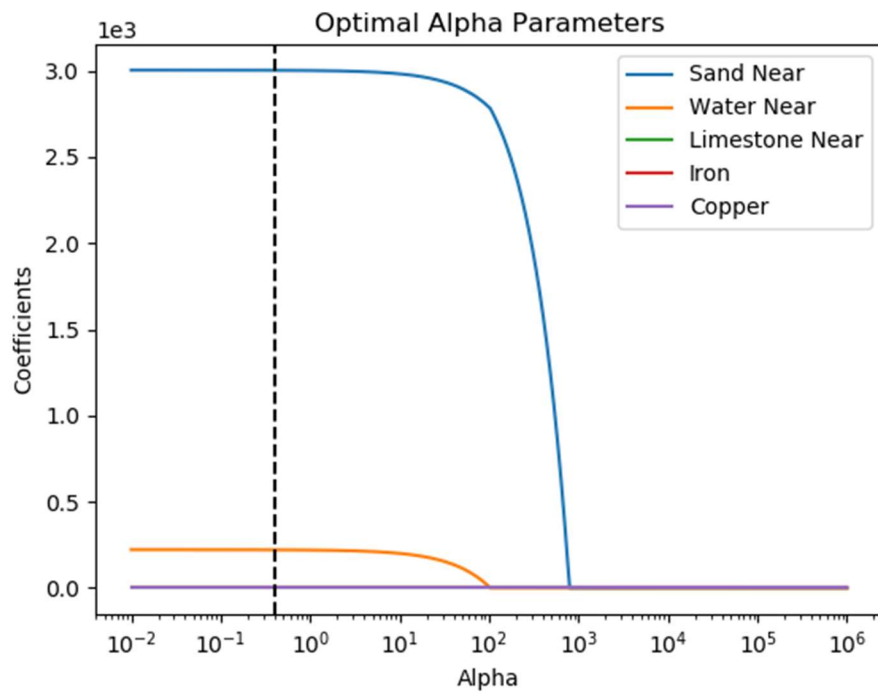


Figure 4-33: LASSO model selection coefficients by changing the normalization parameter for the near detector sand trial

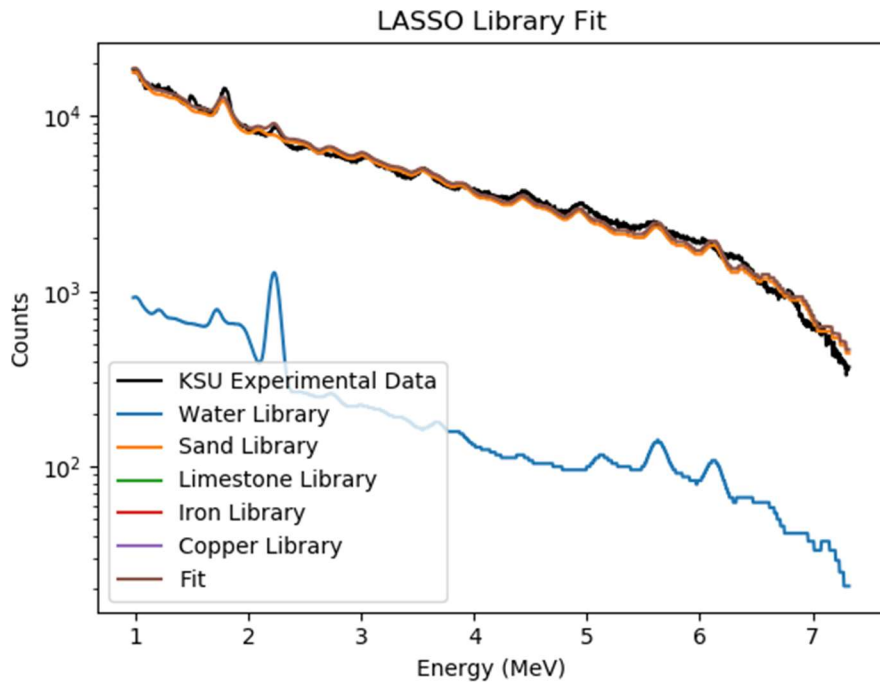


Figure 4-34: LASSO fit for the near detector sand trial

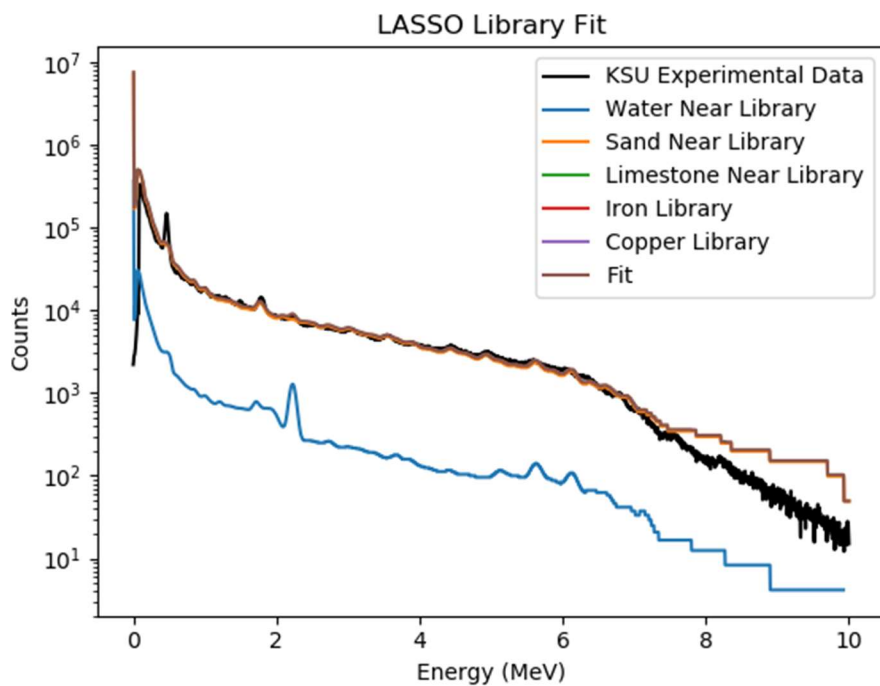


Figure 4-35: LASSO full fit for the near detector sand trial

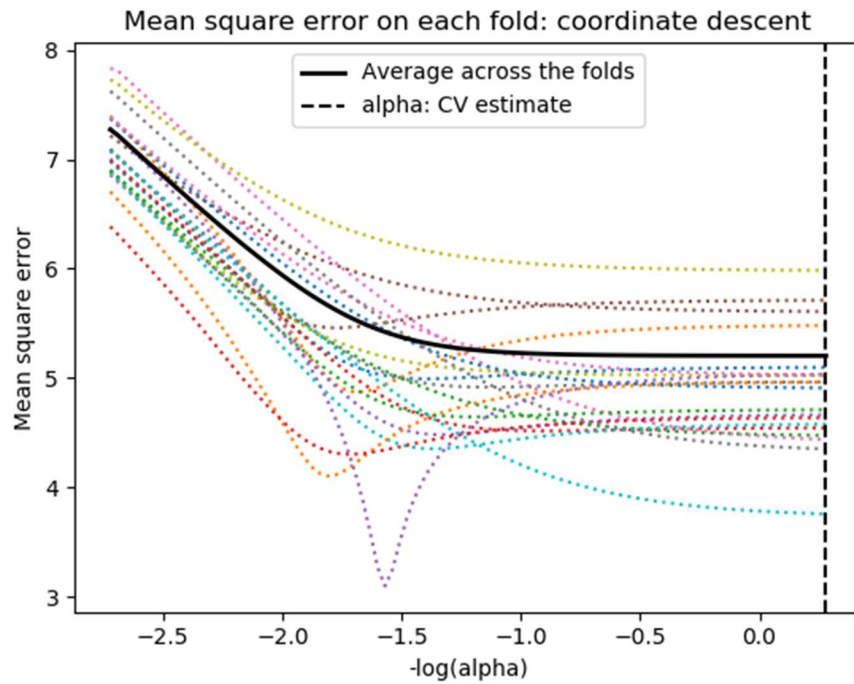


Figure 4-36: Cross validation normalization parameter selection for the Elastic Net near detector sand trial

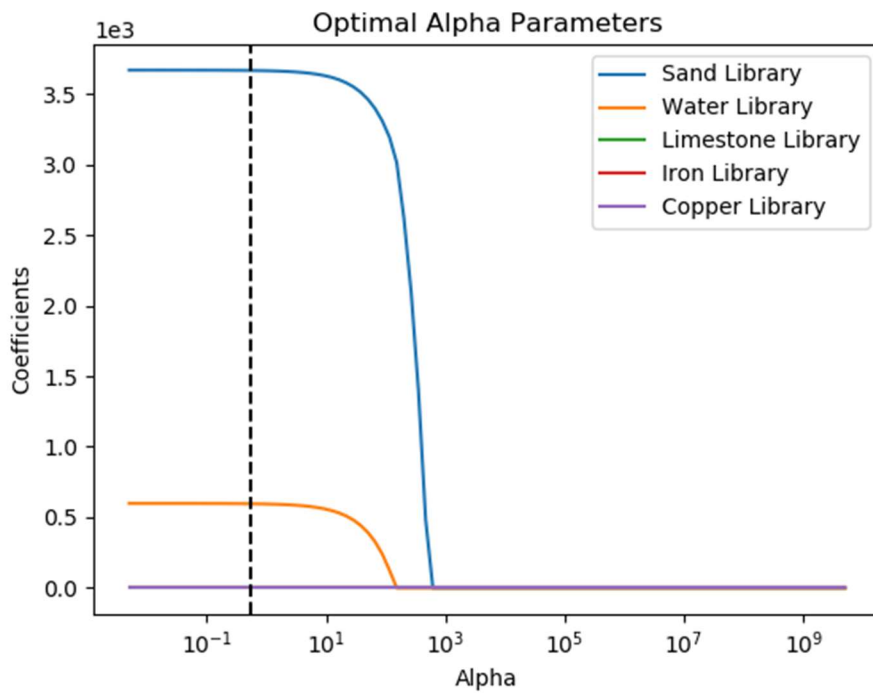


Figure 4-37: Elastic Net model selection coefficients by changing the normalization parameter for the near detector sand trial

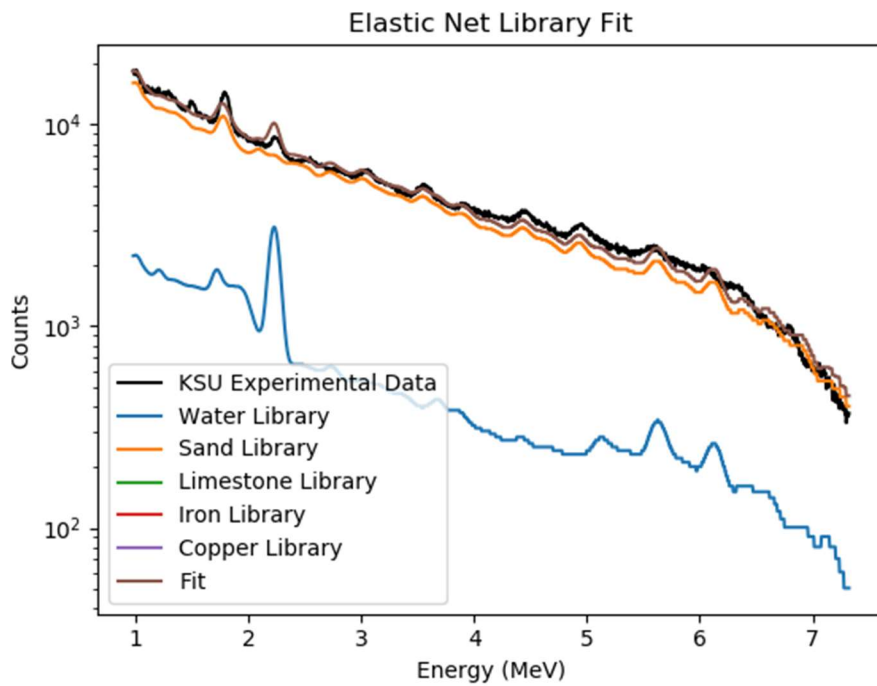


Figure 4-38: Elastic Net fit for the near detector sand trial

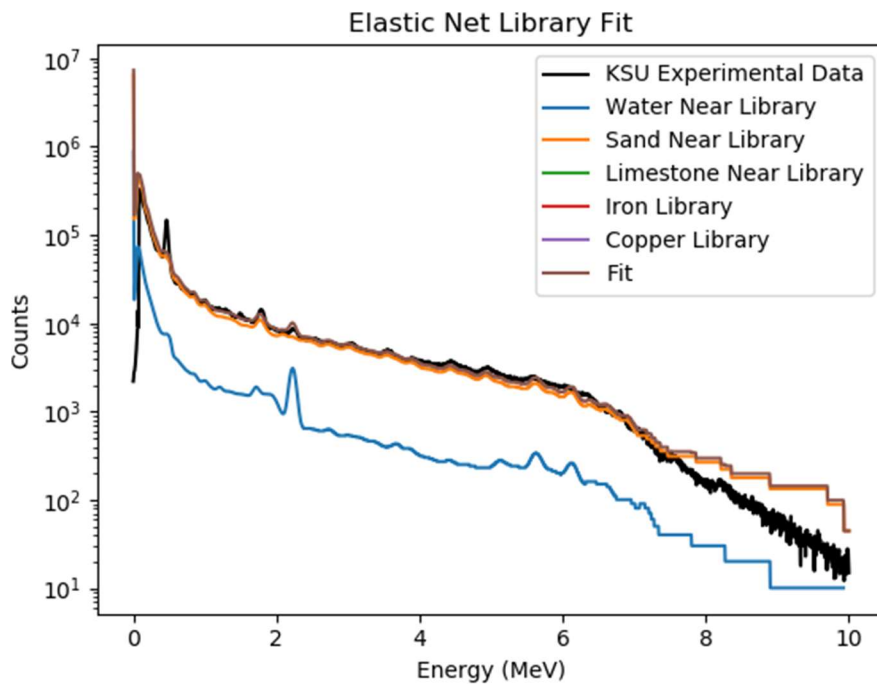


Figure 4-39: Elastic Net full fit for the near detector sand trial

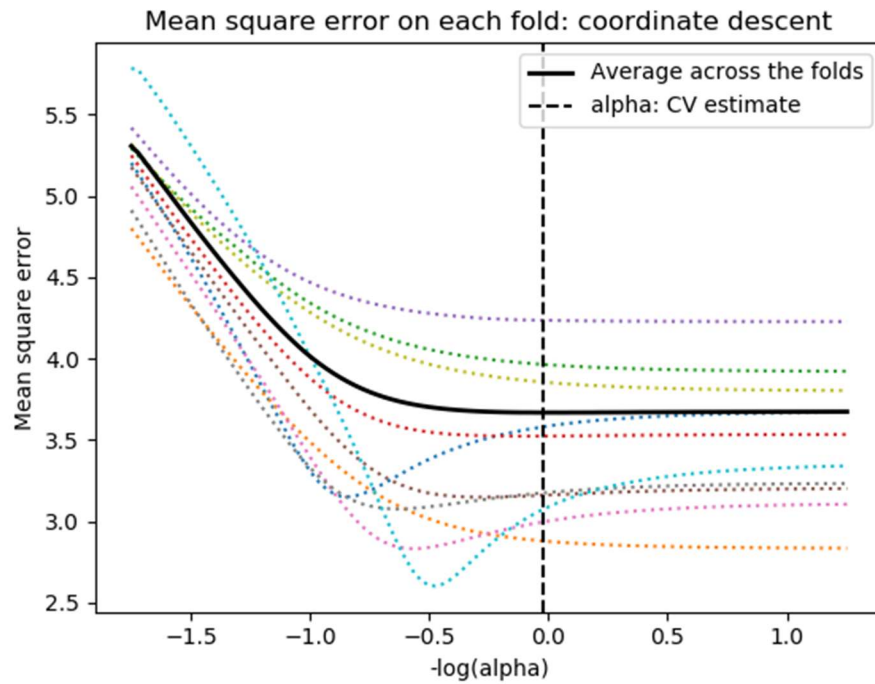


Figure 4-40: Cross validation normalization parameter selection for the LASSO far detector sand trial

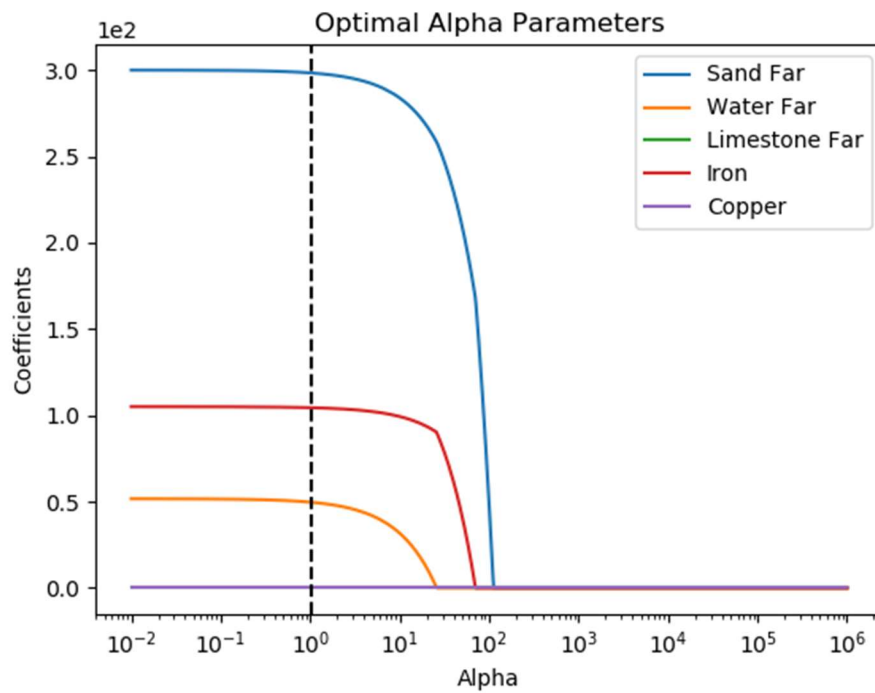


Figure 4-41: LASSO model selection coefficients by changing the normalization parameter for the far detector sand trial

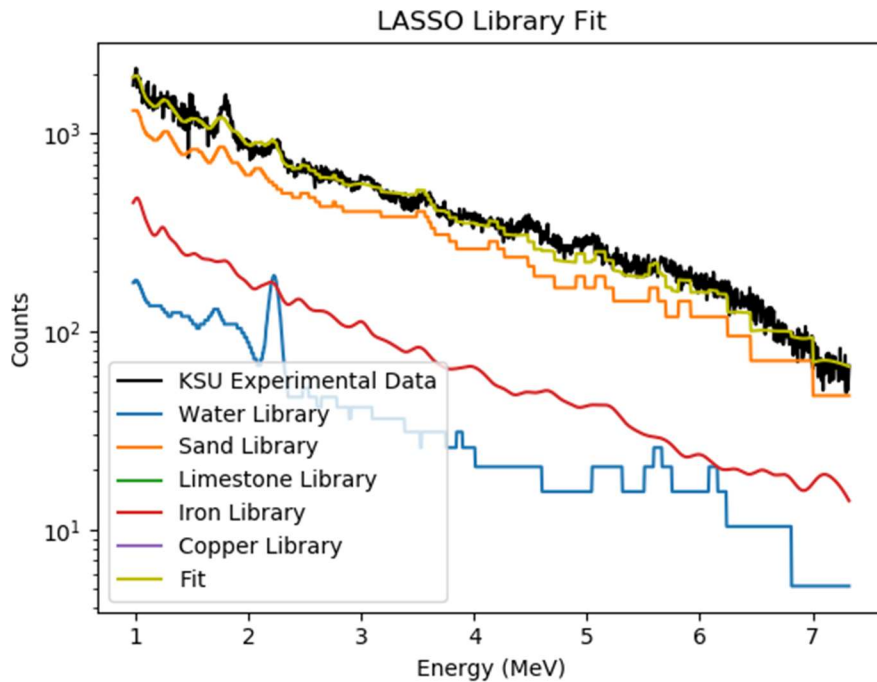


Figure 4-42: LASSO fit for the far detector sand trial

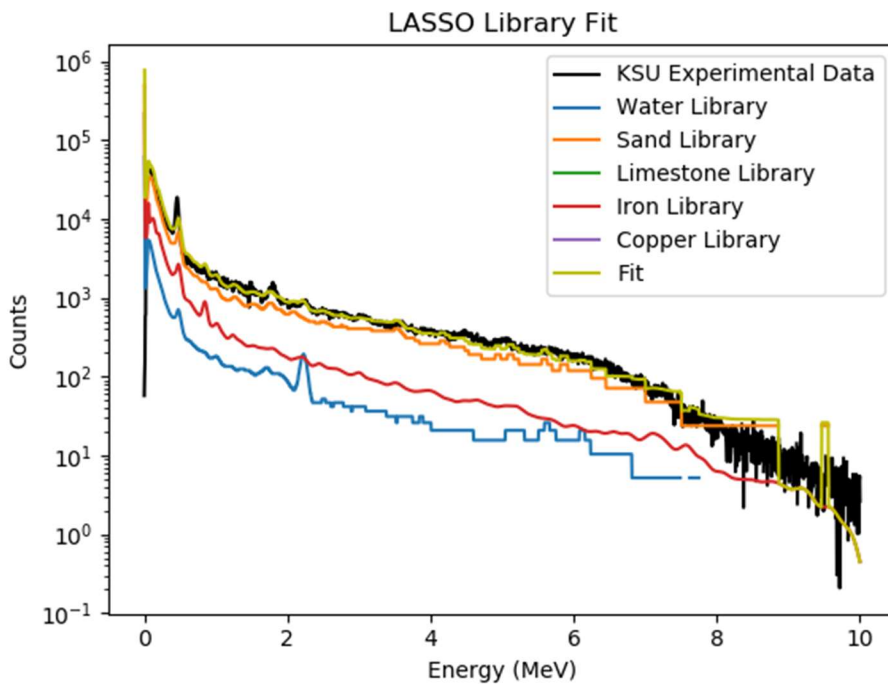


Figure 4-43: LASSO full fit for the far detector sand trial

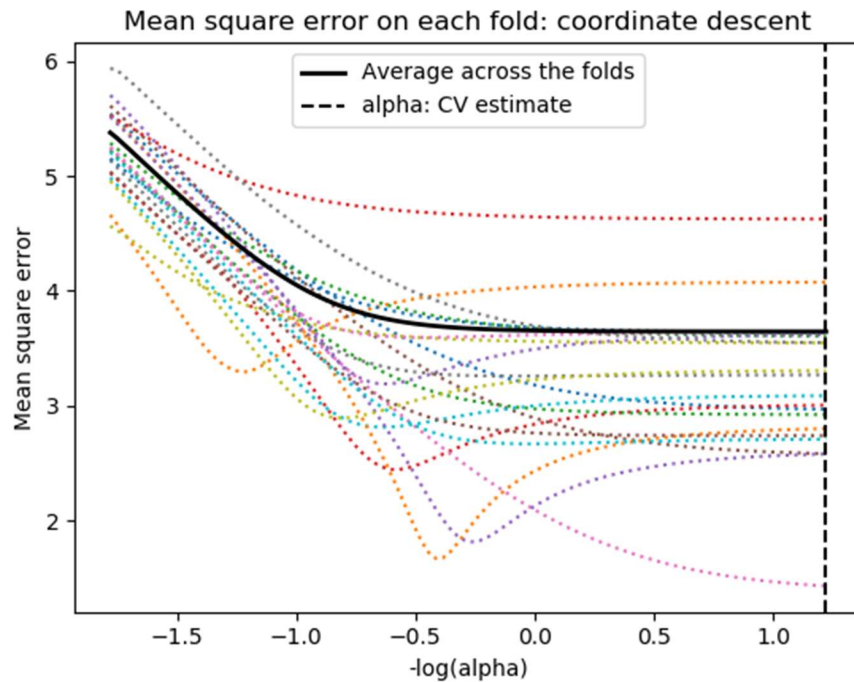


Figure 4-44: Cross validation normalization parameter selection for the Elastic Net far detector sand trial

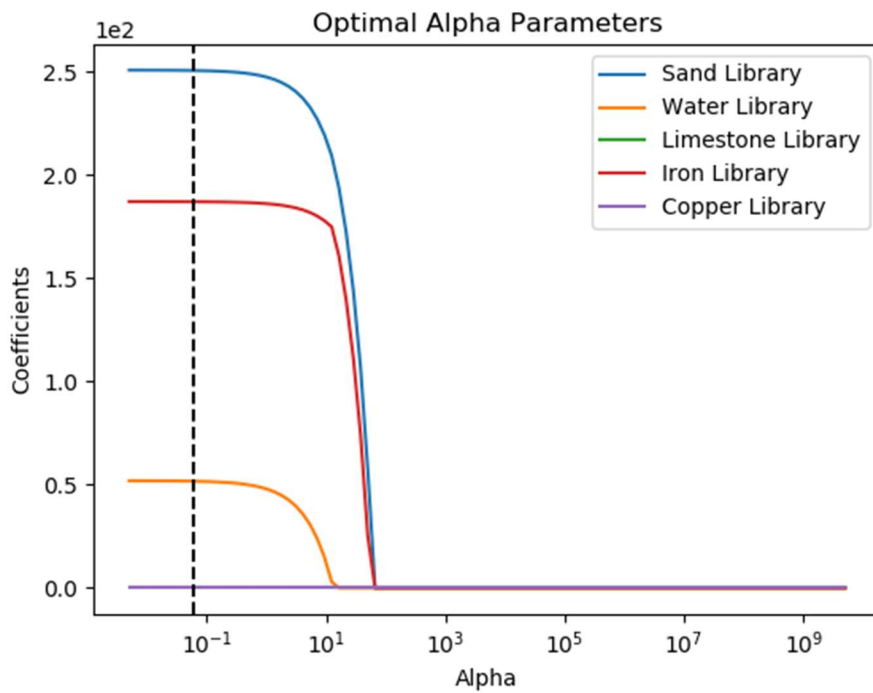


Figure 4-45: Elastic Net model selection coefficients by changing the normalization parameter for the far detector sand trial

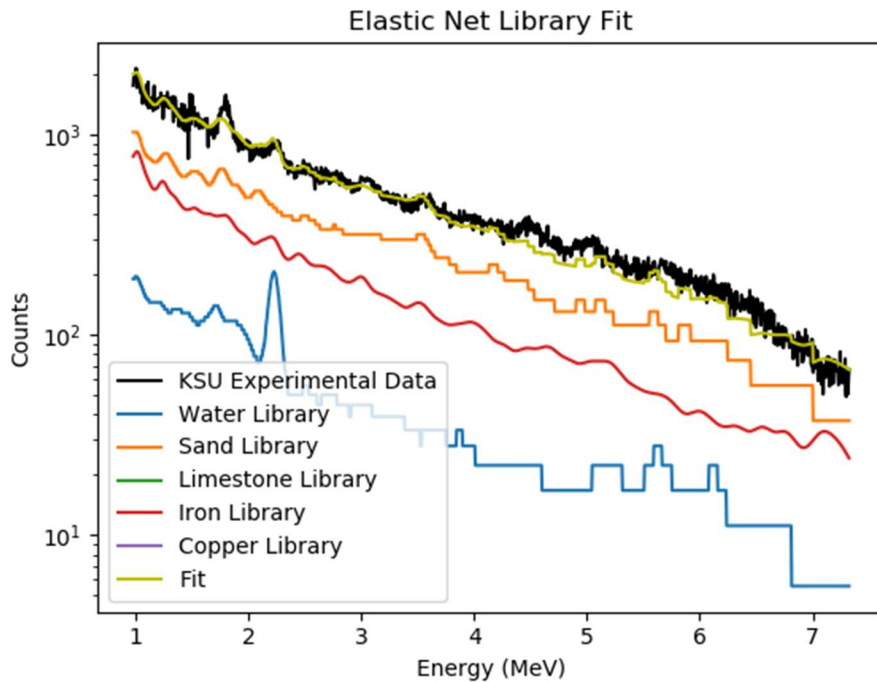


Figure 4-46: Elastic Net fit for the far detector sand trial

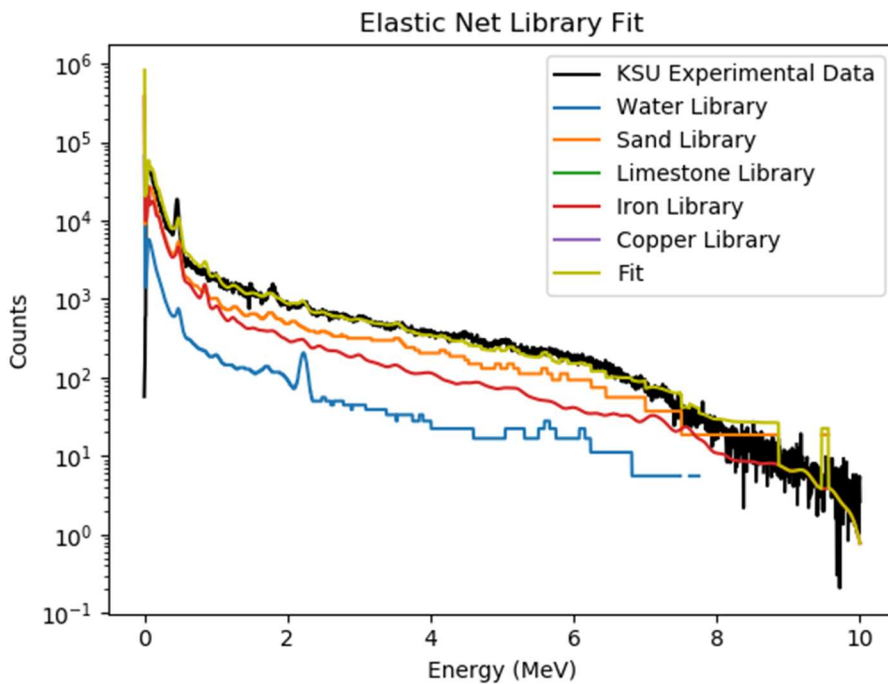


Figure 4-47: Elastic Net full fit for the far detector sand trial

The results show that both LASSO and Elastic Net recognize the presence of both sand and water in the near detector, while also detecting iron in the far detector. The detection of water

was attributed by the Kansas State University researchers as high humidity from running the test in the summer months, as well as not fully evacuating the test chamber of water before the next test. Table 4-5 lists the optimal normalization parameters for each case identified by cross validation. The results for the variable selection process are used as inputs for the final ordinary least squares fitting using the cearlls code. Figures 4-48 and 4-49 display the final fitting and residuals for the near and far detector, respectively. Figure 4-50 shows the near and far final fits together. Tables 4-6, 4-7 provide the chi-squared value, fitting coefficients, and corresponding error.

Table 4-5: Optimal normalization parameters for sand trial

Sand Normalization Parameters		
	Near Detector	Far Detector
LASSO	0.396	1.050
Elastic Net	0.526	0.060

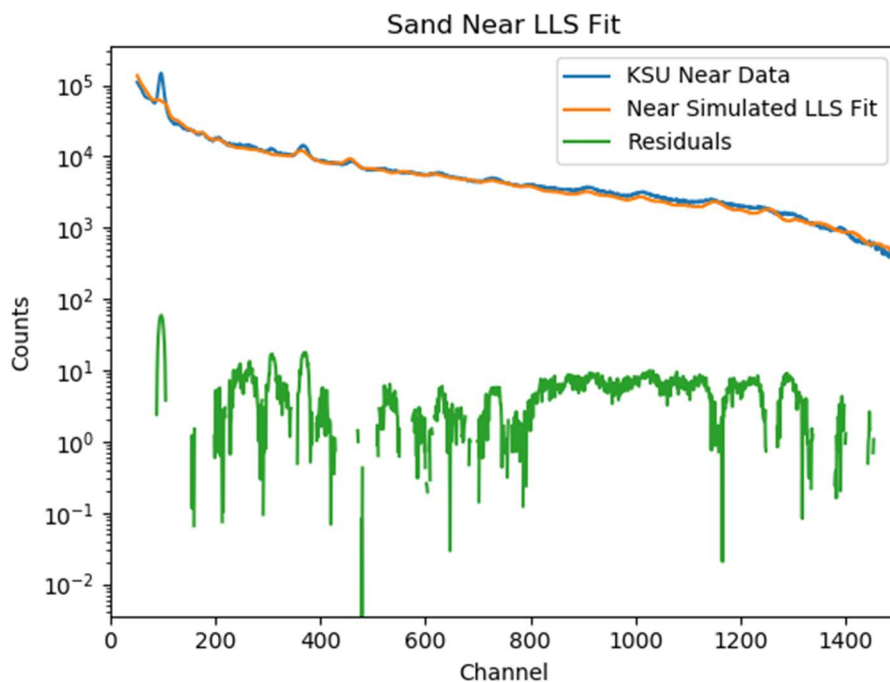


Figure 4-48: Linear least squares fit and residual for the near detector sand trial

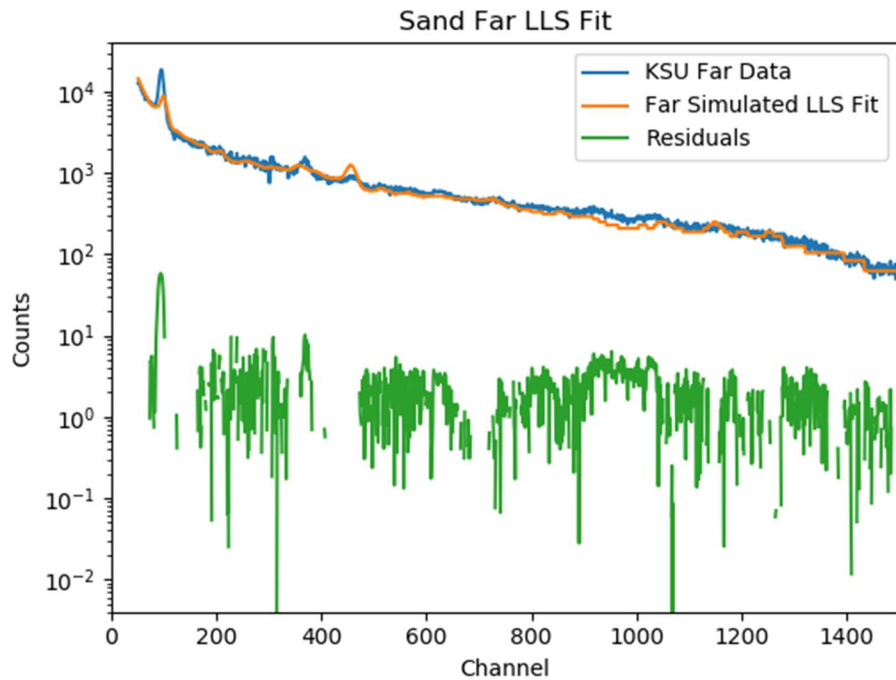


Figure 4-49: Linear least squares fit and residual for the far detector sand trial

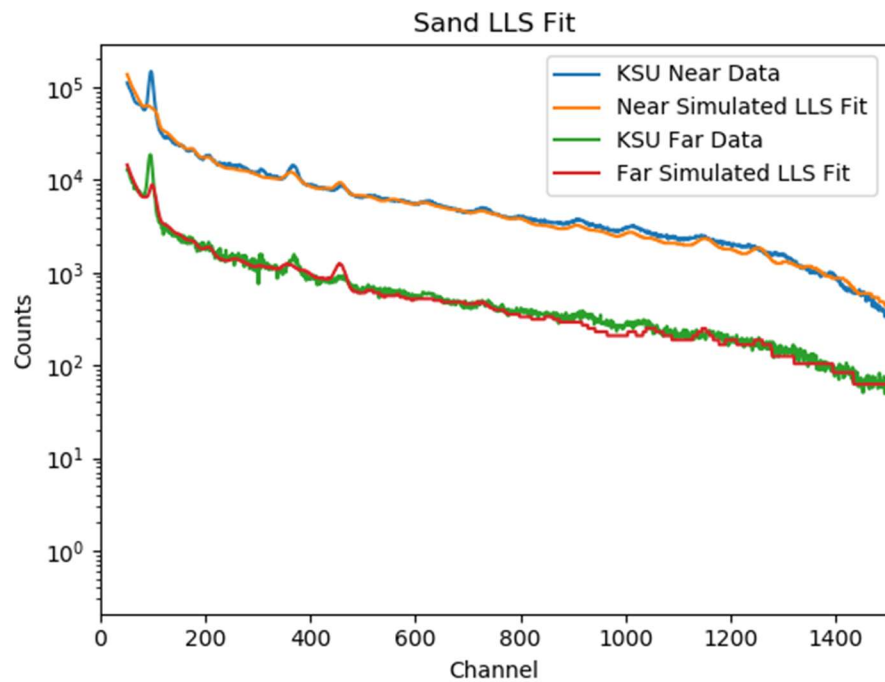


Figure 4-50: Linear least squares fit for near and far detector sand trials

Table 4-6: Linear coefficients and error for sand near detector

Water Linear Least Squares Results – Near Detector		
Chi-Squared = 88.4	Coefficients	Error
Water	79.94	1.10
Sand	437.37	0.13
Limestone	NA	NA
Iron	NA	NA
Copper	NA	NA

Table 4-7: Linear coefficients and error for sand far detector

Water Linear Least Squares Results – Far Detector		
Chi-Squared = 27.6	Coefficients	Error
Water	203.90	0.90
Sand	210.55	0.49
Limestone	NA	NA
Iron	NA	NA
Copper	NA	NA

4.3.3 Sand with Water Trial

The next trial conducted involved sand with added water. No chemical or other analysis was performed on the material, so it is assumed that the makeup is SiO₂. The channel to energy conversion was accomplished by identifying the peak centroids in the sample and adjusting by

$$Energy(MeV) = -0.051 + .00511 * channel + 1e^{-7} * channel^2 \quad (4.5)$$

All other parameters and order of figures are consistent with those from section 4.3.1.

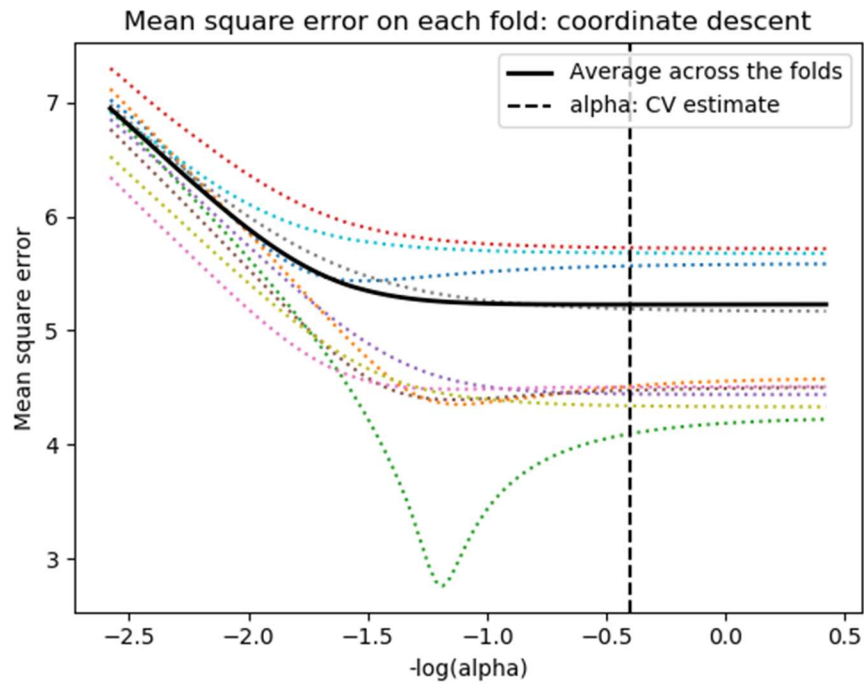


Figure 4-51: Cross validation normalization parameter selection for the LASSO near detector sand and water trial

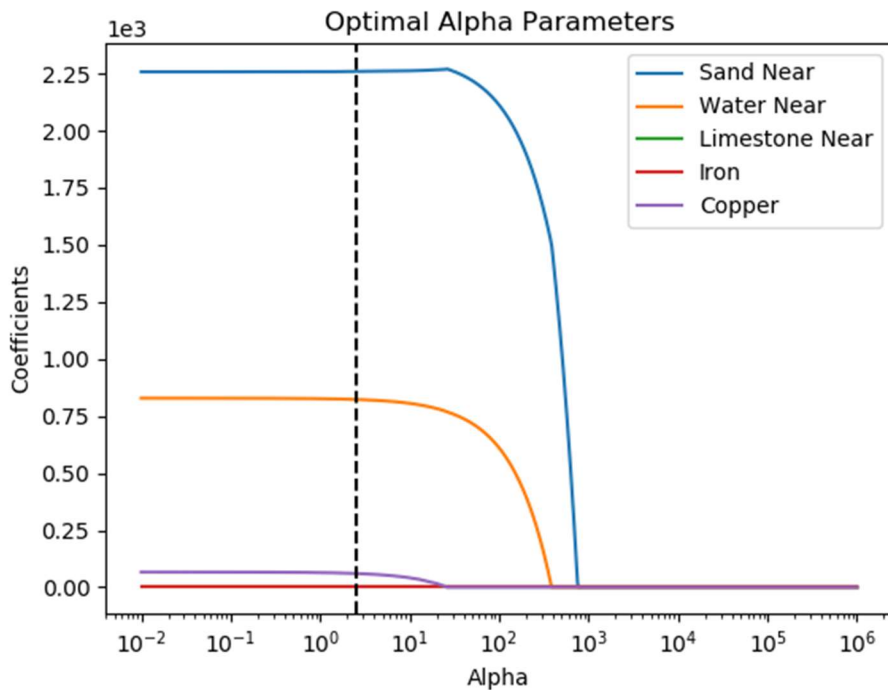


Figure 4-52: LASSO model selection coefficients by changing the normalization parameter for the near detector sand and water trial

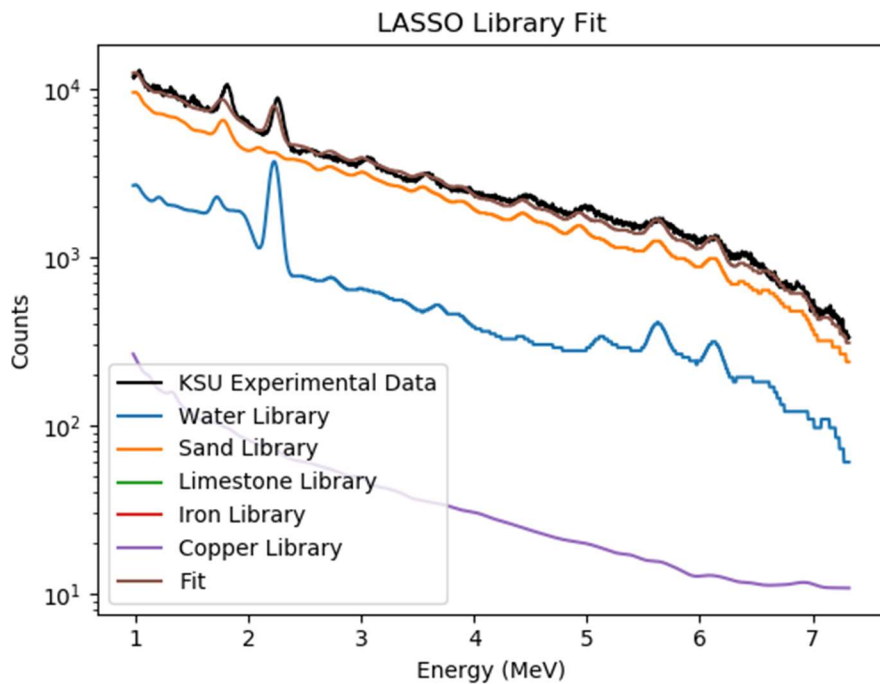


Figure 4-53: LASSO fit for the near detector sand and water trial

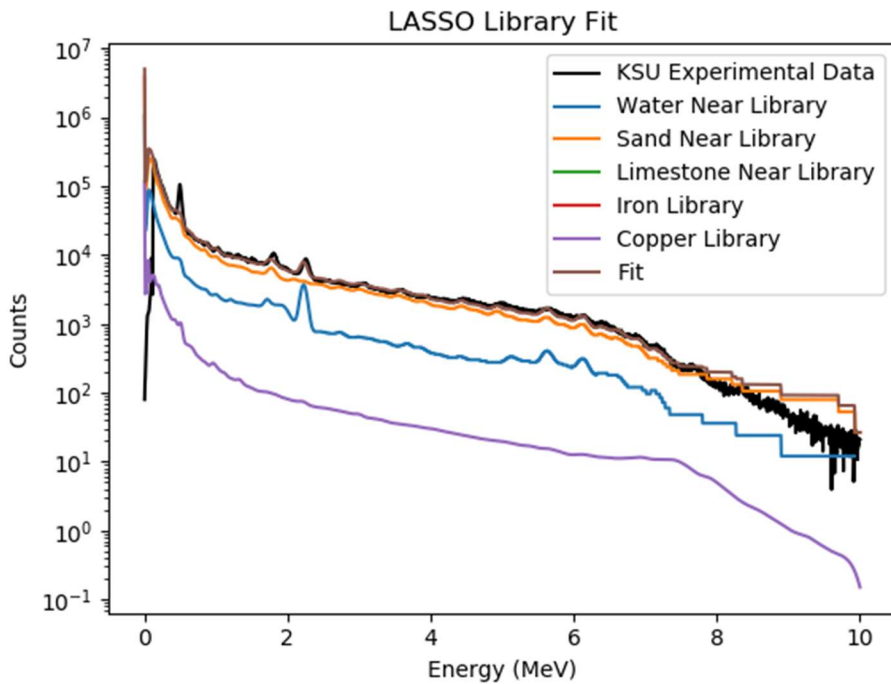


Figure 4-54: LASSO full fit for the near detector sand and water trial

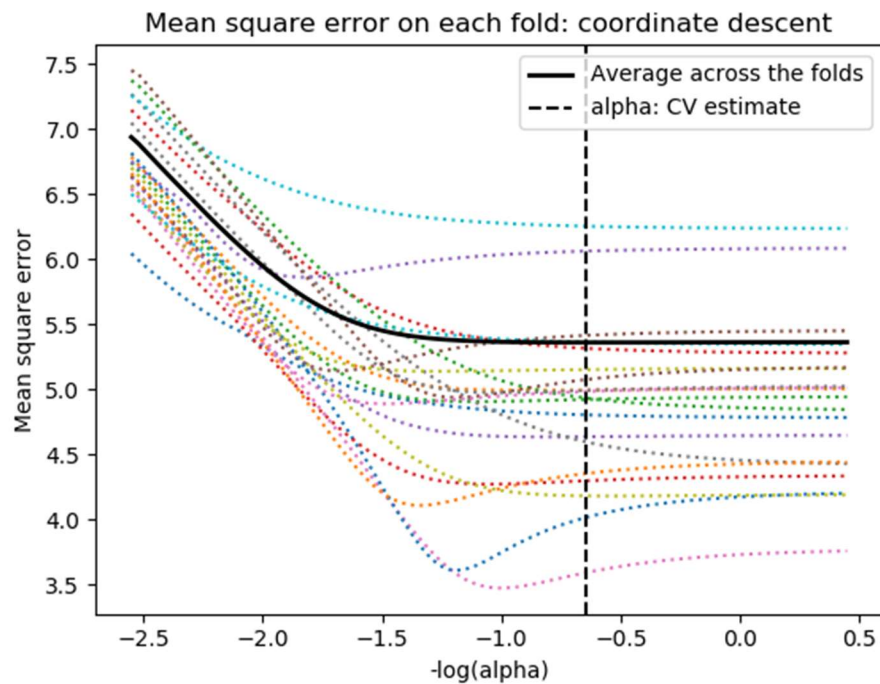


Figure 4-55: Cross validation normalization parameter selection for the Elastic Net near detector sand and water trial

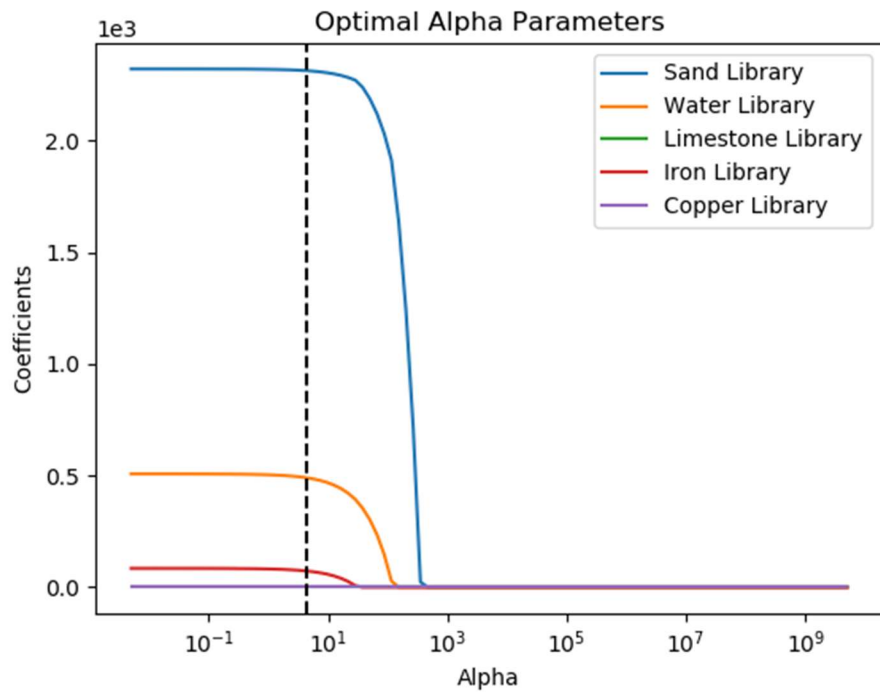


Figure 4-56: Elastic Net model selection coefficients by changing the normalization parameter for the near detector sand and trial

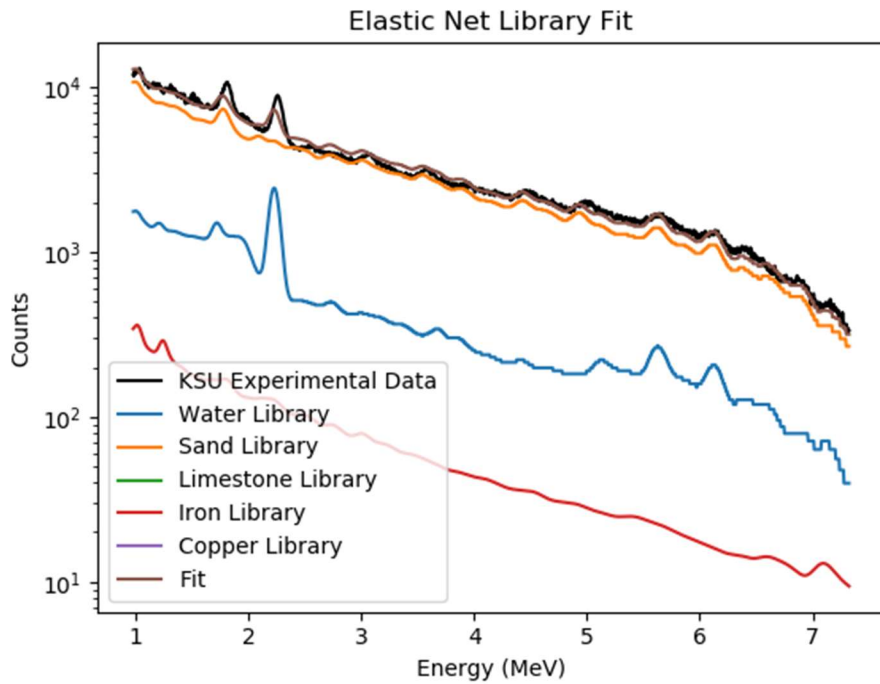


Figure 4-57: Elastic Net fit for the near detector sand and water trial

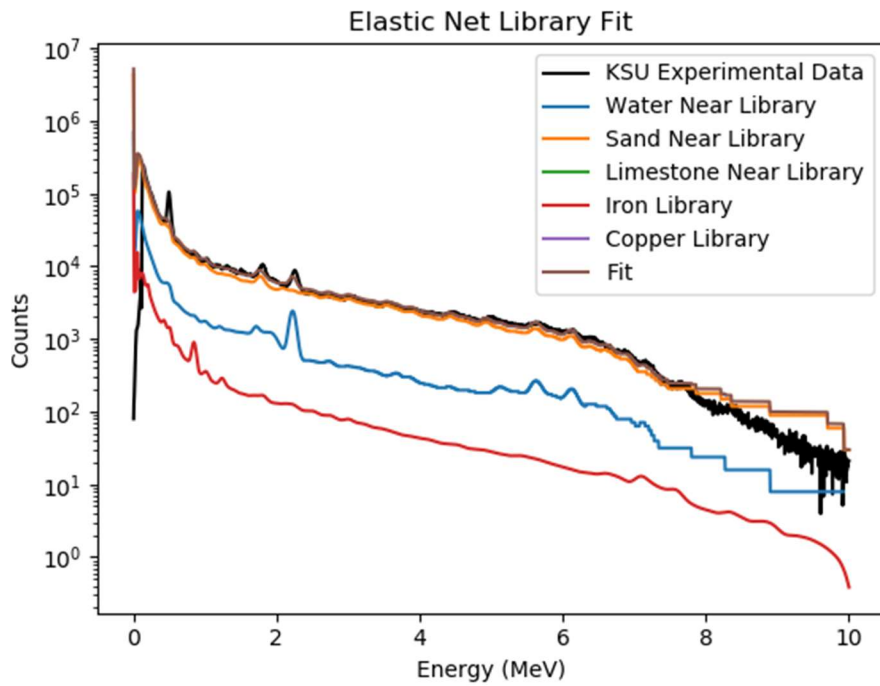


Figure 4-58: Elastic Net full fit for the near detector sand and water trial

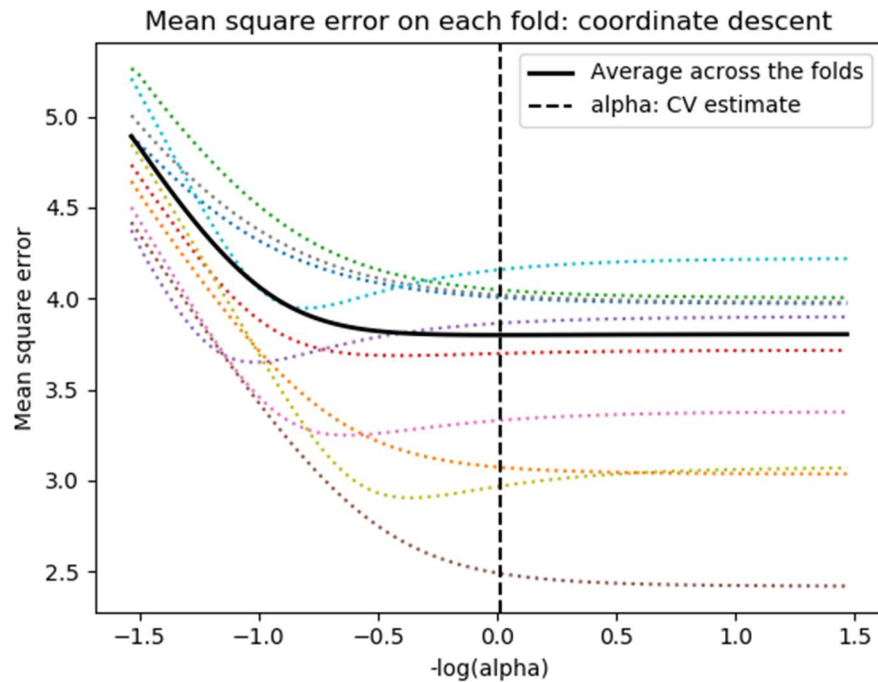


Figure 4-59: Cross validation normalization parameter selection for the LASSO far detector sand and water trial

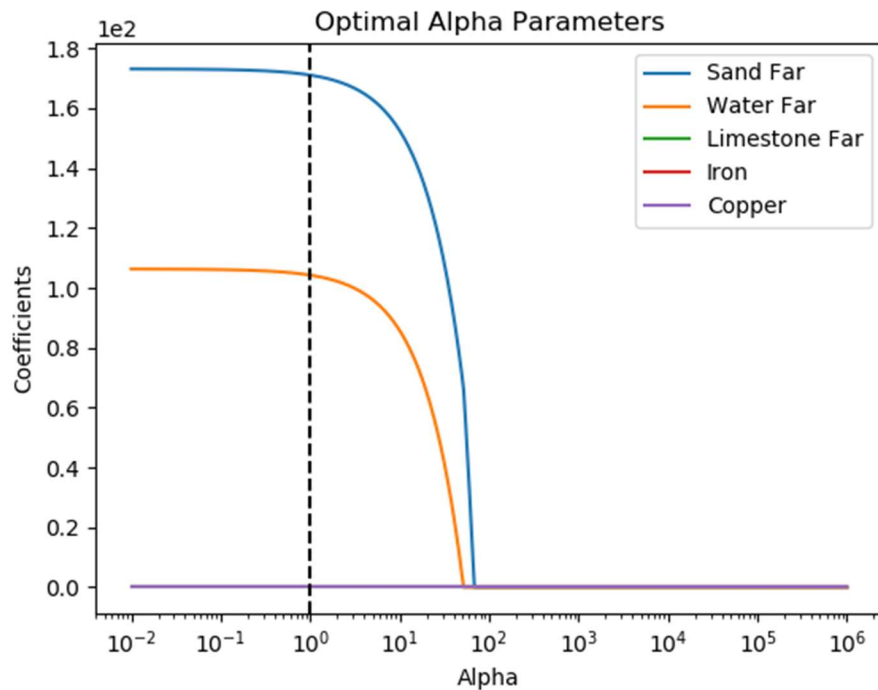


Figure 4-60: LASSO model selection coefficients by changing the normalization parameter for the far detector sand and water trial

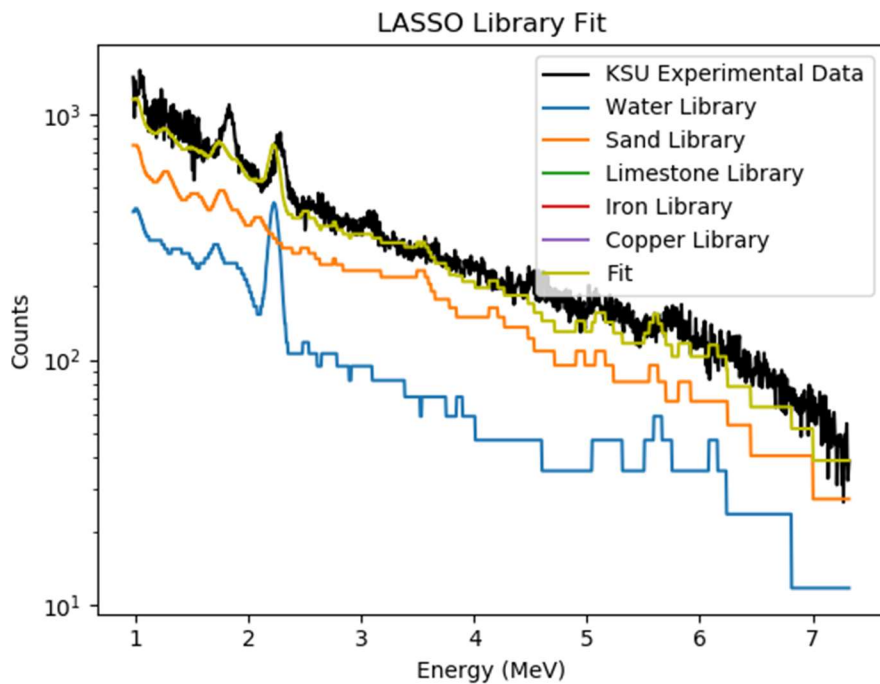


Figure 4-61: LASSO fit for the far detector sand and water trial

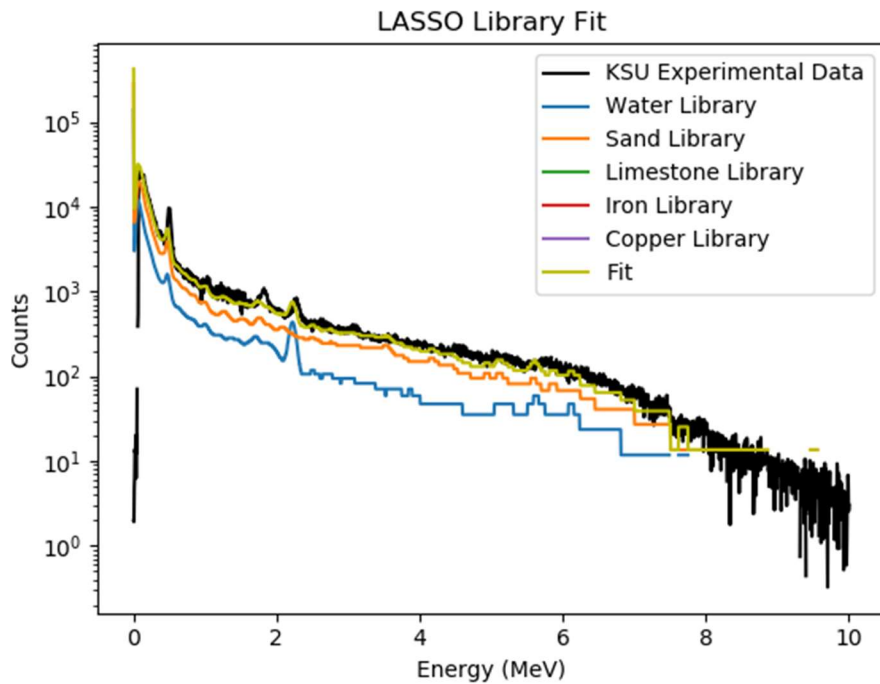


Figure 4-62: LASSO full fit for the far detector sand and water trial

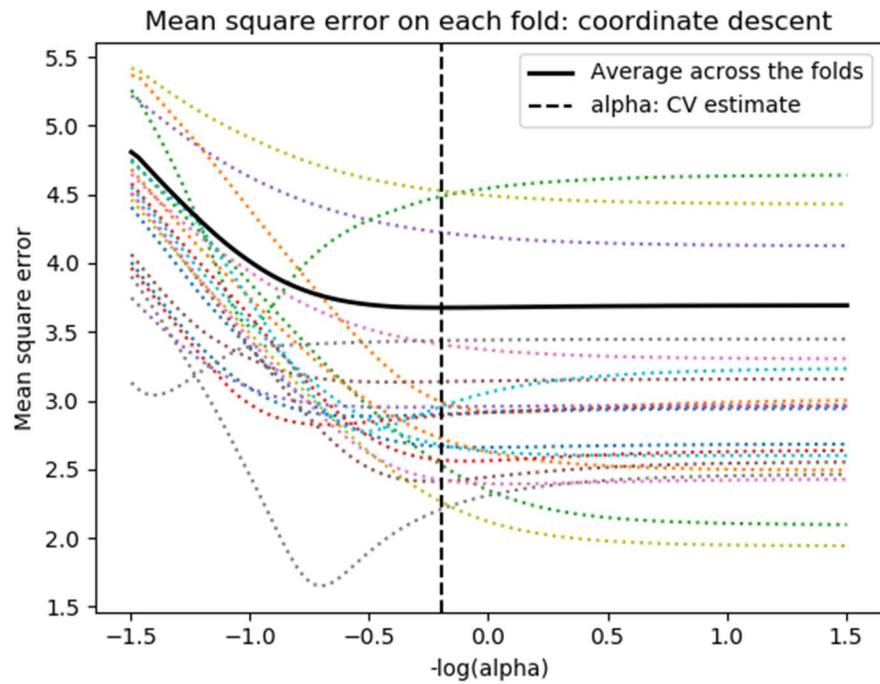


Figure 4-63: Cross validation normalization parameter selection for the Elastic Net far detector sand and water trial

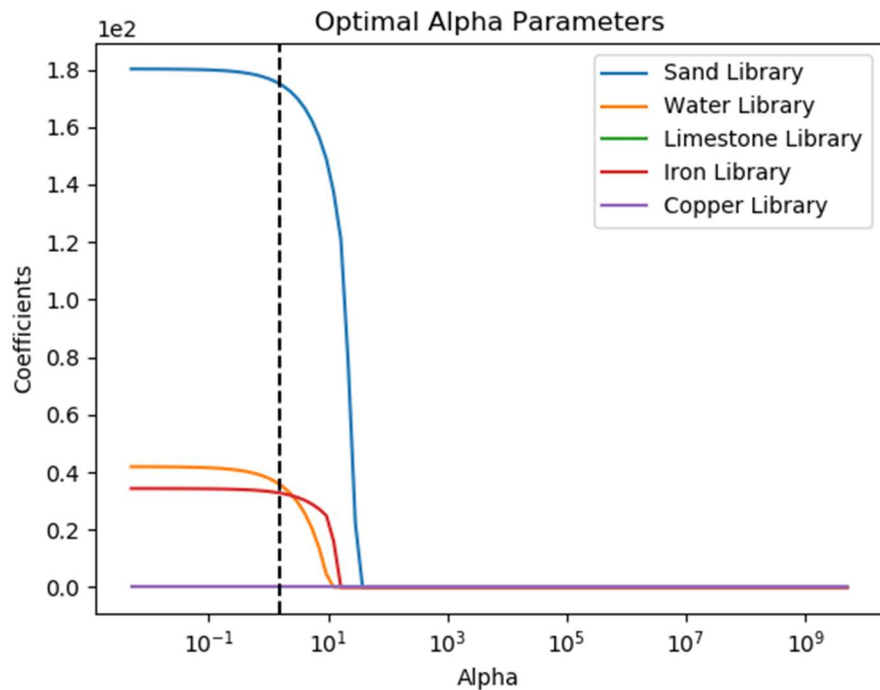


Figure 4-64: Elastic Net model selection coefficients by changing the normalization parameter for the far detector sand and water trial

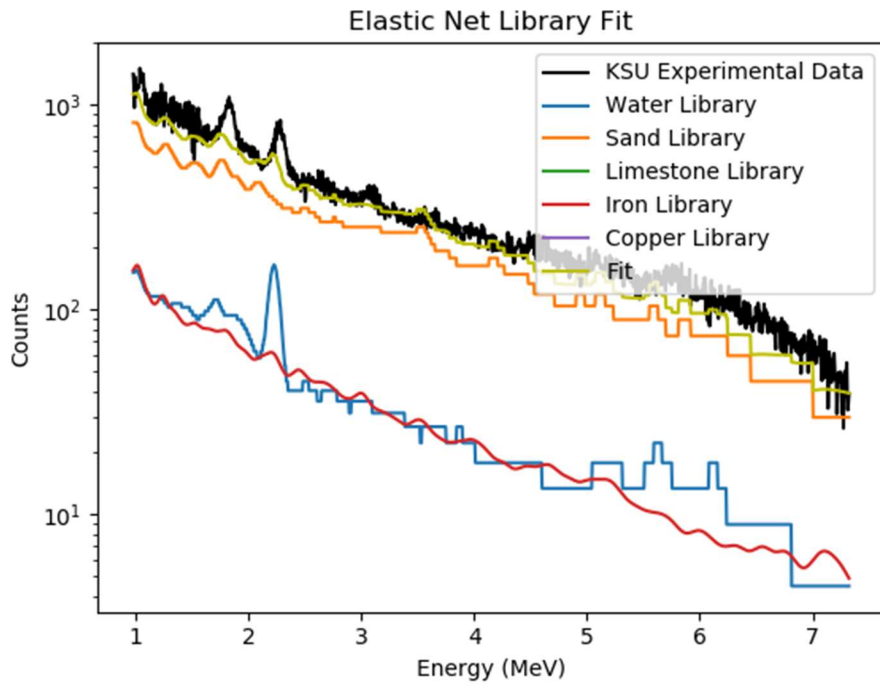


Figure 4-65: Elastic Net fit for the far detector sand and water trial

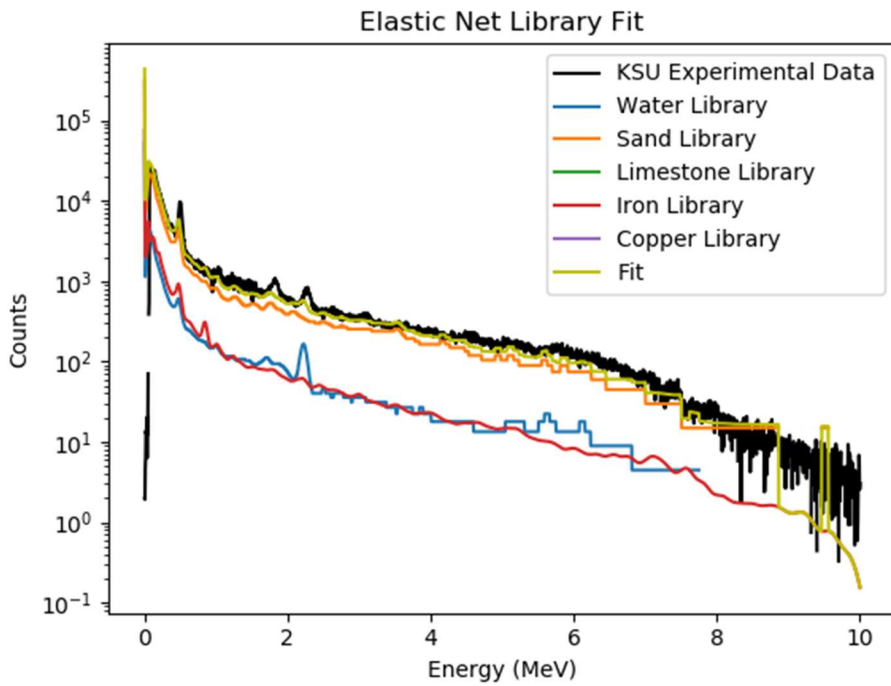


Figure 4-66: Elastic Net full fit for the far detector sand and water trial

The results show that both LASSO and Elastic Net recognize the presence of both sand and water in the near and far detectors. 3 of the 4 tests also include small amounts of iron or copper. Table 4-8 lists the optimal normalization parameters for each case identified by cross validation. The results for the variable selection process are used as inputs for the final ordinary least squares fitting using the cearlls code. Figures 4-67 and 4-68 display the final fitting and residuals for the near and far detector, respectively. Figure 4-69 shows the near and far final fits together. Tables 4-9, 4-10 provide the chi-squared value, fitting coefficients, and corresponding error.

Table 4-8: Optimal normalization parameters for sand and water trial

Sand and Water Normalization Parameters		
	Near Detector	Far Detector
LASSO	2.495	0.972
Elastic Net	4.385	1.561

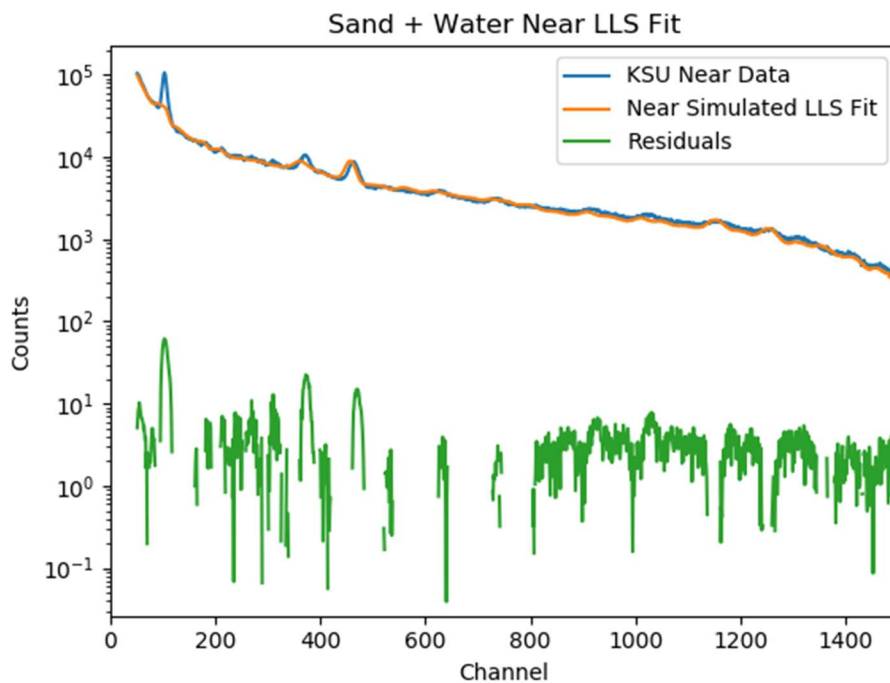


Figure 4-67: Linear least squares fit and residual for the near detector sand and water trial

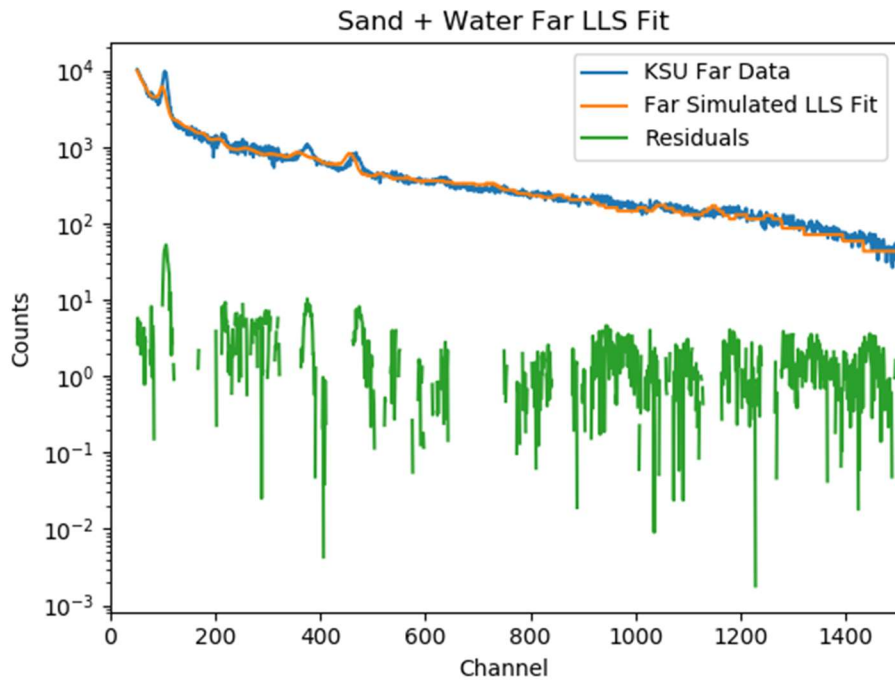


Figure 4-68: Linear least squares fit and residual for the far detector sand and water trial

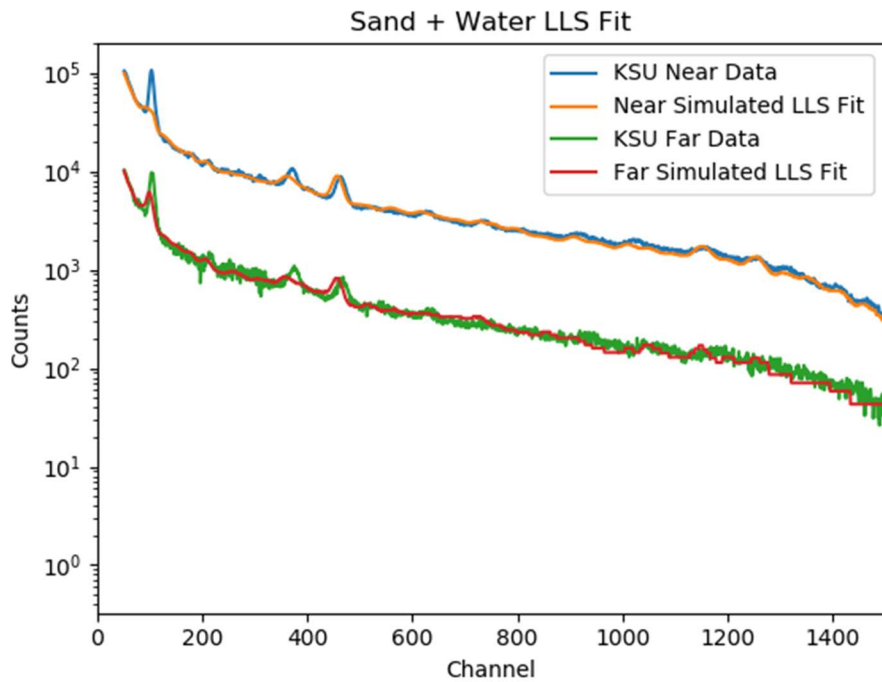


Figure 4-69: Linear least squares fit for near and far detector sand and water trials

Table 4-9: Linear coefficients and error for sand and water near detector

Sand and Water Linear Least Squares Results – Near Detector		
Chi-Squared = 51.8	Coefficients	Error
Water	164.20	0.48
Sand	247.83	0.20
Limestone	NA	NA
Iron	NA	NA
Copper	NA	NA

Table 4-10: Linear coefficients and error for sand and water far detector

Sand and Water Linear Least Squares Results – Far Detector		
Chi-Squared = 18.2	Coefficients	Error
Water	125.89	1.34
Sand	152.51	0.62
Limestone	NA	NA
Iron	NA	NA
Copper	NA	NA

4.3.4 Limestone Trial

The next trial conducted involved pure limestone. No chemical or other analysis was performed on the material, so it is assumed that the makeup is CaCO₃, SiO₂, and SiO₄. The channel to energy conversion was accomplished by identifying the peak centroids in the sample and adjusting by

$$\text{Energy(MeV)} = -0.012 + .00492 * \text{channel} + 2e^{-7} * \text{channel}^2 \quad (4.6)$$

All other parameters and order of figures are consistent with those from section 4.3.1.

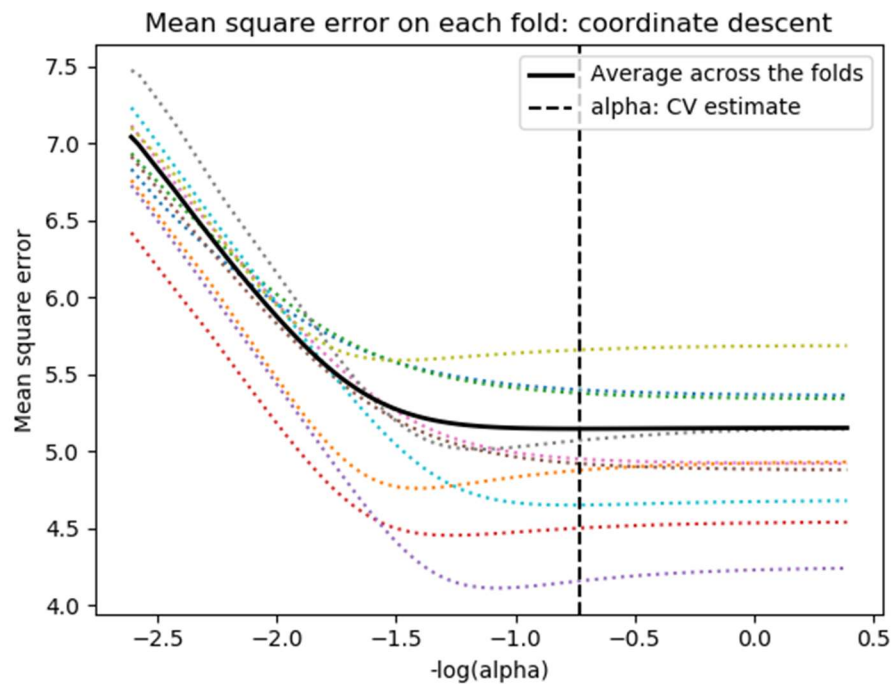


Figure 4-70: Cross validation normalization parameter selection for the LASSO near detector limestone trial

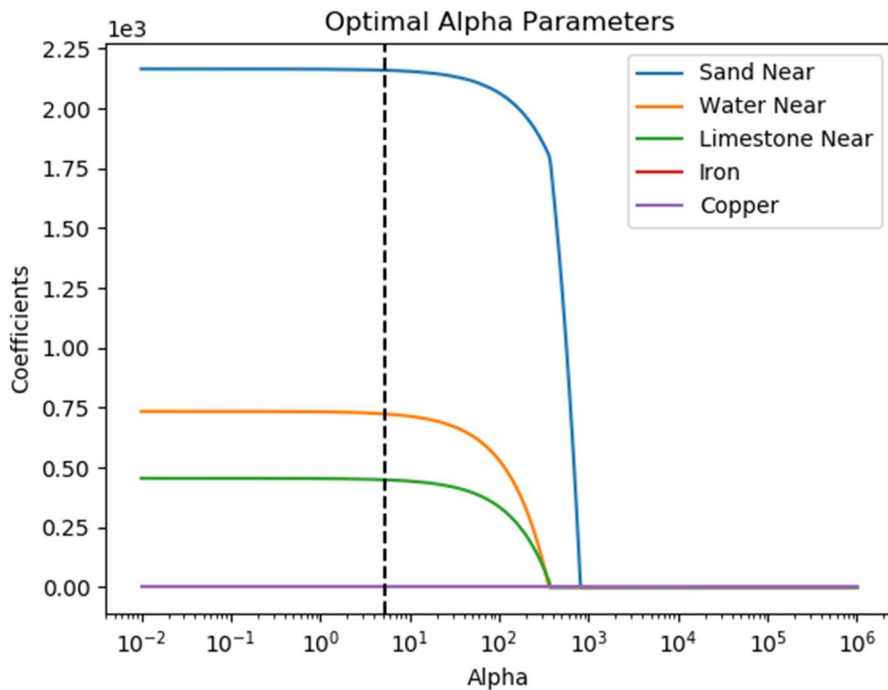


Figure 4-71: LASSO model selection coefficients by changing the normalization parameter for the near detector limestone trial

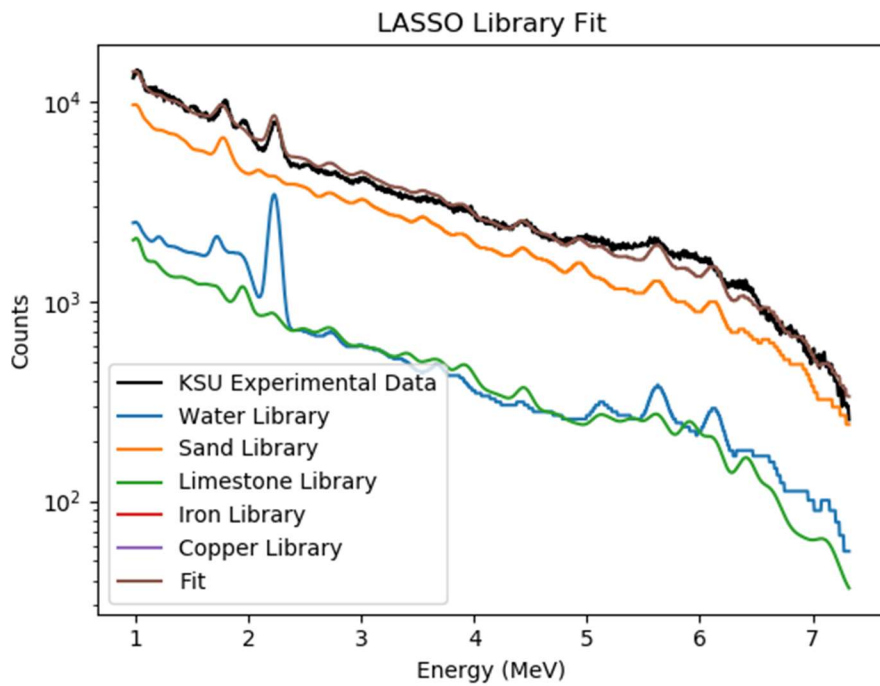


Figure 4-72: LASSO fit for the near detector limestone trial

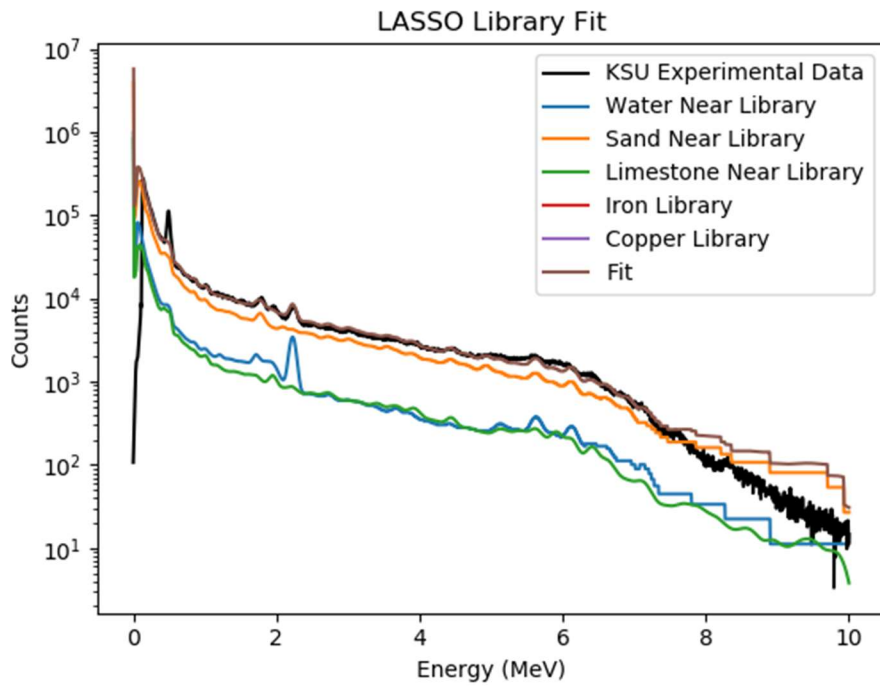


Figure 4-73: LASSO full fit for the near detector limestone trial

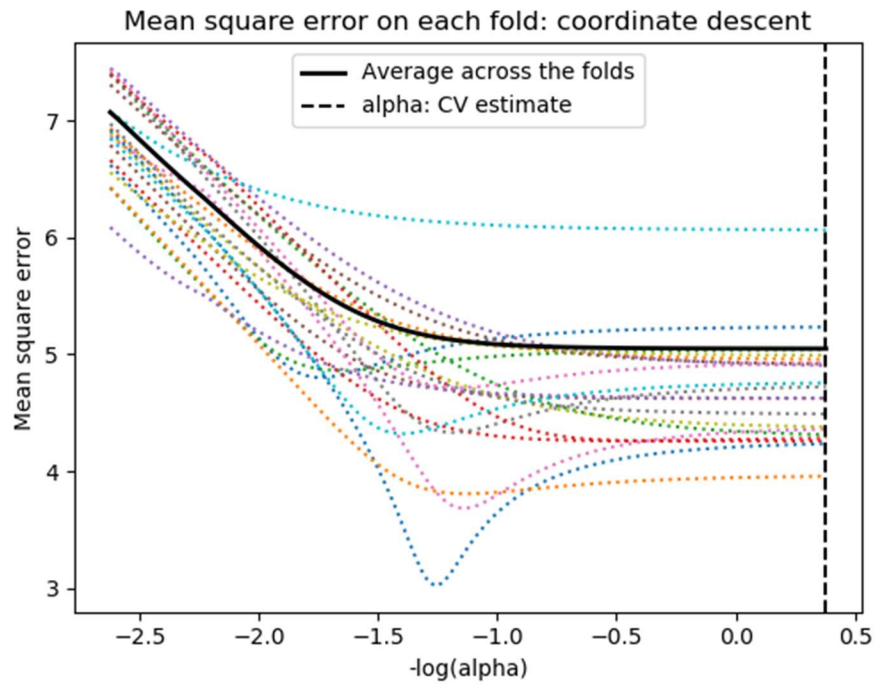


Figure 4-74: Cross validation normalization parameter selection for the Elastic Net near detector limestone trial

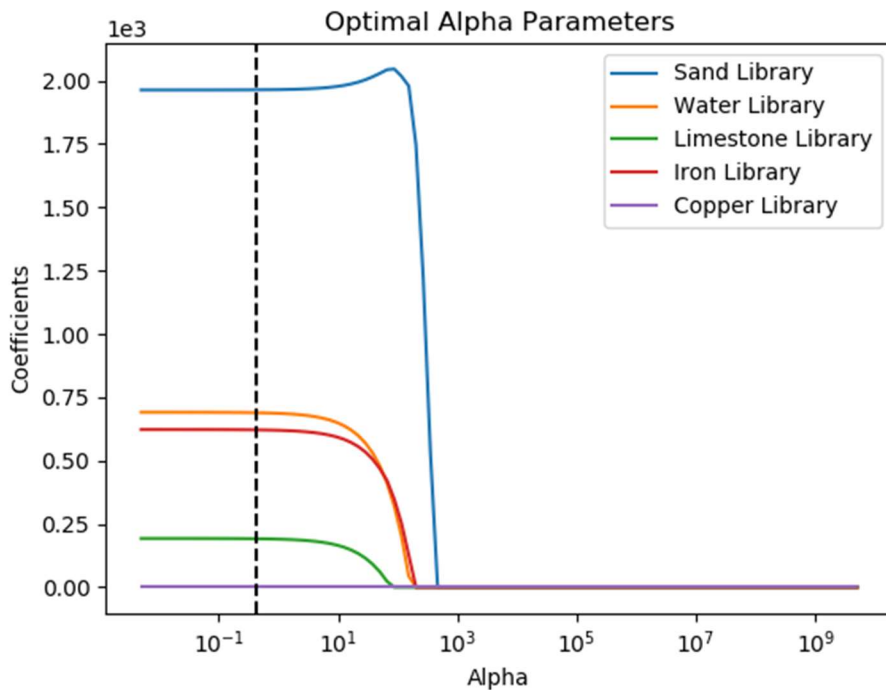


Figure 4-75: Elastic Net model selection coefficients by changing the normalization parameter for the near detector limestone trial

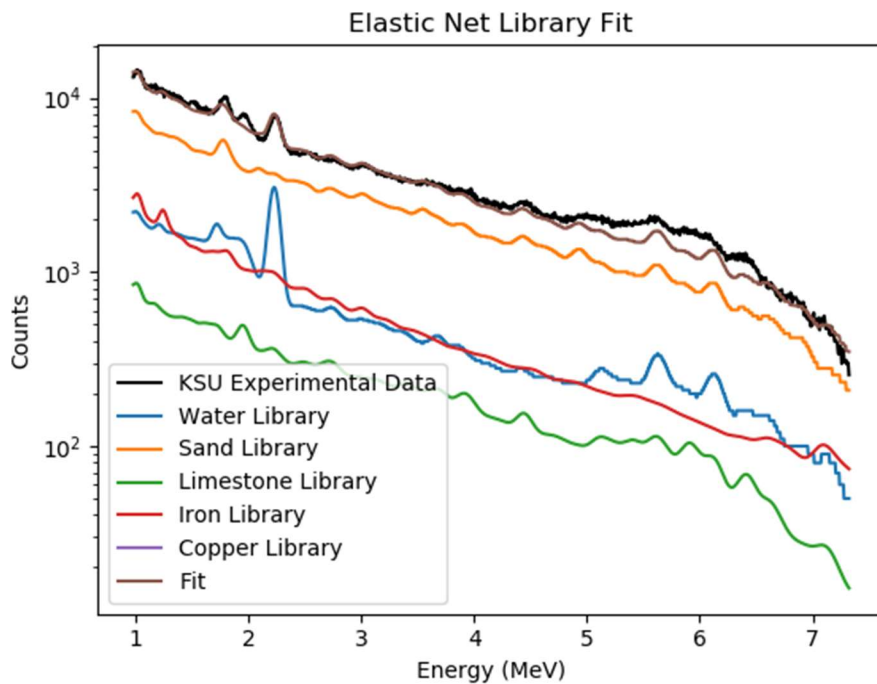


Figure 4-76: Elastic Net fit for the near detector limestone trial

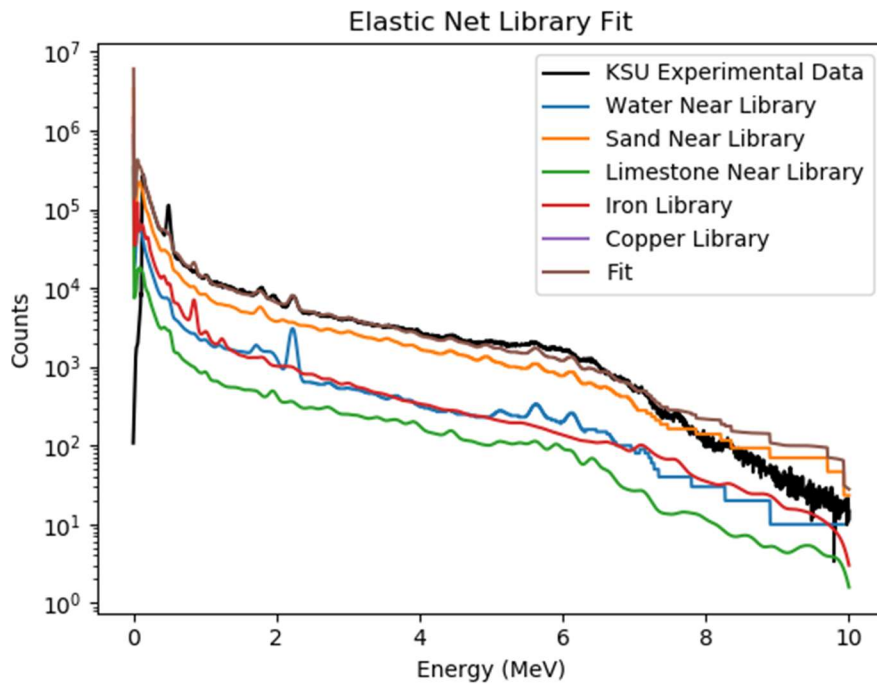


Figure 4-77: Elastic Net full fit for the near detector limestone trial

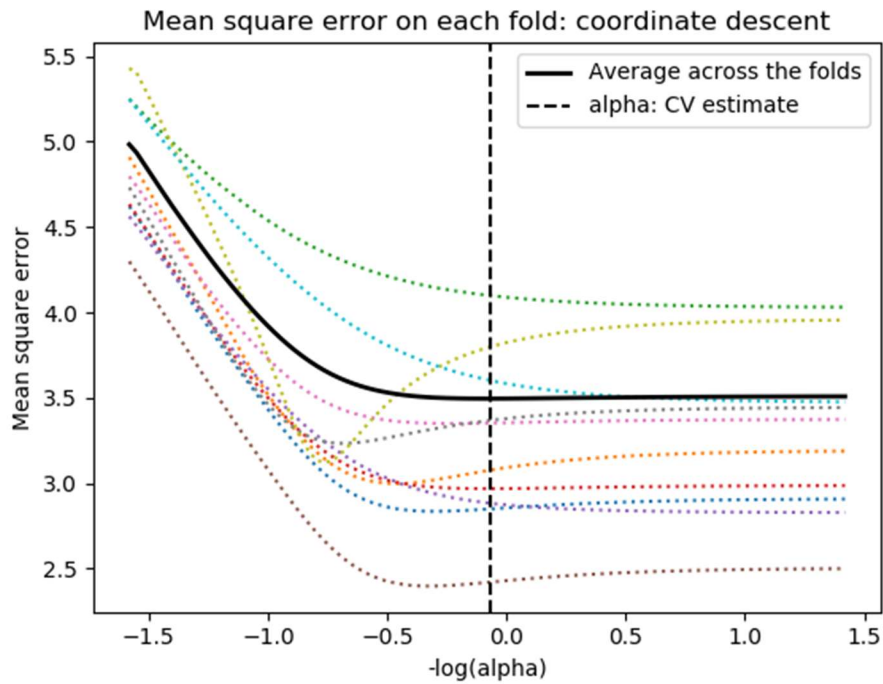


Figure 4-78: Cross validation normalization parameter selection for the LASSO far detector limestone trial

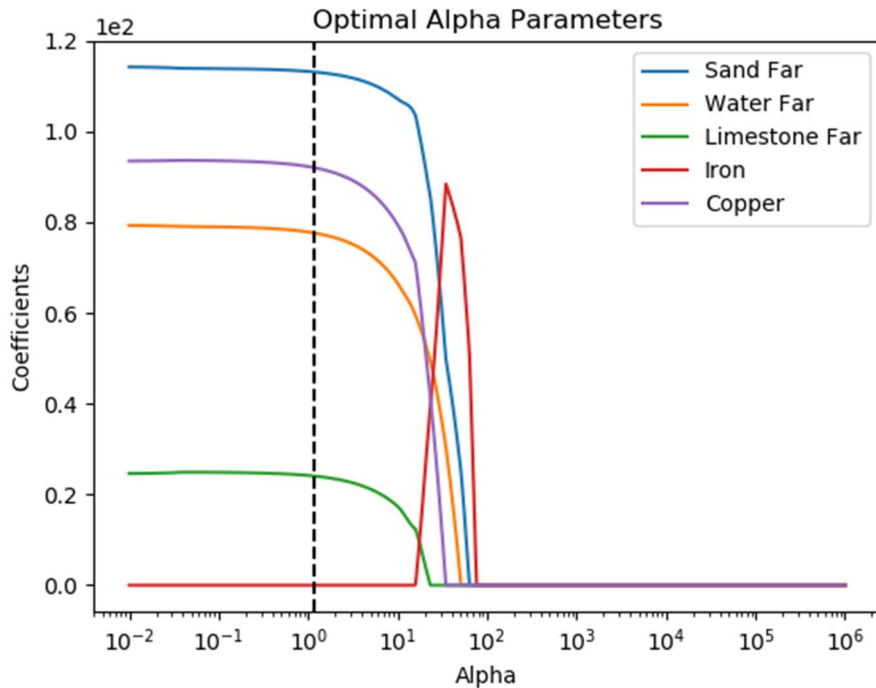


Figure 4-79: LASSO model selection coefficients by changing the normalization parameter for the far detector limestone trial

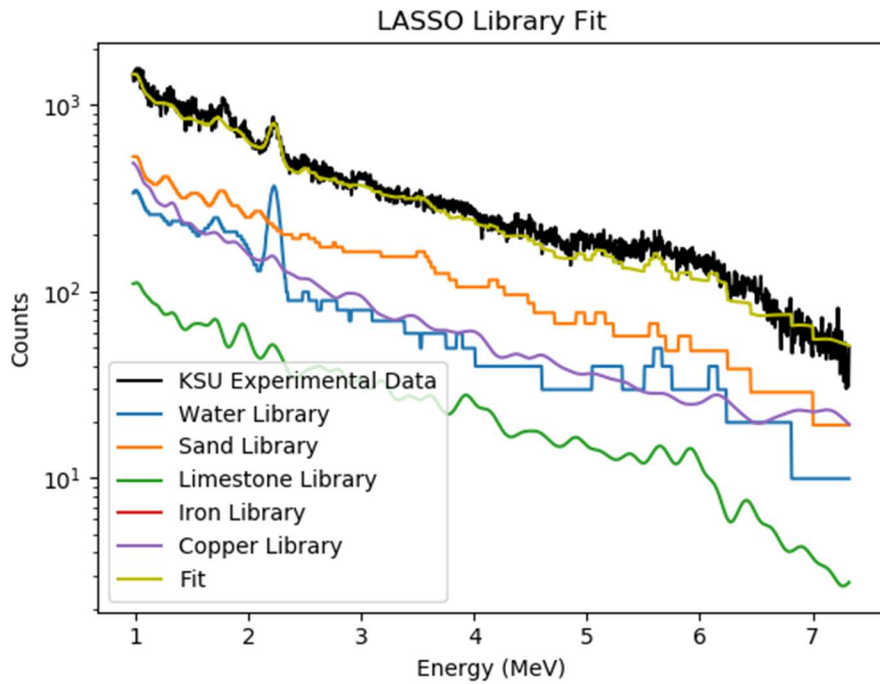


Figure 4-80: LASSO fit for the far detector limestone trial

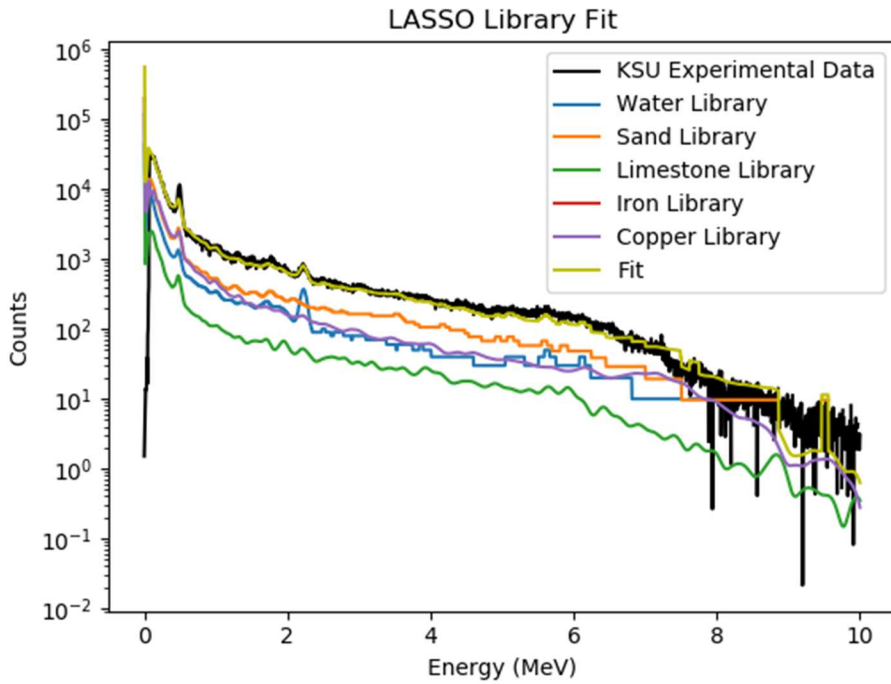


Figure 4-81: LASSO full fit for the far detector limestone trial

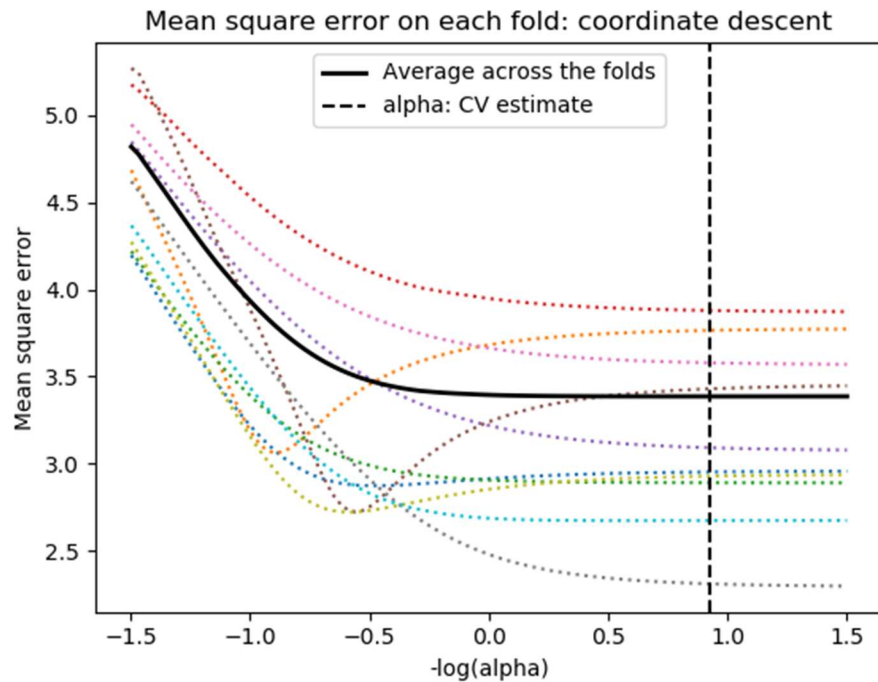


Figure 4-82: Cross validation normalization parameter selection for the Elastic Net far detector limestone trial

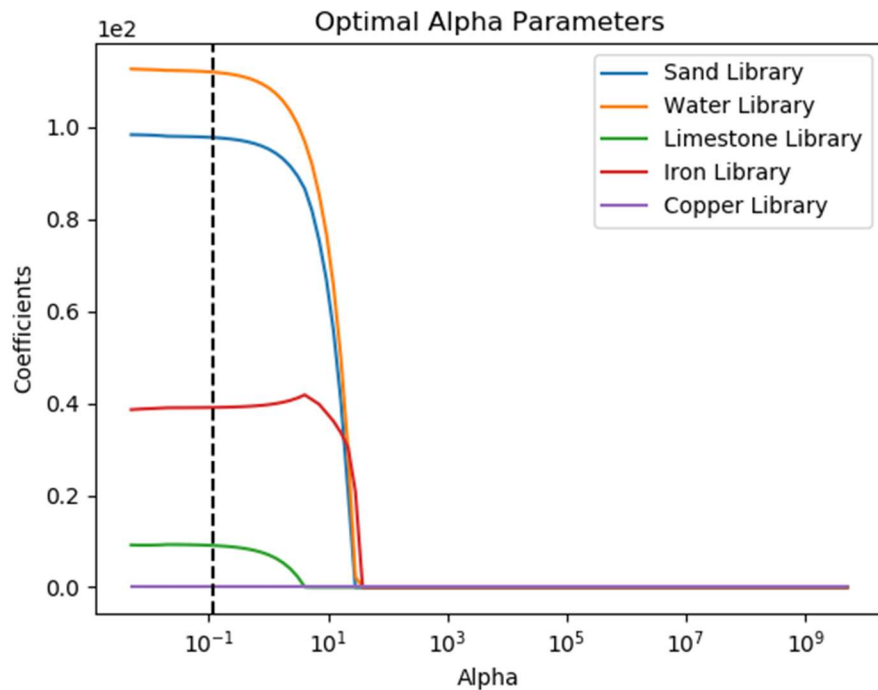


Figure 4-83: Elastic Net model selection coefficients by changing the normalization parameter for the far detector limestone trial

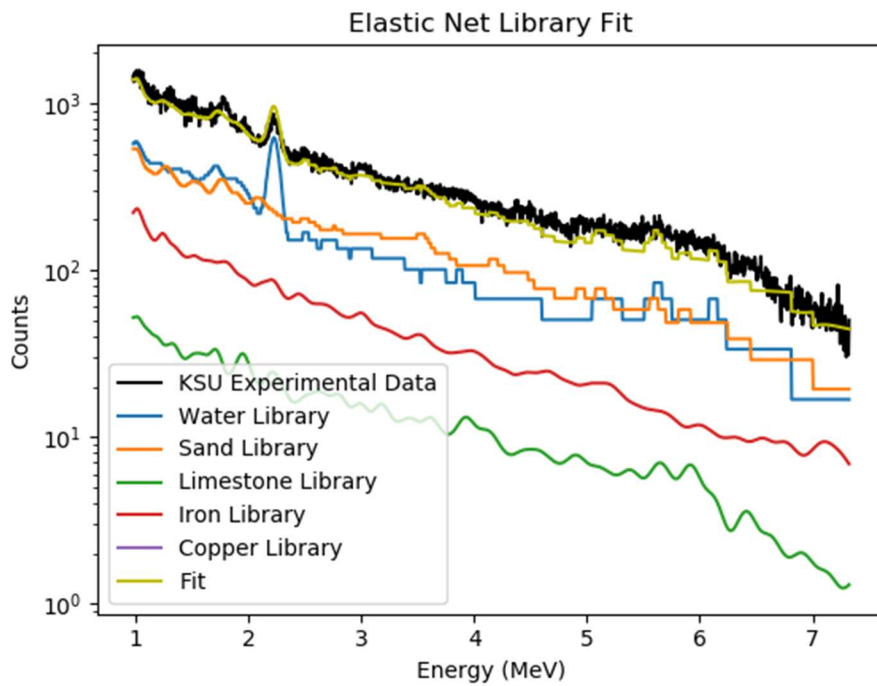


Figure 4-84: Elastic Net fit for the far detector limestone trial

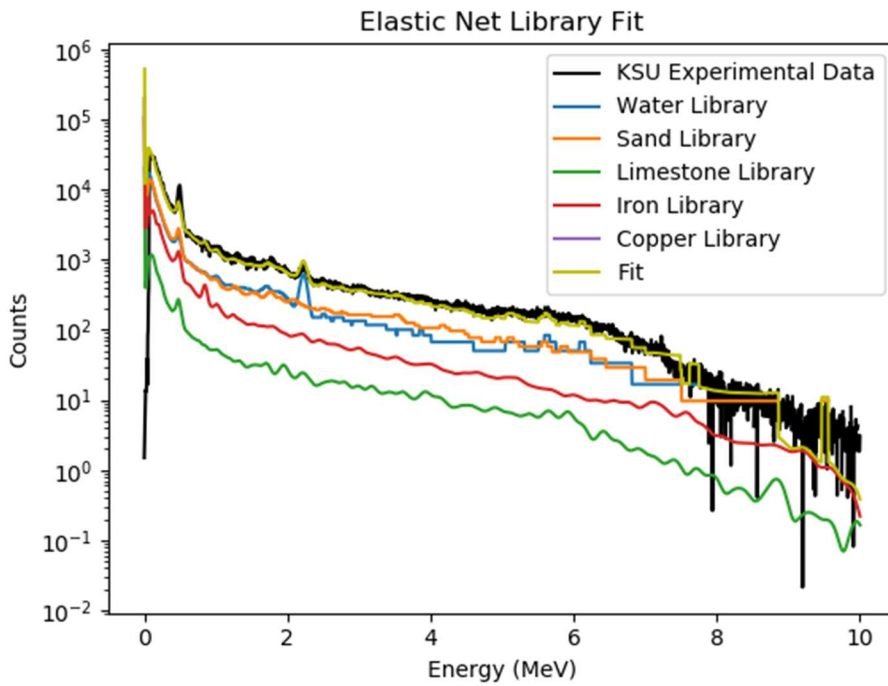


Figure 4-85: Elastic Net full fit for the far detector limestone trial

The results show that both LASSO and Elastic Net recognize the presence of limestone, sand, and water in the near and far detectors. The inclusion of water in each of the results has been attributed to a light rain sustained during the loading of the material. 3 of the 4 tests also include small amounts of iron or copper. Table 4-11 lists the optimal normalization parameters for each case identified by cross validation. The results for the variable selection process are used as inputs for the final ordinary least squares fitting using the cearlls code. Figures 4-86 and 4-87 display the final fitting and residuals for the near and far detector, respectively. Figure 4-88 shows the near and far final fits together. Tables 4-12 and 4-13 provide the chi-squared value, fitting coefficients, and corresponding error.

Table 4-11: Optimal normalization parameters for limestone trial

Limestone Normalization Parameters		
	Near Detector	Far Detector
LASSO	5.384	1.163
Elastic Net	0.419	0.118

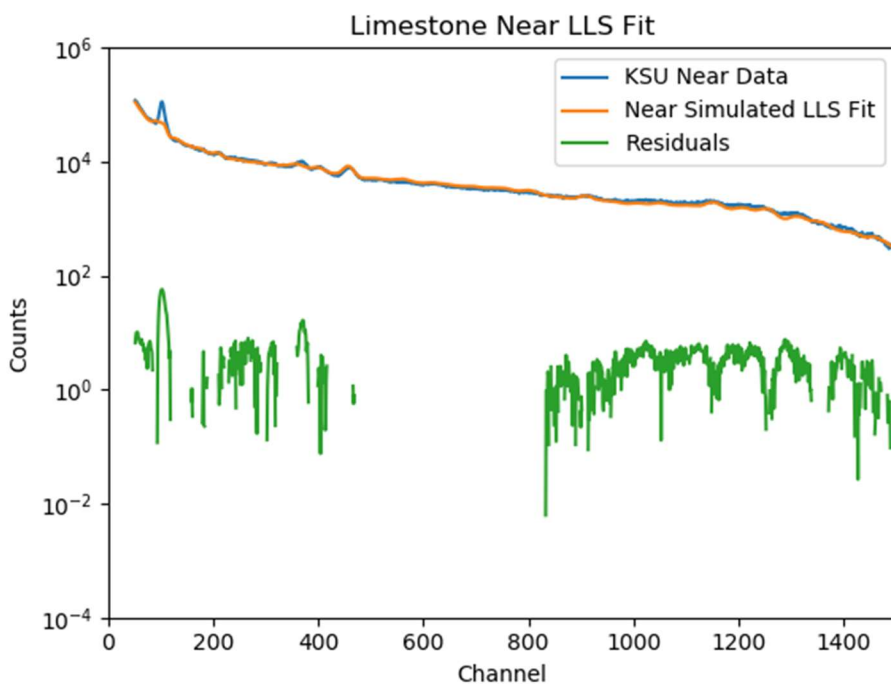


Figure 4-86: Linear least squares fit and residual for the near detector limestone trial

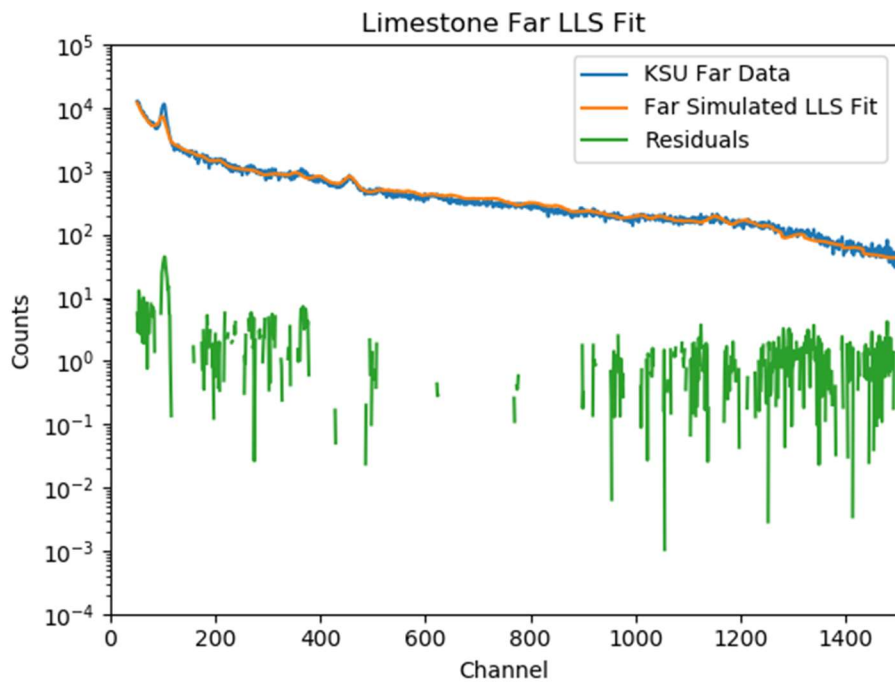


Figure 4-87: Linear least squares fit and residual for the far detector limestone trial

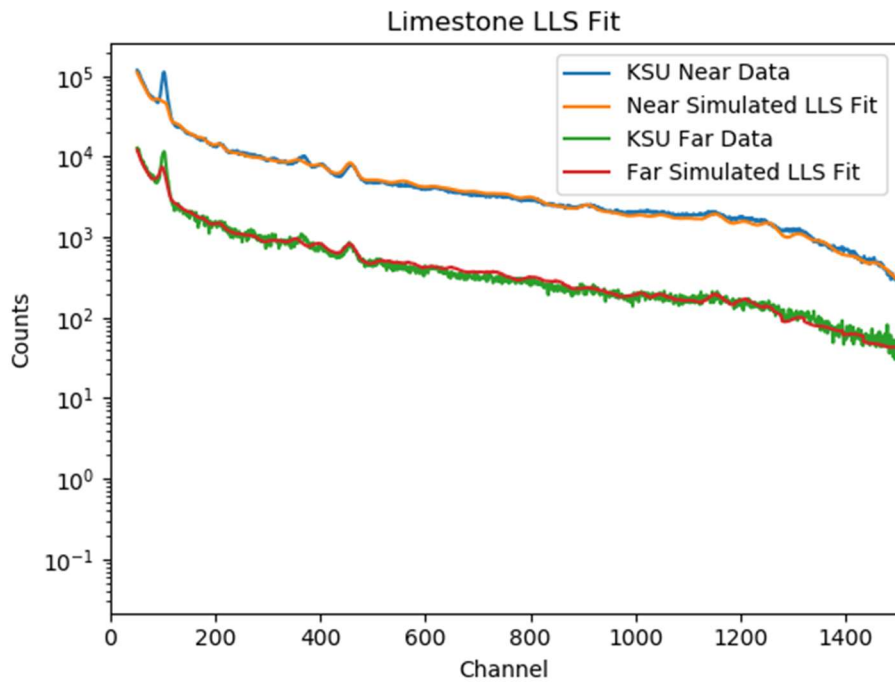


Figure 4-88: Linear least squares fit for near and far detector limestone trials

Table 4-12: Linear coefficients and error for limestone near detector

Limestone Linear Least Squares Results – Near Detector		
Chi-Squared = 26.7	Coefficients	Error
Water	104.44	0.79
Sand	139.82	1.42
Limestone	230.1	1.08
Iron	NA	NA
Copper	NA	NA

Table 4-13: Linear coefficients and error for limestone far detector

Limestone Linear Least Squares Results – Far Detector		
Chi-Squared = 18.2	Coefficients	Error
Water	75.14	2.88
Sand	90.42	3.14
Limestone	171.14	2.31
Iron	NA	NA
Copper	NA	NA

4.3.5 Limestone with Water Trial

The final trial conducted involved limestone with added water. No chemical or other analysis was performed on the material, so it is assumed that the makeup is CaCO₃, SiO₂, and water. The channel to energy conversion was accomplished by identifying the peak centroids in the sample and adjusting by

$$\text{Energy(MeV)} = -.046 + .005063 * \text{channel} + 2e^{-7} * \text{channel}^2 \quad (4.7)$$

All other parameters and order of figures are consistent with those from section 4.3.1.

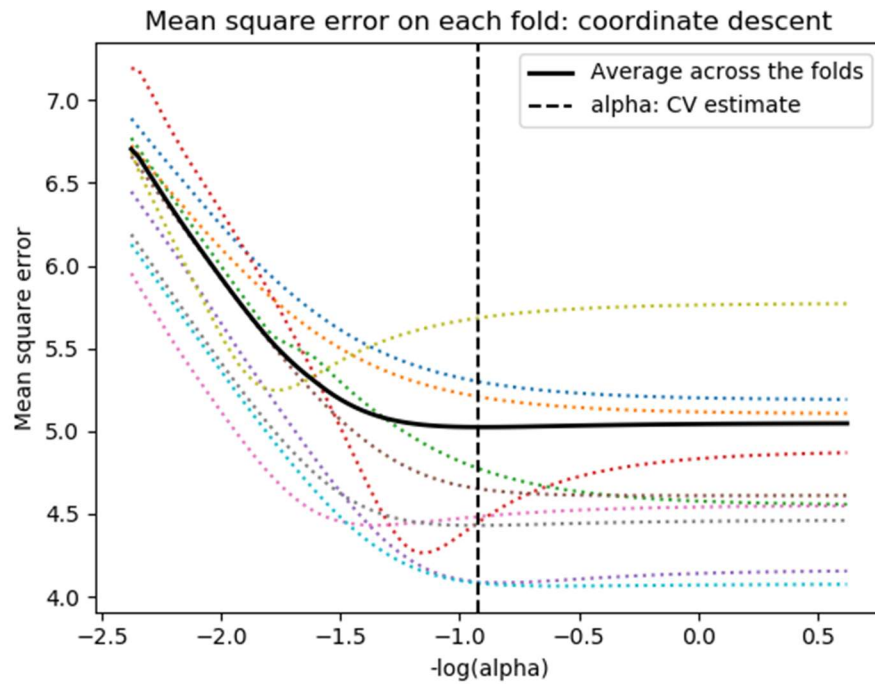


Figure 4-89: Cross validation normalization parameter selection for the LASSO near detector limestone and water trial

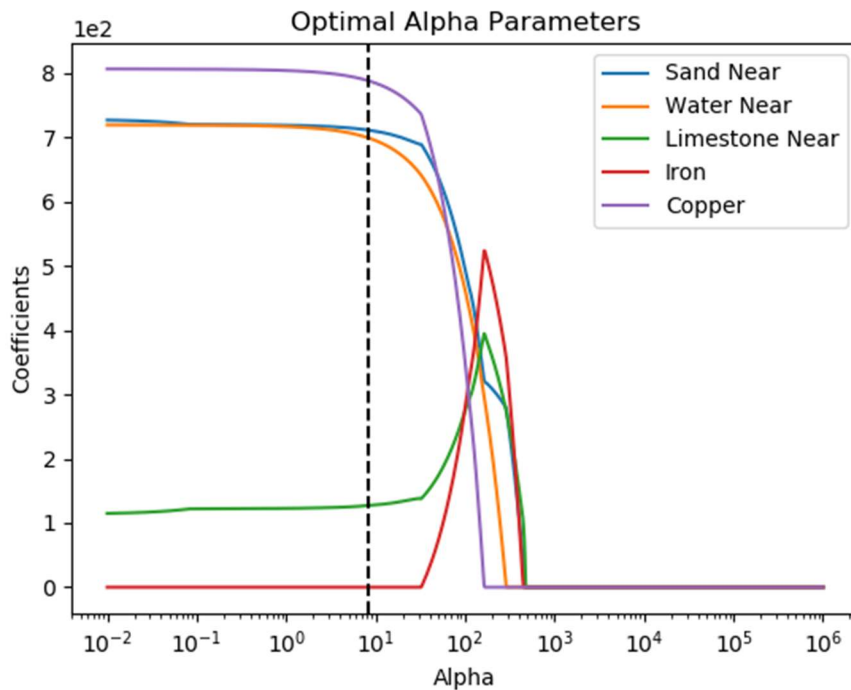


Figure 4-90: LASSO model selection coefficients by changing the normalization parameter for the near detector limestone and water trial

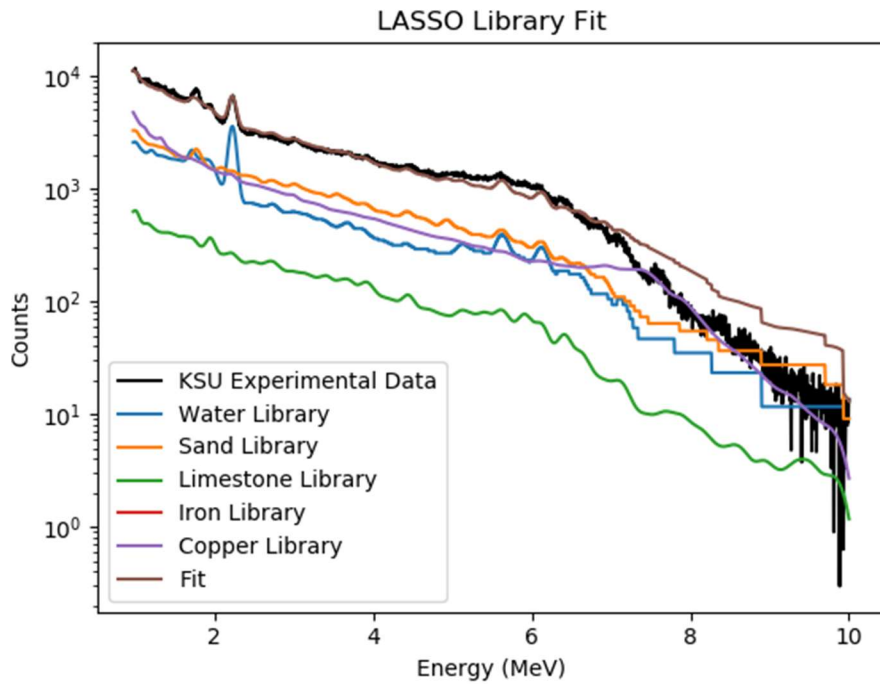


Figure 4-91: LASSO fit for the near detector limestone and water trial

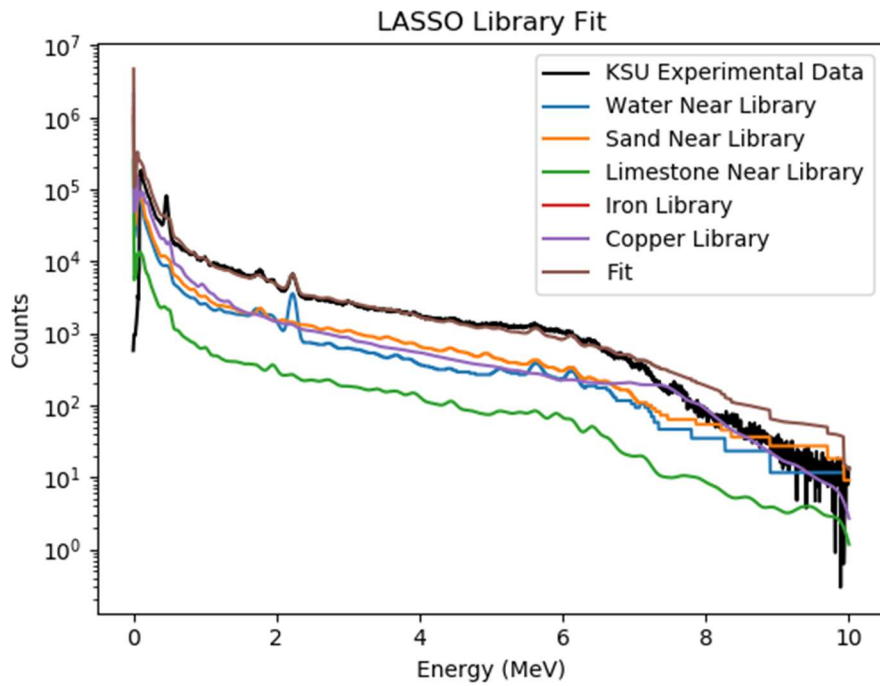


Figure 4-92: LASSO full fit for the near detector limestone and water trial

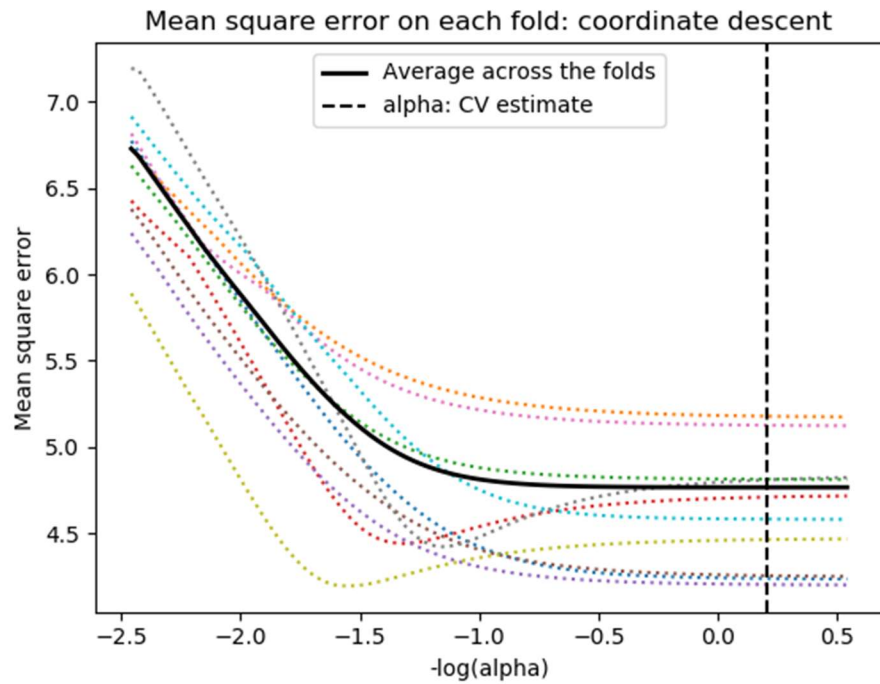


Figure 4-93: Cross validation normalization parameter selection for the Elastic Net near detector limestone and water trial

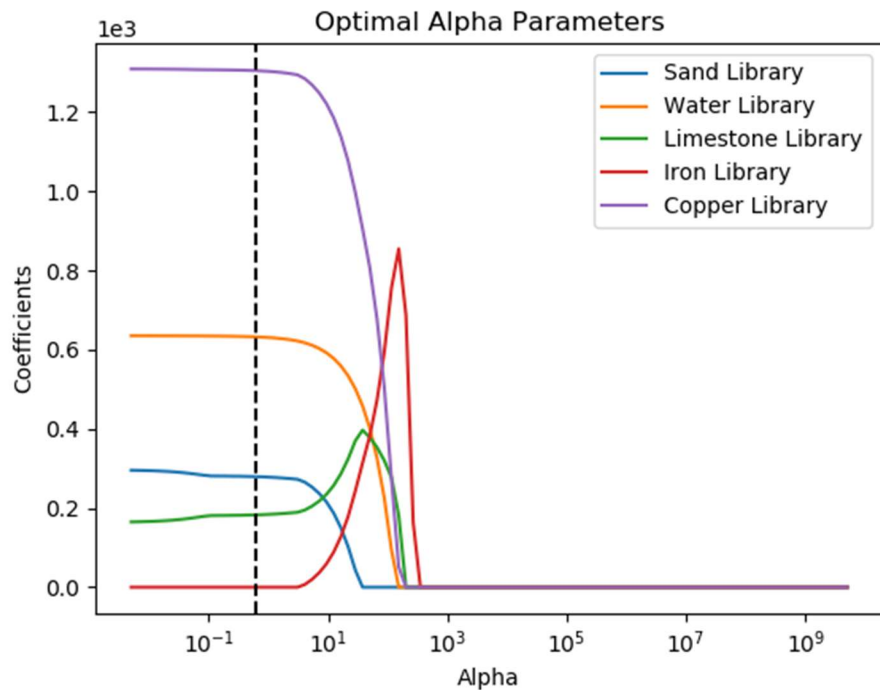


Figure 4-94: Elastic Net model selection coefficients by changing the normalization parameter for the near detector limestone and water trial

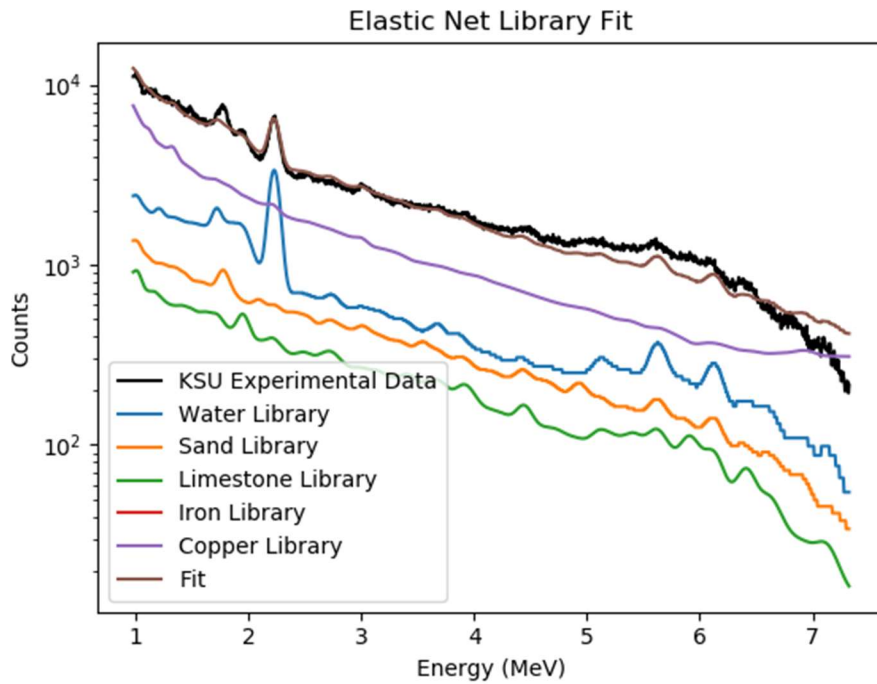


Figure 4-95: Elastic Net fit for the near detector limestone and water trial

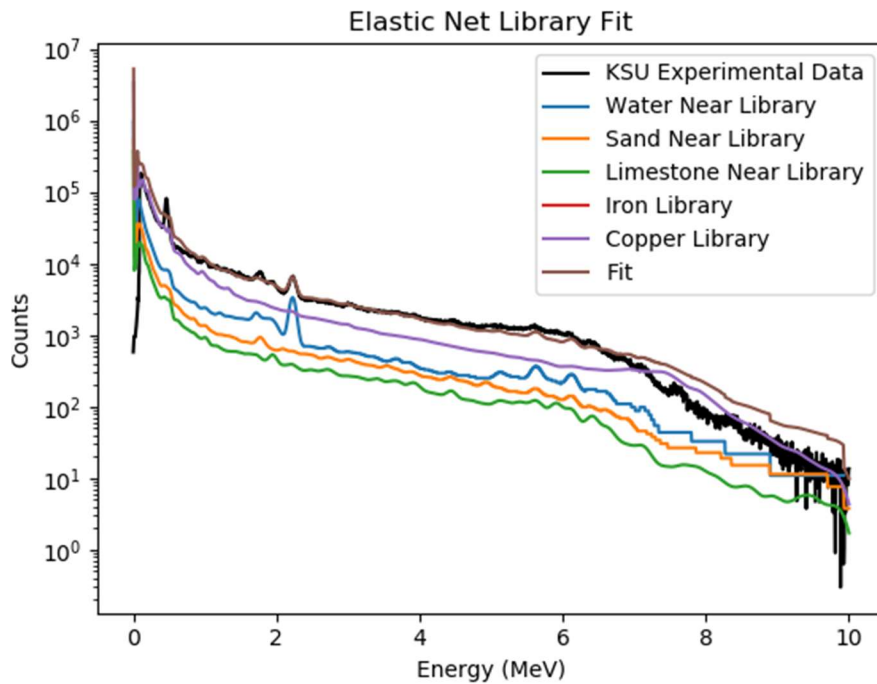


Figure 4-96: Elastic Net full fit for the near detector limestone and water trial

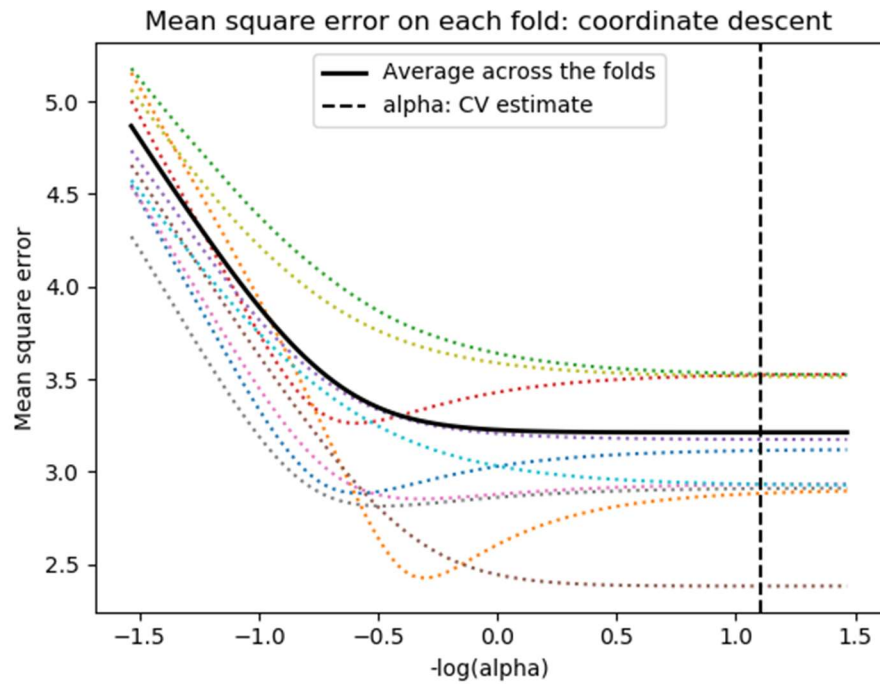


Figure 4-97: Cross validation normalization parameter selection for the LASSO far detector limestone and water trial

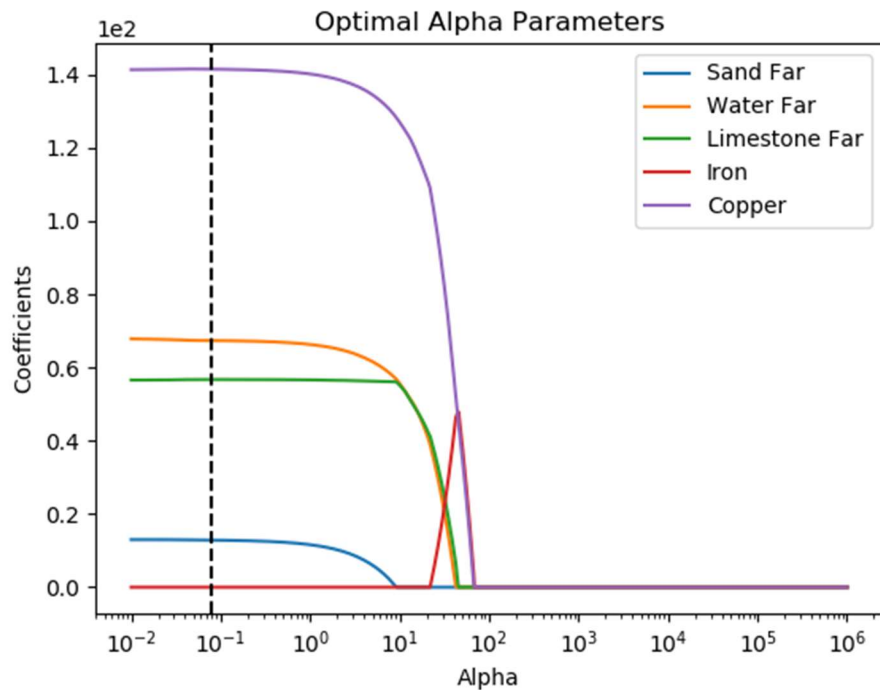


Figure 4-98: LASSO model selection coefficients by changing the normalization parameter for the far detector limestone and water

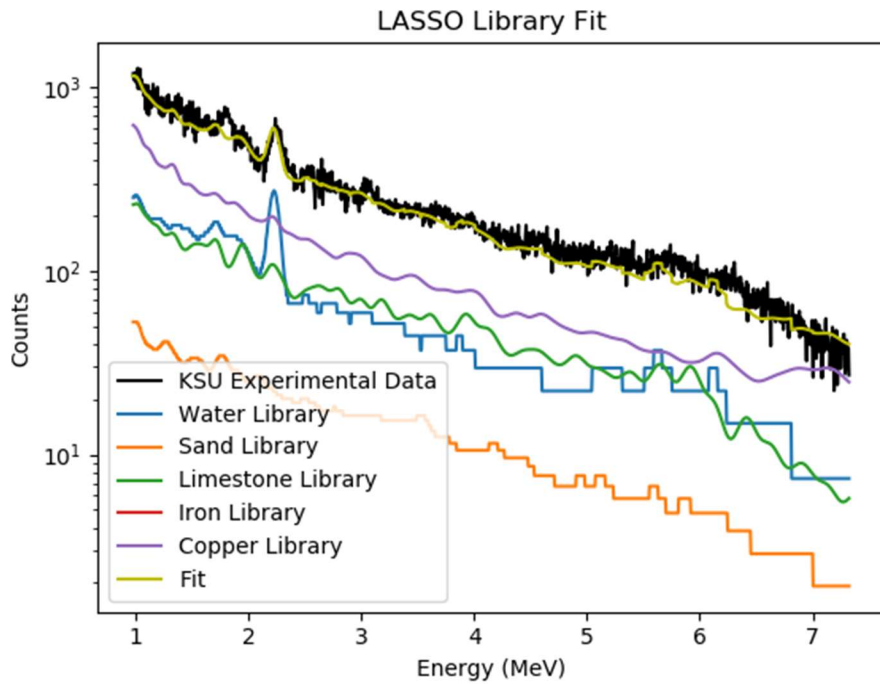


Figure 4-99: LASSO fit for the far detector limestone and water trial

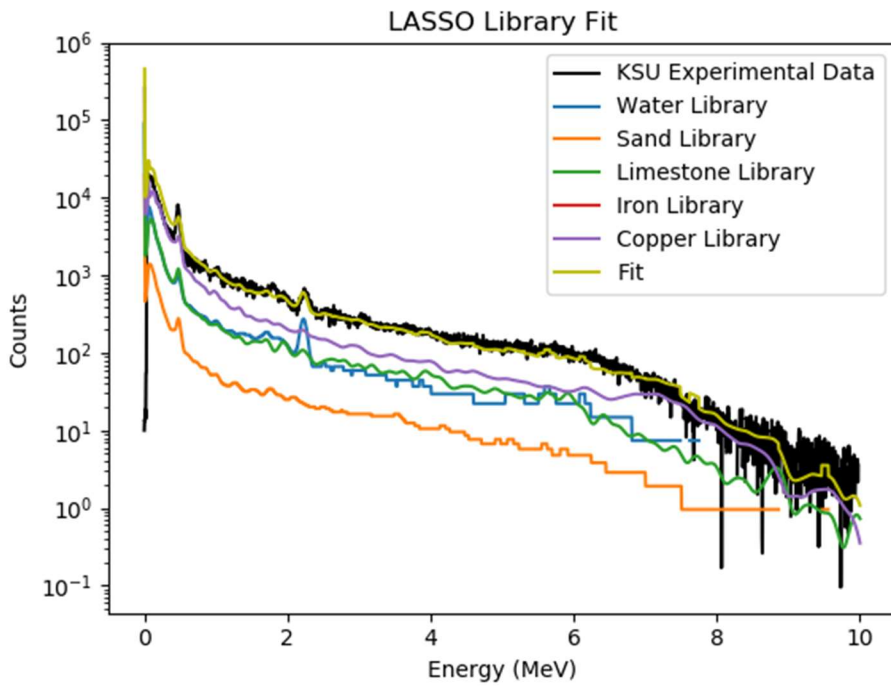


Figure 4-100: LASSO full fit for the far detector limestone and water trial

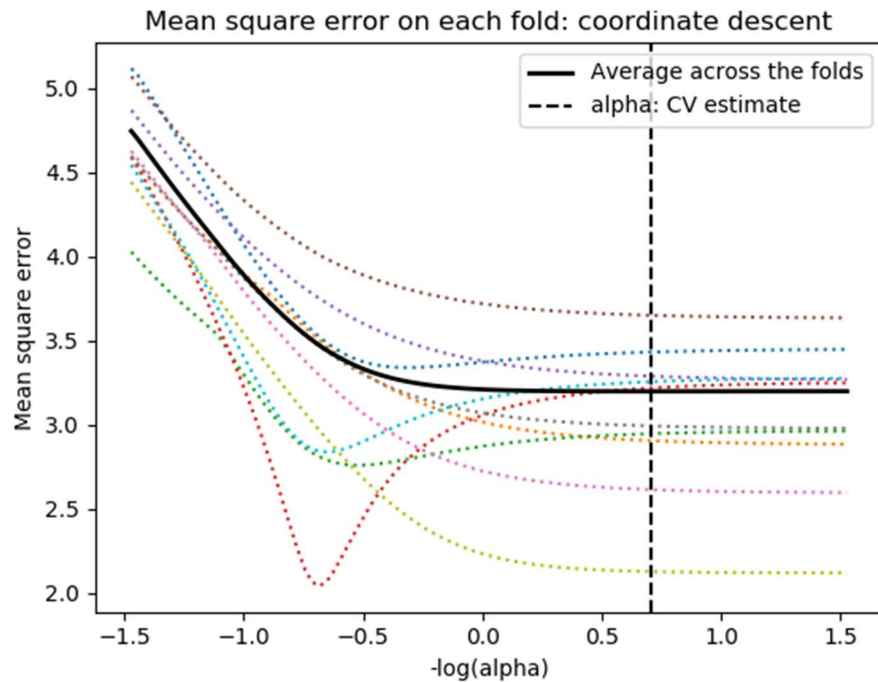


Figure 4-101: Cross validation normalization parameter selection for the Elastic Net far detector limestone and water trial

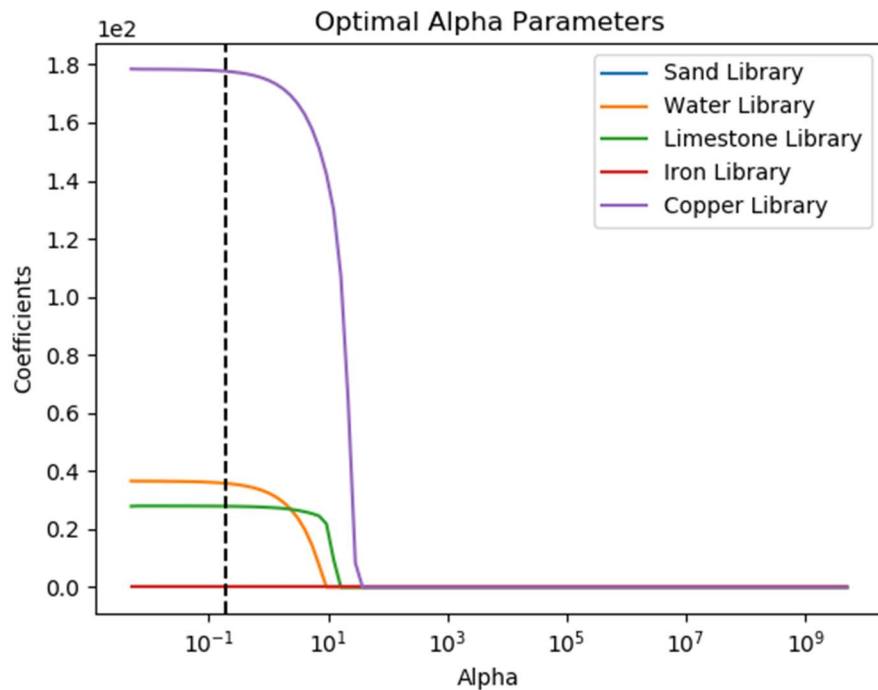


Figure 4-102: Elastic Net model selection coefficients by changing the normalization parameter for the far detector limestone and water trial

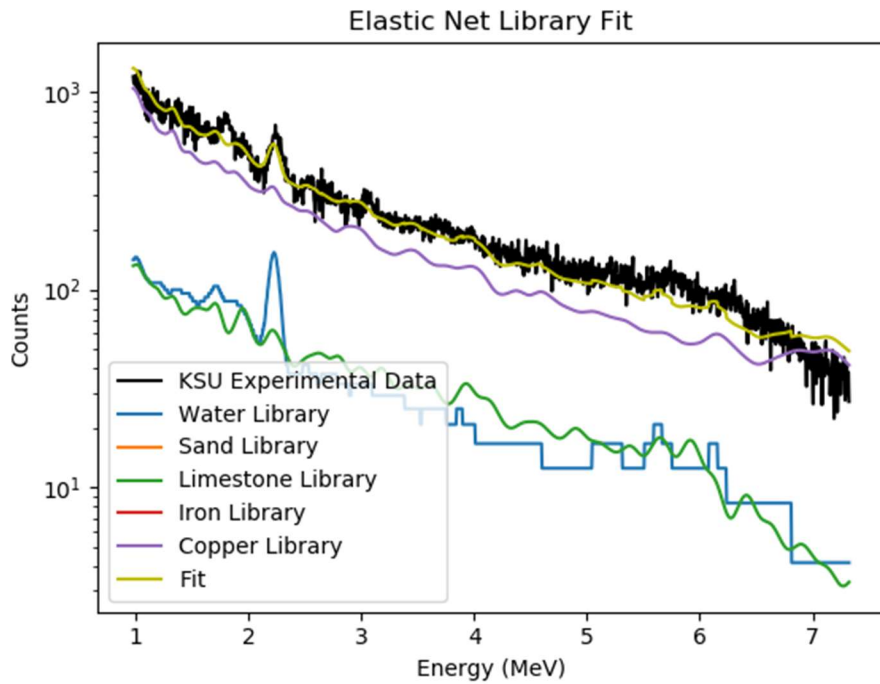


Figure 4-103: Elastic Net fit for the far detector limestone and water trial

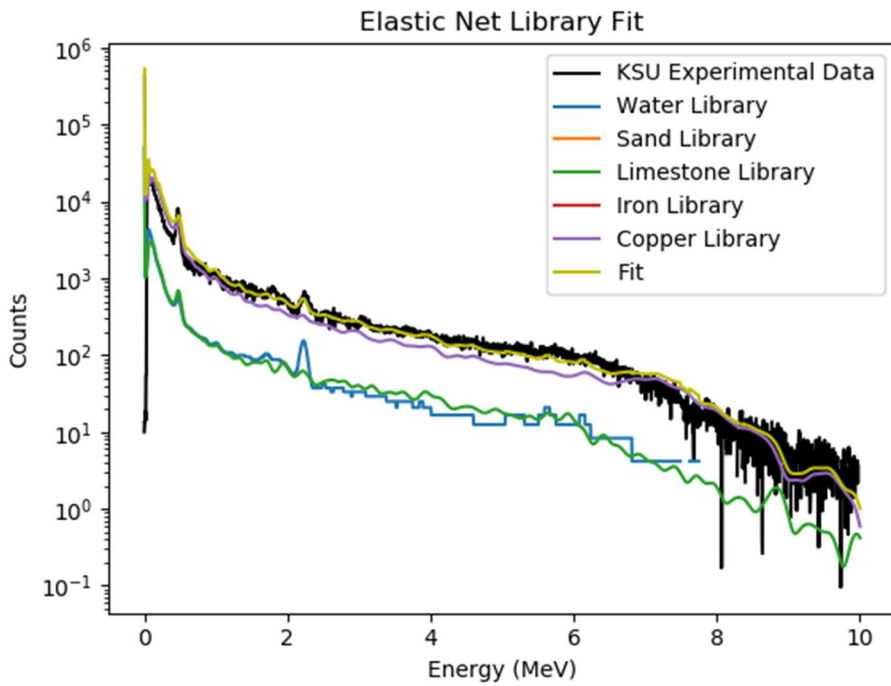


Figure 4-104: Elastic Net full fit for the far detector limestone and water trial

The results show that both LASSO and Elastic Net recognize the presence of limestone, sand, and water in the near and far detectors in 3 of the 4 detectors. Each of the tests also include large amounts of copper. Table 4-14 lists the optimal normalization parameters for each case identified by cross validation. The results for the variable selection process are used as inputs for the final ordinary least squares fitting using the cearlls code. Figures 4-105 and 4-106 display the final fitting and residuals for the near and far detector, respectively. Figure 4-107 shows the near and far final fits together. Tables 4-15 and 4-16 provide the chi-squared value, fitting coefficients, and corresponding error.

Table 4-14: Optimal normalization parameters for limestone and water trial

Limestone with Water Normalization Parameters		
	Near Detector	Far Detector
LASSO	8.362	0.079
Elastic Net	0.619	0.195

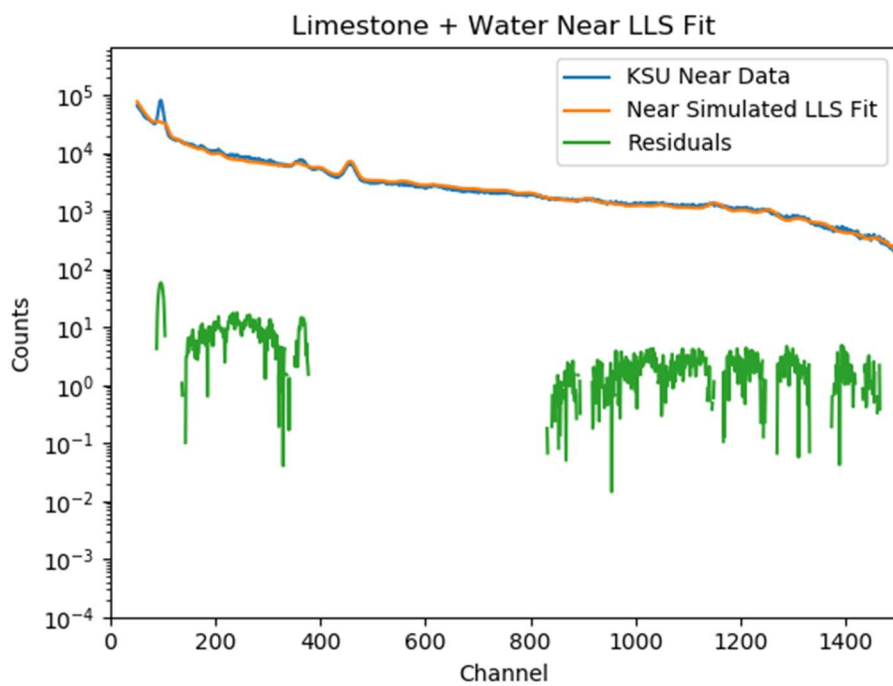


Figure 4-105: Linear least squares fit and residual for the near detector limestone and water trial

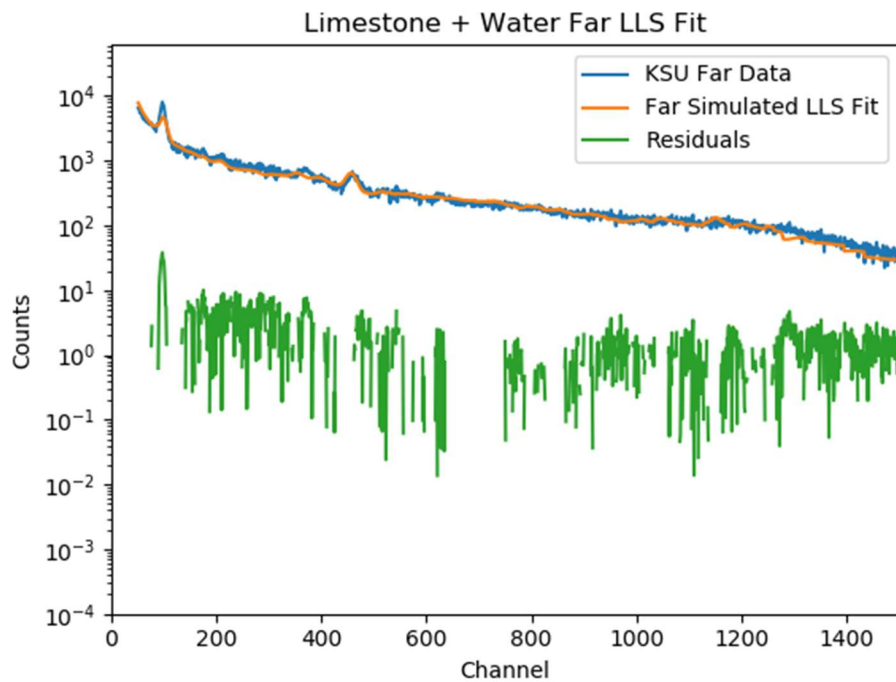


Figure 4-106: Linear least squares fit and residual for the far detector limestone and water trial

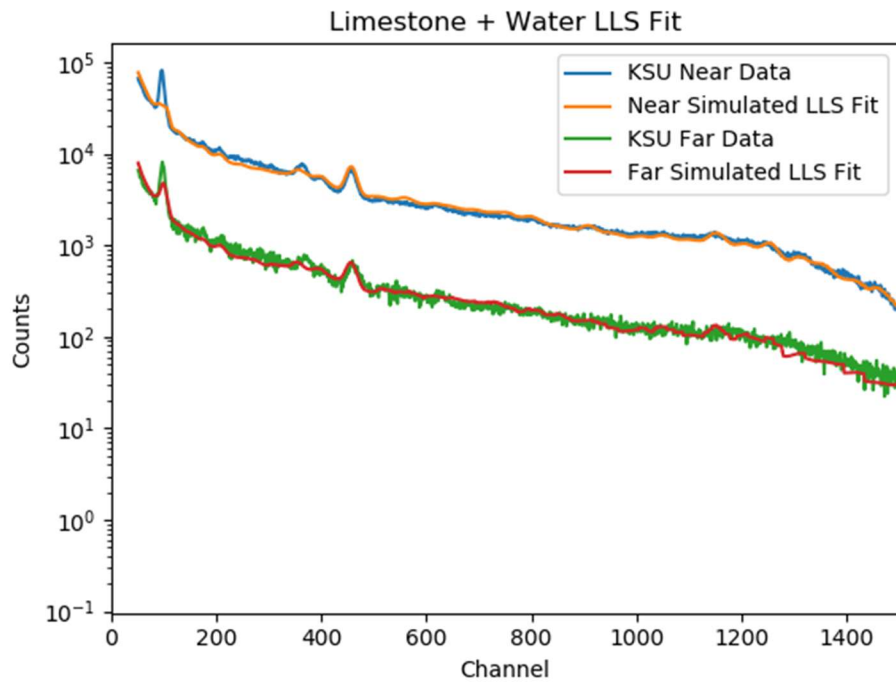


Figure 4-107: Linear least squares fit for near and far detector limestone and water trial

Table 4-15: Linear coefficients and error for limestone and water near detector

Limestone With Water Linear Least Squares Results – Near Detector		
Chi-Squared = 34.2	Coefficients	Error
Water	140.80	0.51
Sand	90.48	1.77
Limestone	114.66	1.76
Iron	NA	NA
Copper	NA	NA

Table 4-16: Linear coefficients and error for limestone and water far detector

Limestone With Water Linear Least Squares Results – Far Detector		
Chi-Squared = 10.2	Coefficients	Error
Water	96.77	1.91
Sand	64.89	3.64
Limestone	71.21	4.61
Iron	NA	NA
Copper	NA	NA

4.4 Discussion

The LASSO and Elastic Net variable selection techniques perform well for both the sand and water trials. The results with the limestone trials show some of the problems if the libraries or data collection are off by any significant amount. During a conversation with oil industry experts, it was noted that calcium cross sections have errors, possibly contributing to the difficulties in the variable selection process for limestone. Additionally, they stated that they are no longer using the far detectors to determine the density of the materials. Further tests should remove the far gamma detector. Improvements continue to be made by both the NC State group and the Kansas State group. Aaron Feinberg is working on a Bayesian approach to fit the non-linear components instead of the basic calculations currently being used. Long Vo is working on separating the time dependent data to improve the background contribution.

CHAPTER 5

Radioisotope Identification

Device Algorithm

5.1 Data Collection

Six radioisotope sources (Ba-133, Na-22, Cs-137, Co-57, Co-60, and Mn-54) were simulated at a distance of 10 cm from the detector face using geometry from a standard 3x3 NaI detector, each with an energy below 1.5 MeV (figs. 5-1, 5-2). Some of the most difficult problems in radioisotope identification involve shielding, masking, and convolution. The masking problem is when several higher energy radioisotopes reduce the signature of a lower energy source, drowning out the contribution in the Compton continuum. Convolved peaks are a major concern in techniques involving peak identification. LASSO and Elastic Net provide a full spectrum analysis, offering a potential solution to this problem. Finally, shielding introduces distortions to the gamma response depending on the materials used, the thickness, and the order of the shielding materials. This investigation looks at each of these problems and demonstrates how LASSO and Elastic Net respond to each. Four separate cases will be investigated: a shielded and unshielded masking and convoluted example. For each, a high, medium, and low count trial will evaluate the effectiveness and limit to each method. The results will be evaluated based on the prediction accuracy using 20 separate runs.

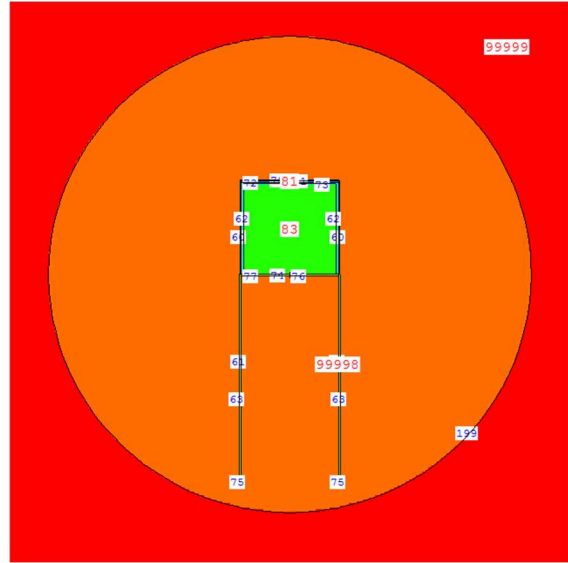


Figure 5-1: Vised depiction of detector geometry

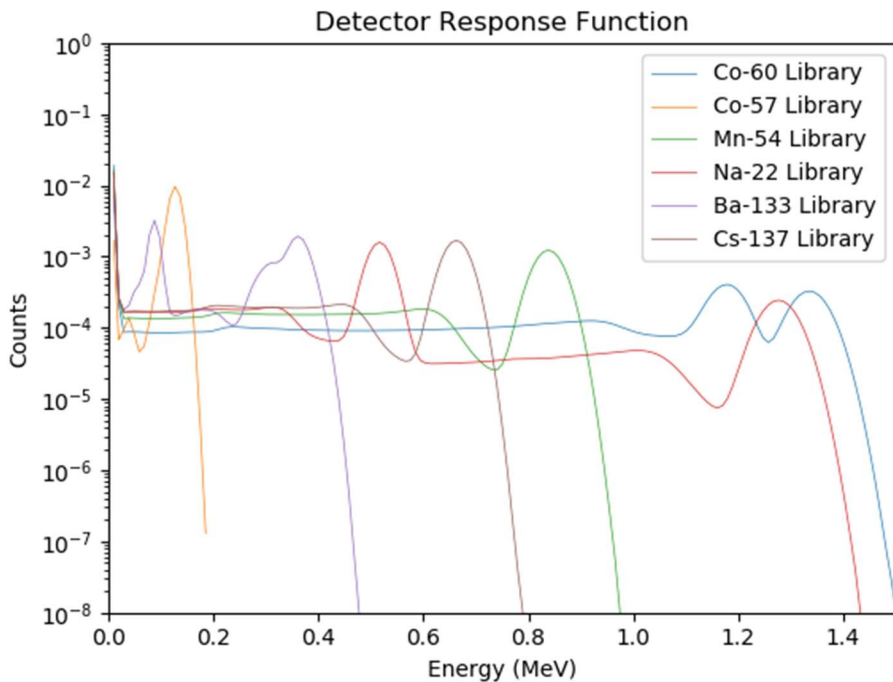


Figure 5-2: MCNP generated radioisotope libraries

5.2 Masking Without Shielding

To replicate an ideal masking situation, a small Co-57 contribution was included to a spectrum with Ba-133, Na-22, and Cs-137. Table 5-1 provides the coefficients used in the generation of

the simulated combination spectrum. Each combination spectrum consists of the library output from MCNP multiplied by the linear coefficient, added to each library used in the combination spectrum, and given random Poisson distributed noise. Figures 5-3 thru 5-8 show a random fit for a low, medium, and high count rate for both LASSO and Elastic Net. Table 5-2 displays the accuracy at predicting the correct components to the model.

Table 5-1: Masking coefficients and total counts

Masking Linear Coefficients			
Ba-133	30,000	300,000	3,000,000
Na-22	100,000	1,000,000	10,000,000
Mn-54	0	0	0
Cs-137	100,000	1,000,000	10,000,000
Co-60	0	0	0
Co-57	5,000	50,000	500,000
Total Counts	4997	50,790	510,348

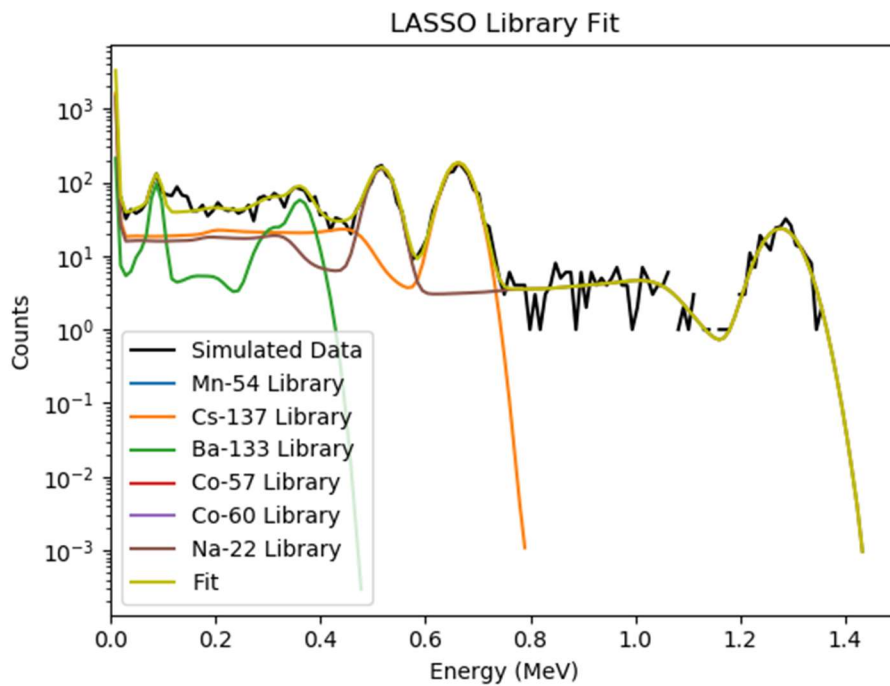


Figure 5-3: LASSO masking low count rate fit

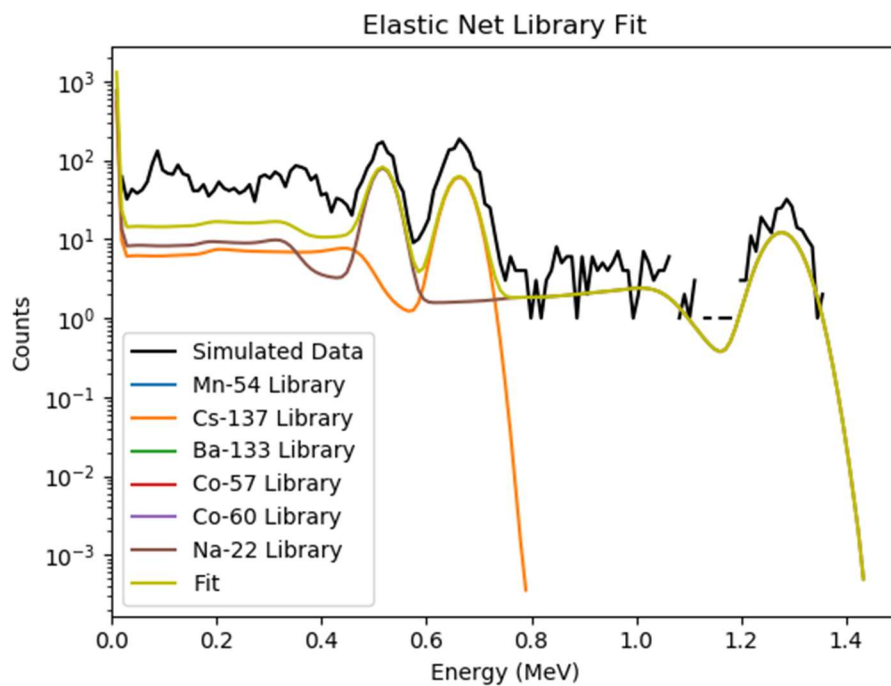


Figure 5-4: Elastic Net masking low count rate fit

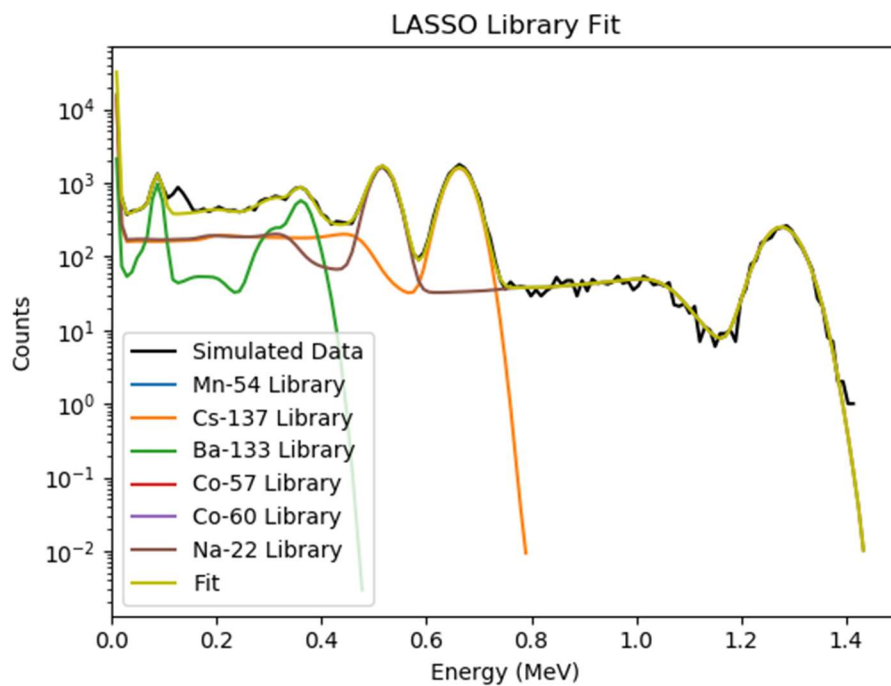


Figure 5-5: LASSO masking medium count rate fit

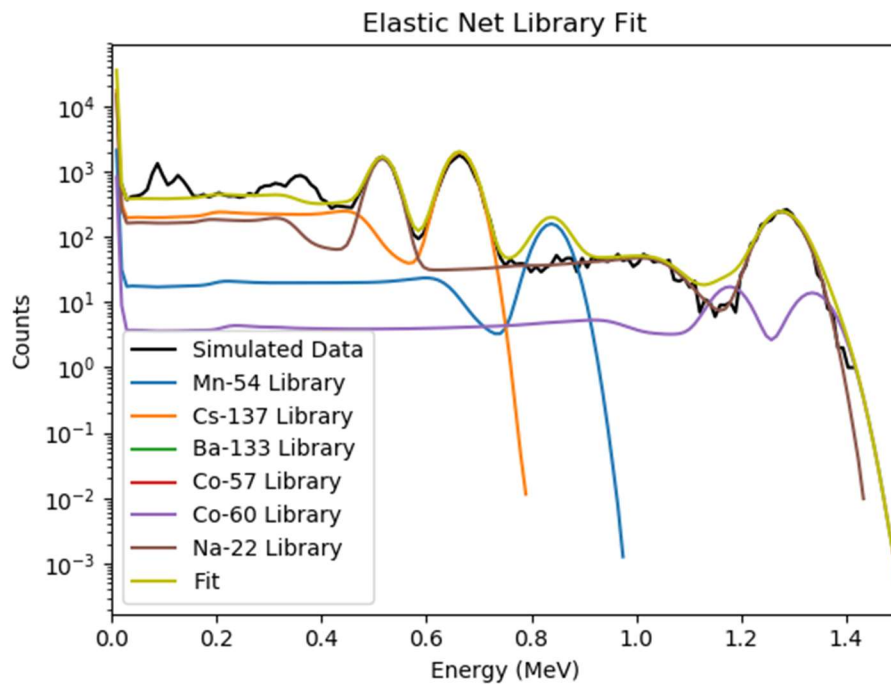


Figure 5-6: Elastic Net masking medium count rate fit

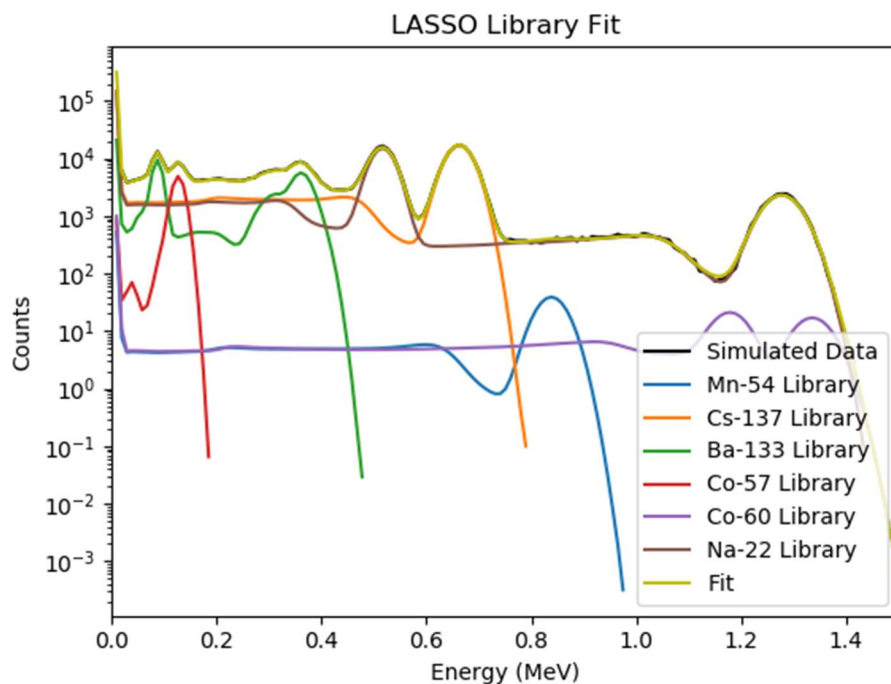


Figure 5-7: LASSO masking high count rate fit

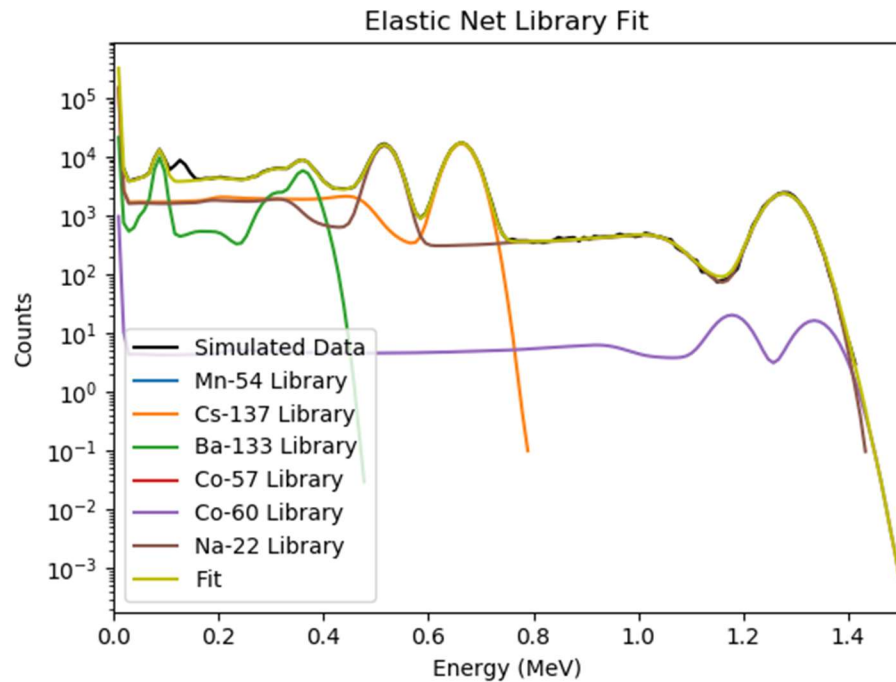


Figure 5-8: Elastic Net masking high count rate fit

Table 5-2: Masking trial prediction accuracy for LASSO and Elastic Net with varying count rates

	Masking Without Shielding Prediction Accuracy					
	Lasso-Low	EN-Low	Lasso-Med	EN-Med	LASSO-High	Elastic Net-High
Ba-133	0.85	0.65	0.95	0.75	1.00	0.85
Na-22	0.95	0.90	1.00	0.95	1.00	1.00
Mn-54	0.65	0.60	0.55	0.55	0.75	0.50
Cs-137	0.95	0.75	1.00	0.90	1.00	0.85
Co-60	0.55	0.40	0.60	0.75	0.75	0.70
Co-57	0.40	0.35	0.50	0.30	0.70	0.40

The results demonstrate that LASSO is far more effective at correctly selecting the correct model. As the count rate is increased, LASSO demonstrates an ability to detect even small contributions of Co-57 at a 70% rate, while only having a false positive rate of 25%.

5.3 Convolution Without Shielding

To replicate an ideal convolution situation, contributions of both Na-22 and Co-60 are used.

Table 5-3 provides the coefficients used in the generation of the simulated combination spectrum. Each combination spectrum consists of the library output from MCNP multiplied by the linear coefficient, added to each library used in the combination spectrum, and given random Poisson distributed noise. Figures 5-9 thru 5-14 show a random fit for a low, medium, and high count rate for both LASSO and Elastic Net. Table 5-4 displays the accuracy at predicting the correct components to the model.

Table 5-3: Convolution coefficients and total counts

Convolution Linear Coefficients			
Ba-133	0	0	0
Na-22	125,000	2,000,000	20,000,000
Mn-54	0	0	0
Cs-137	20,000	200,000	2,000,000
Co-60	100,000	1,000,000	10,000,000
Co-57	5,000	50,000	500,000
Total Counts	4,817	64,407	646,974

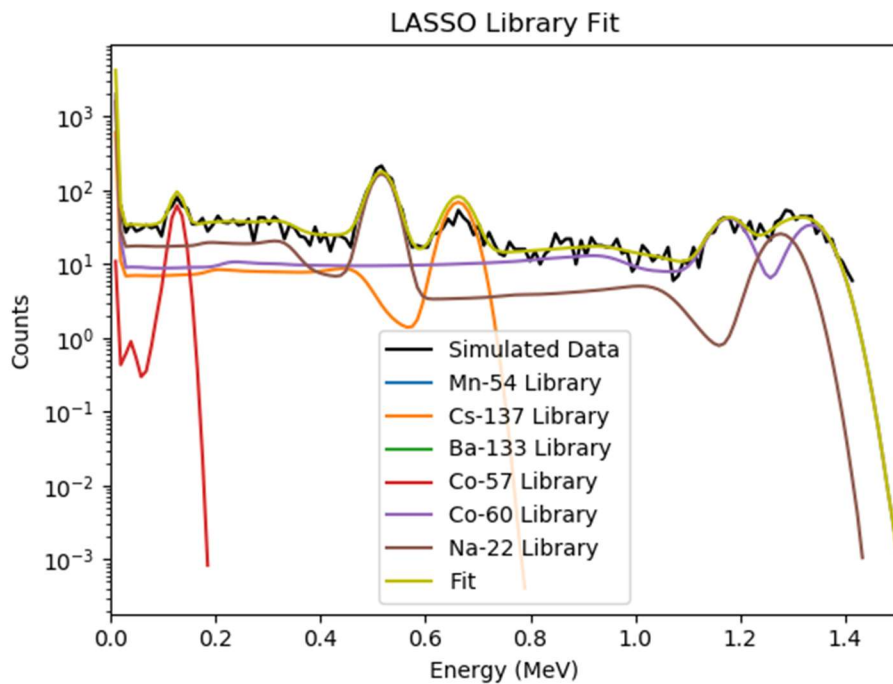


Figure 5-9: LASSO convolution low count rate fit

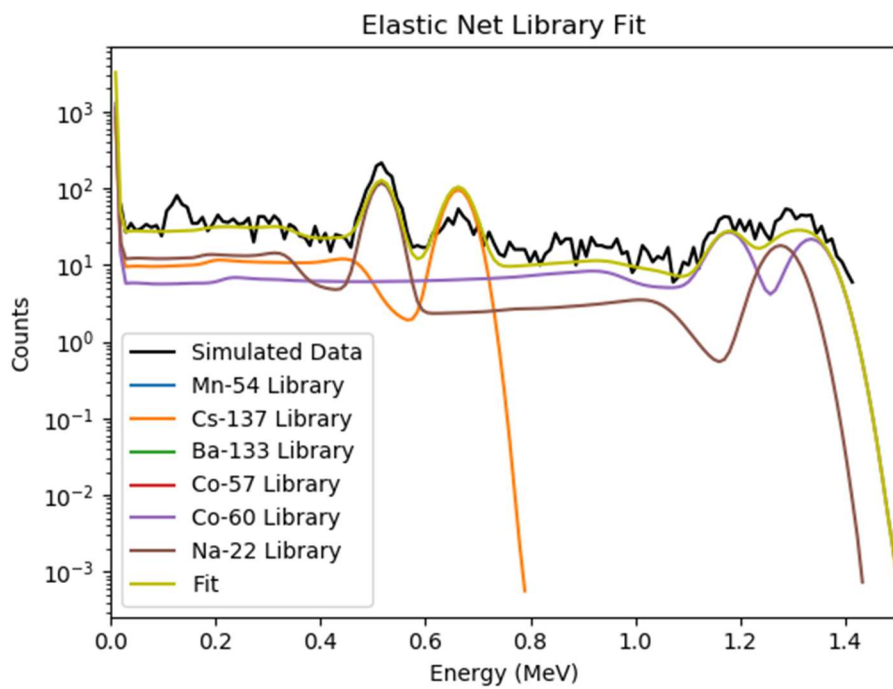


Figure 5-10: Elastic Net convolution low count rate fit

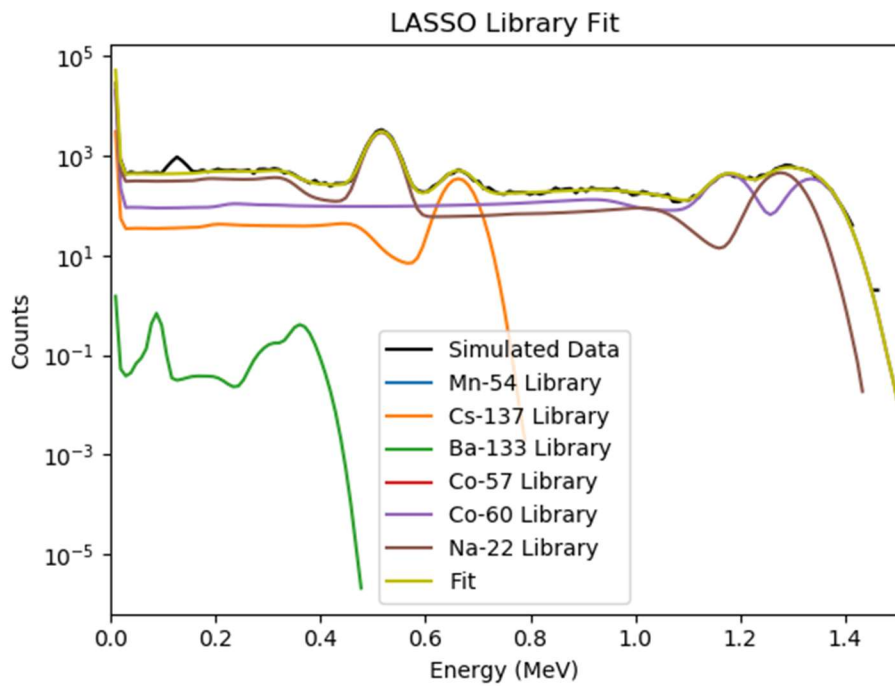


Figure 5-11: LASSO convolution medium count rate fit

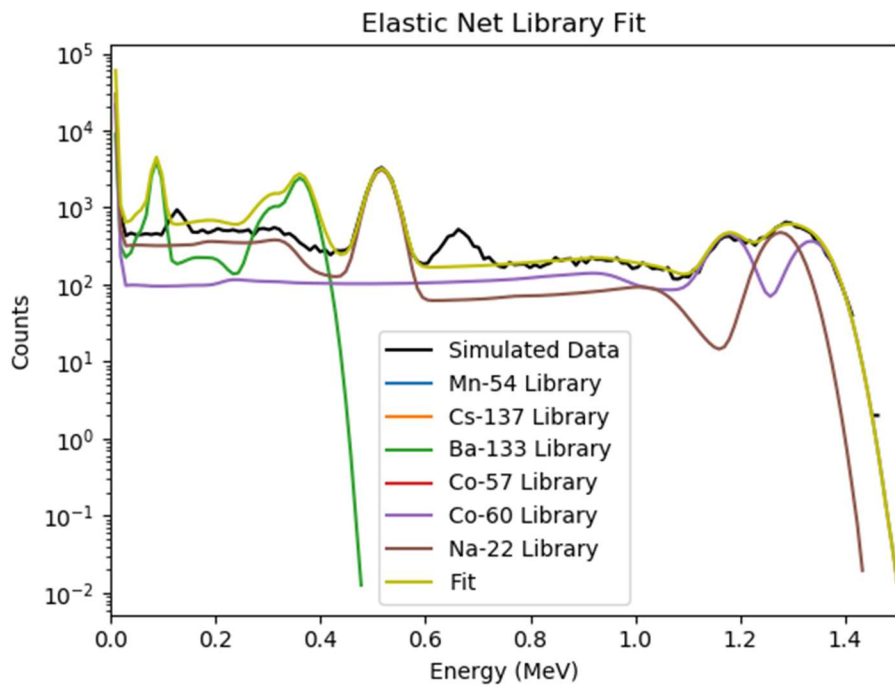


Figure 5-12: Elastic Net convolution medium count rate fit

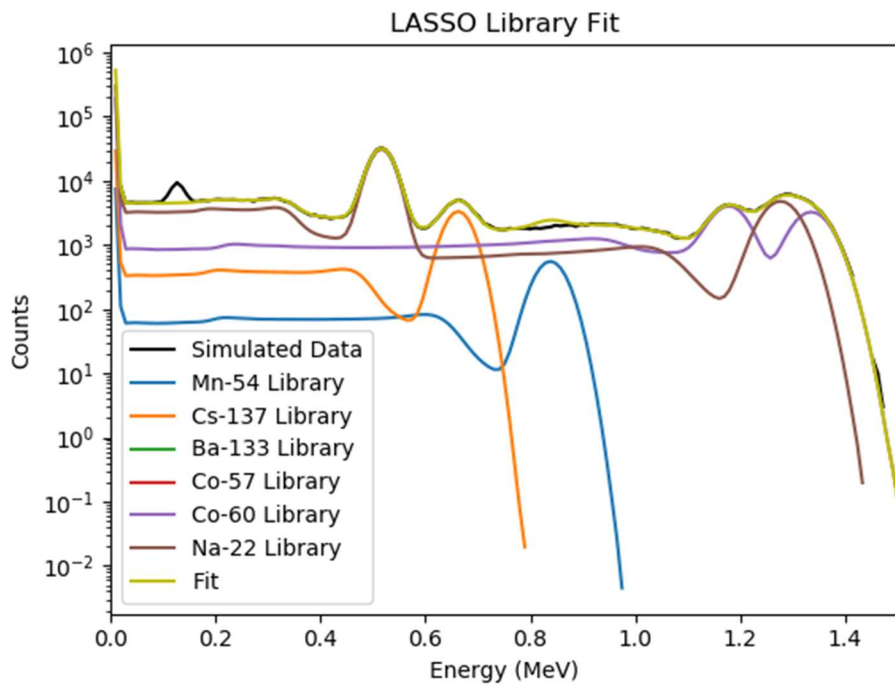


Figure 5-13: LASSO convolution high count rate fit

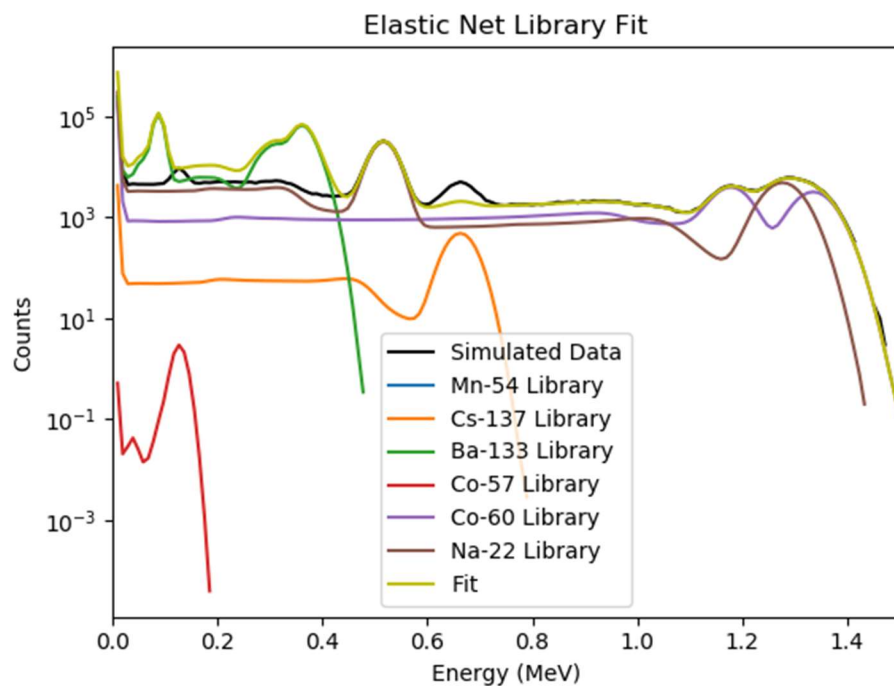


Figure 5-14: Elastic Net convolution high count rate fit

Table 5-4: Convolution trial prediction accuracy for LASSO and Elastic Net with varying count rates

Convolution Without Shielding Prediction Accuracy						
	Lasso-Low	EN-Low	Lasso-Med	EN-Med	LASSO-High	Elastic Net-High
Ba-133	0.90	0.90	0.75	0.80	0.60	0.80
Na-22	1.00	0.95	1.00	1.00	1.00	1.00
Mn-54	0.75	0.95	0.80	0.65	0.65	0.65
Cs-137	0.85	0.75	0.90	0.75	1.00	0.95
Co-60	1.00	0.95	1.00	1.00	1.00	1.00
Co-57	0.15	0.10	0.60	0.35	0.45	0.50

The results demonstrate that LASSO is far more effective at accurately selecting the correct model for the convolved peak application. As the count rate is increased, LASSO demonstrates an ability to decipher contributions of both Co-60 and Na-22 at 100% rate, while only having a false positive rate of 35%. Co-57 has a minor contribution to the overall spectrum and with the highest prediction rate of 60%, this demonstrates that the contribution may be close to the detectable limit for these methods.

5.4 Masking with Shielding

To perform the masking with shielding problem, the same steps from section 5.2 were taken. In order to create a different response, shielded libraries using 1 inch of aluminum placed half way between the detector and source were used to create the combination spectrum. Table 5-5 provides the coefficients used in the generation of the simulated combination spectrum. Figures 5-15 thru 5-20 show a random fit for a low, medium, and high count rate for both LASSO and Elastic Net. Table 5-6 displays the accuracy at predicting the correct components to the model.

Table 5-5: Masking with Shielding coefficients and total counts

Masking with Shielding Linear Coefficients			
Ba-133	30,000	300,000	3,000,000
Na-22	100,000	1,000,000	10,000,000
Mn-54	0	0	0
Cs-137	100,000	1,000,000	10,000,000
Co-60	0	0	0
Co-57	5,000	50,000	500,000
Total Counts	4956	50,625	509,744

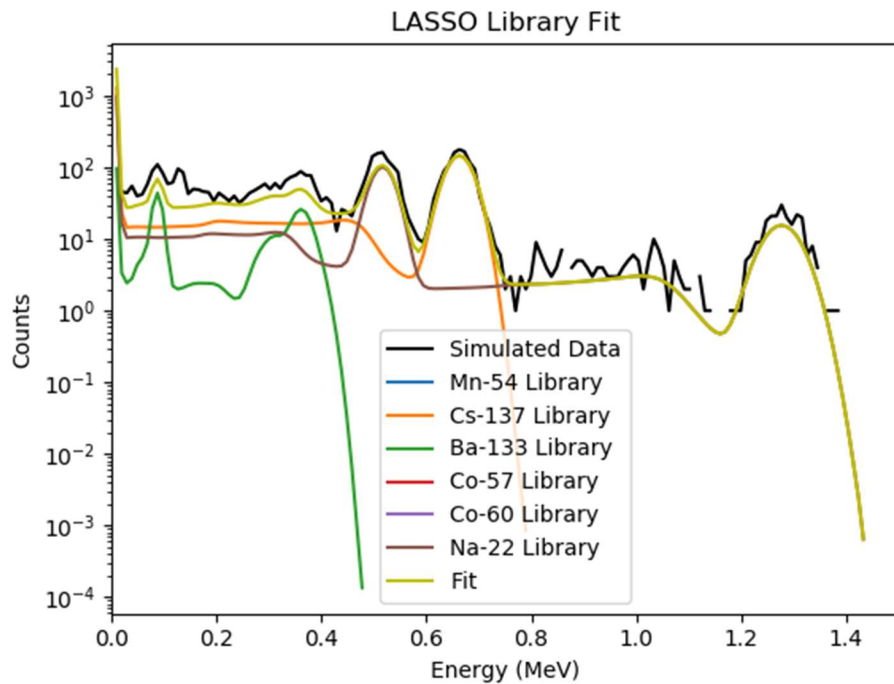


Figure 5-15: LASSO masking with shielding low count rate fit

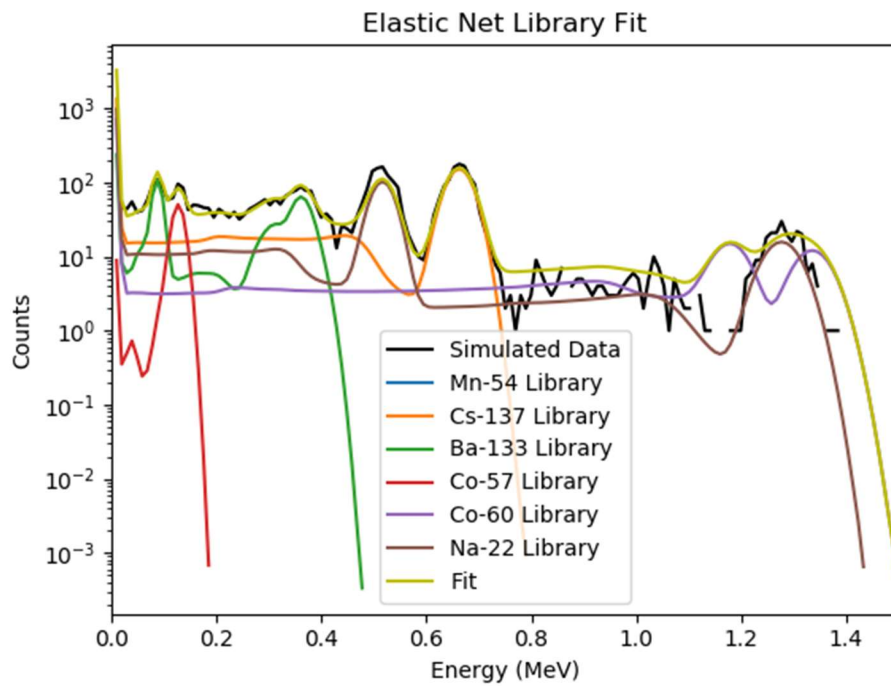


Figure 5-16: Elastic Net masking with shielding low count rate fit

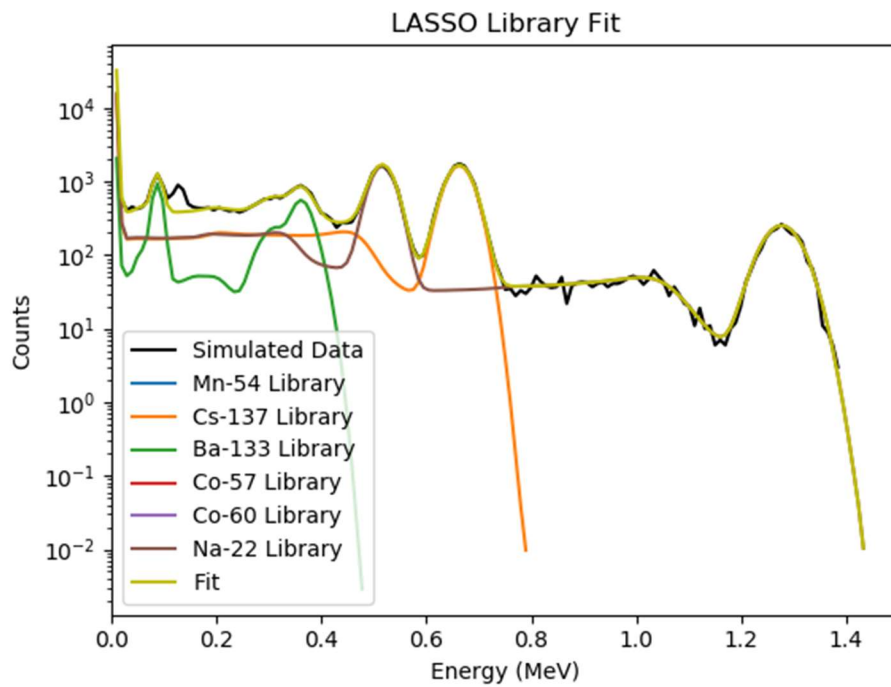


Figure 5-17: LASSO masking with shielding medium count rate fit

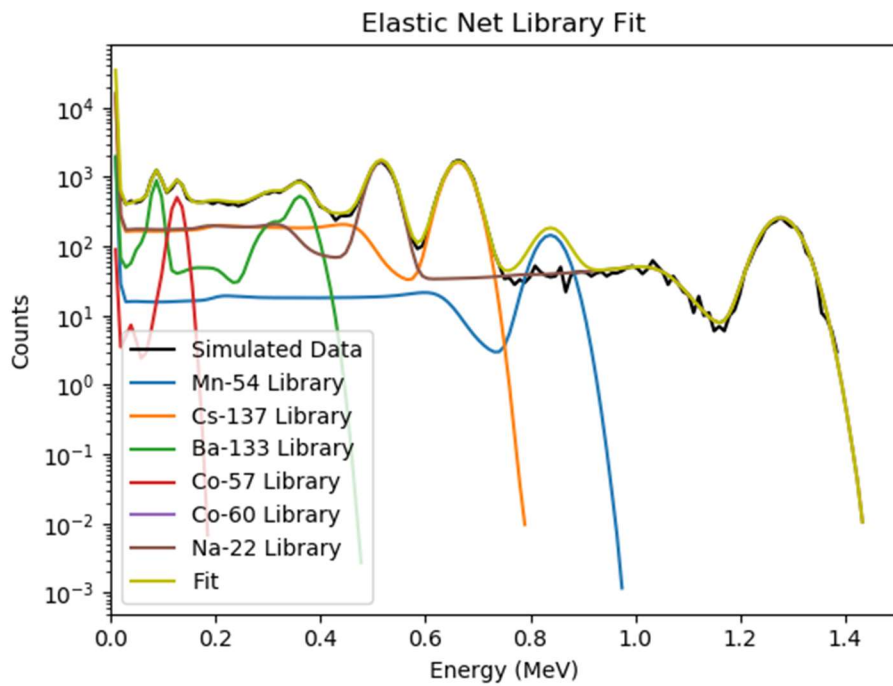


Figure 5-18: Elastic Net masking with shielding medium count rate fit

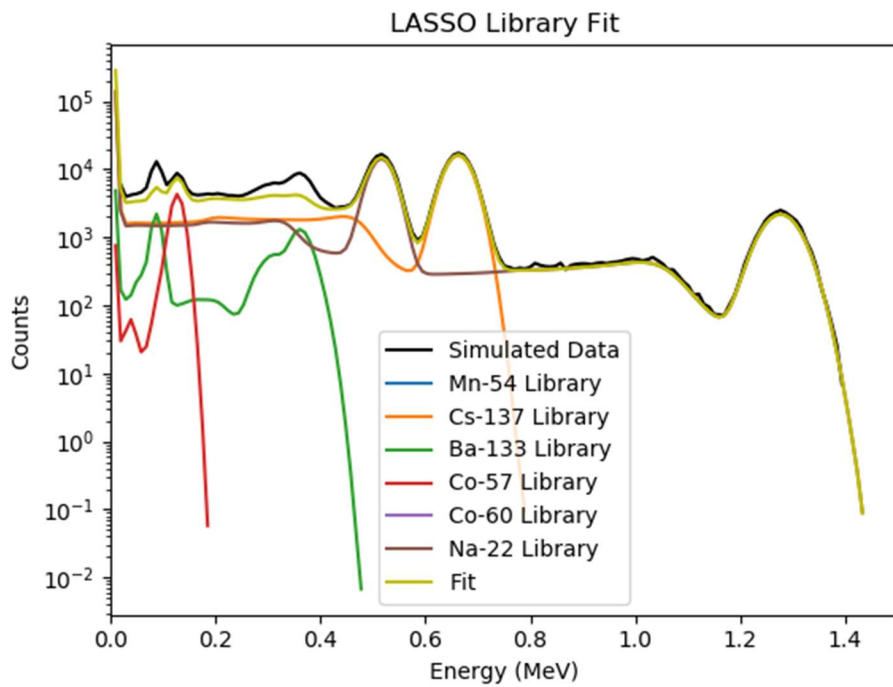


Figure 5-19: LASSO masking with shielding high count rate fit

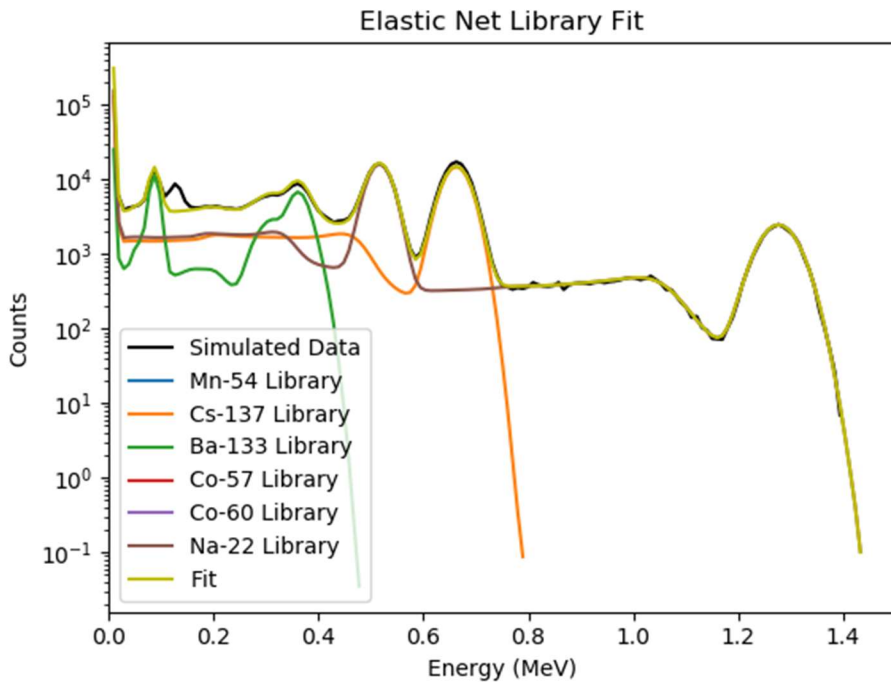


Figure 5-20: Elastic Net masking with shielding high count rate fit

Table 5-6: Masking with shielding trial prediction accuracy for LASSO and Elastic Net with varying count rates

	Masking with Shielding Prediction Accuracy						
	Lasso-Low	EN-Low	Lasso-Med	EN-Med	LASSO-High	Elastic Net-High	
Ba-133	0.80	0.55	0.90	0.70	1.00	0.80	
Na-22	1.00	0.90	1.00	0.90	1.00	1.00	
Mn-54	0.55	0.55	0.60	0.65	0.70	0.65	
Cs-137	0.85	0.75	0.95	0.80	1.00	0.85	
Co-60	0.70	0.30	0.60	0.75	0.80	0.70	
Co-57	0.35	0.30	0.35	0.25	0.55	0.35	

The results demonstrate that LASSO is far more effective at correctly selecting the correct model. As the count rate is increased, LASSO demonstrates an ability to detect even small contributions of Co-57 at a 55% rate, while only having a false positive rate of 30%.

5.5 Convolution with Shielding

To replicate an ideal convolution with shielding situation the same steps from section 5.3 were taken. In order to create a different response, shielded libraries using 1 inch of aluminum placed halfway between the detector and source were used to create the combination spectrum. Table 5-

7 provides the coefficients used in the generation of the simulated combination spectrum. Figures 5-21 thru 5-26 show a random fit for a low, medium, and high count rate for both LASSO and Elastic Net. Table 5-8 displays the accuracy at predicting the correct components to the model.

Table 5-7: Convolution with shielding coefficients and total counts

Convolution with Shielding Linear Coefficients			
Ba-133	0	0	0
Na-22	125,000	2,000,000	20,000,000
Mn-54	0	0	0
Cs-137	20,000	200,000	2,000,000
Co-60	100,000	1,000,000	10,000,000
Co-57	5,000	50,000	500,000
Total Counts	4,387	61,327	61,756

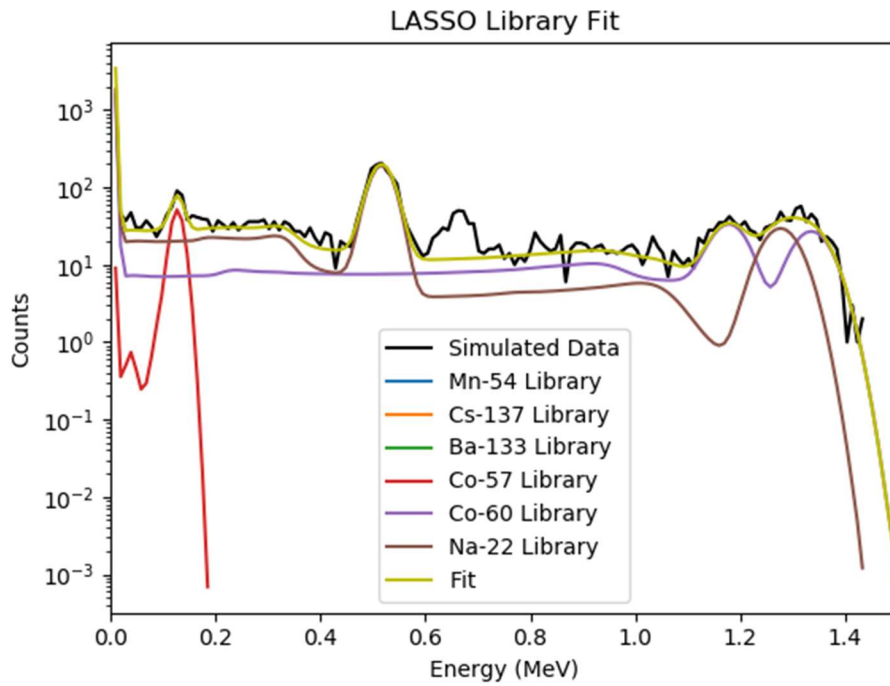


Figure 5-21: LASSO convolution with shielding low count rate fit

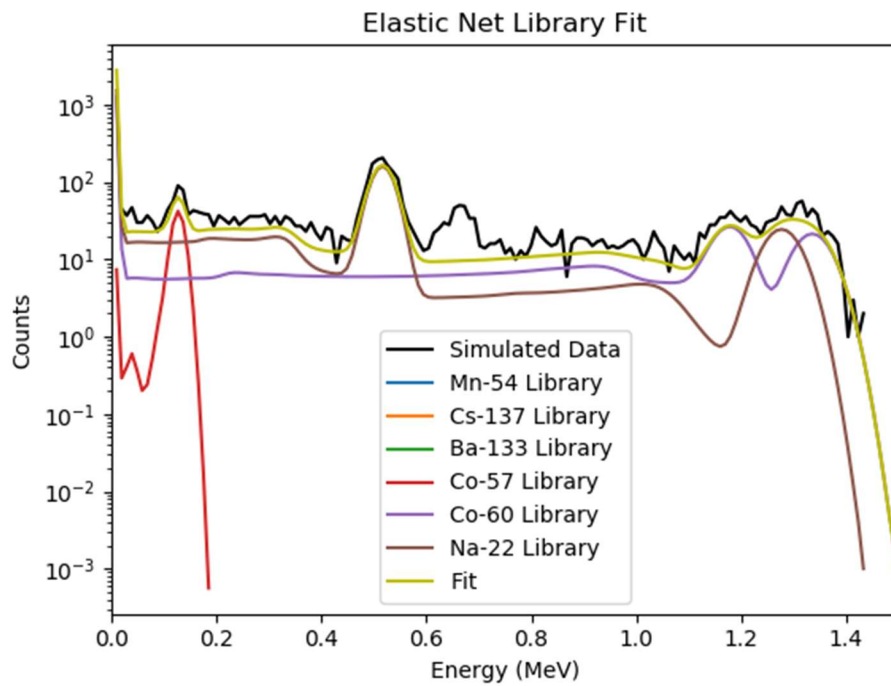


Figure 5-22: Elastic Net convolution with shielding low count rate fit

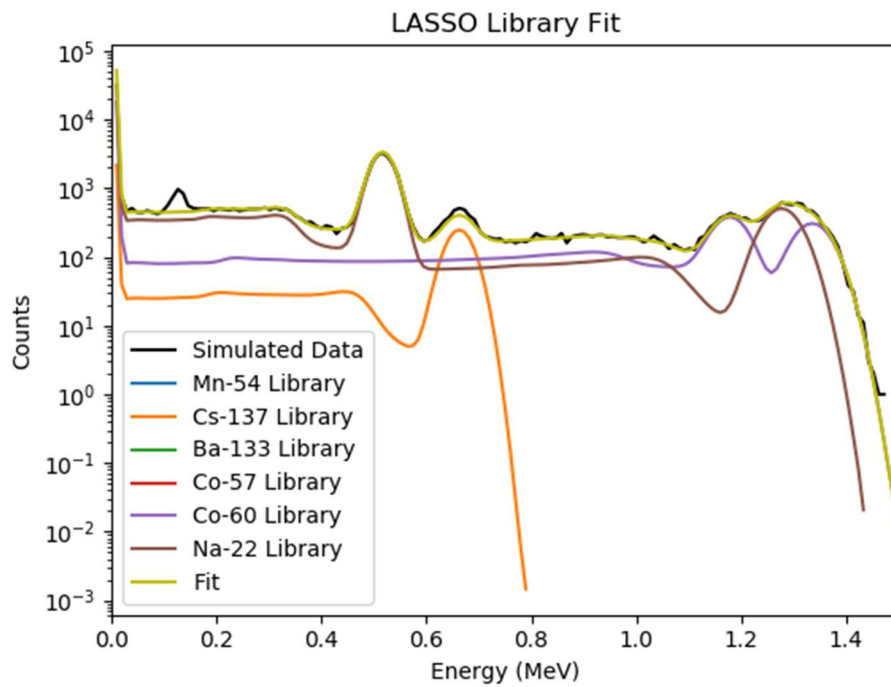


Figure 5-23: LASSO convolution with shielding medium count rate fit

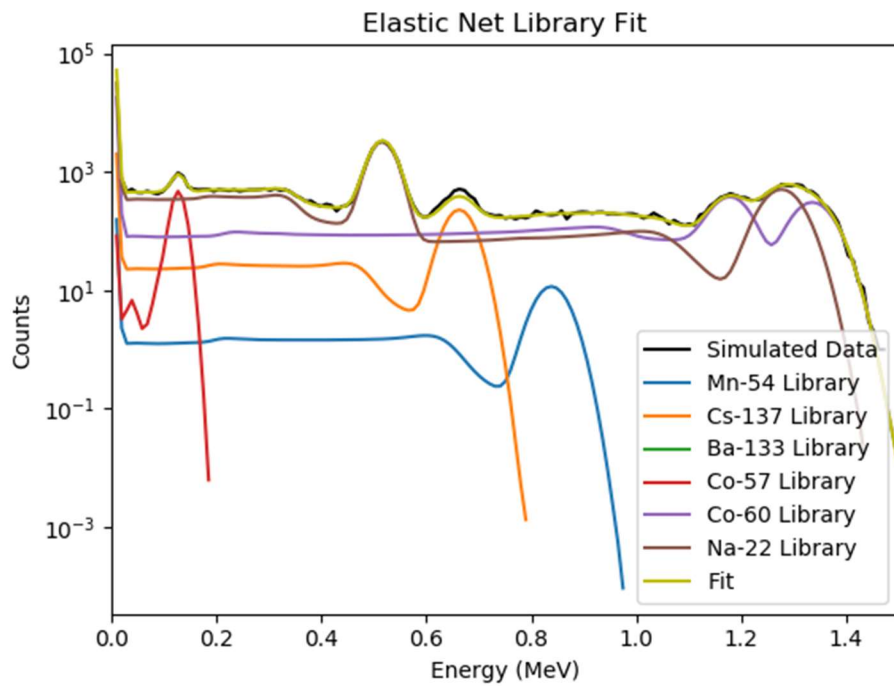


Figure 5-24: Elastic Net convolution with shielding medium count rate fit

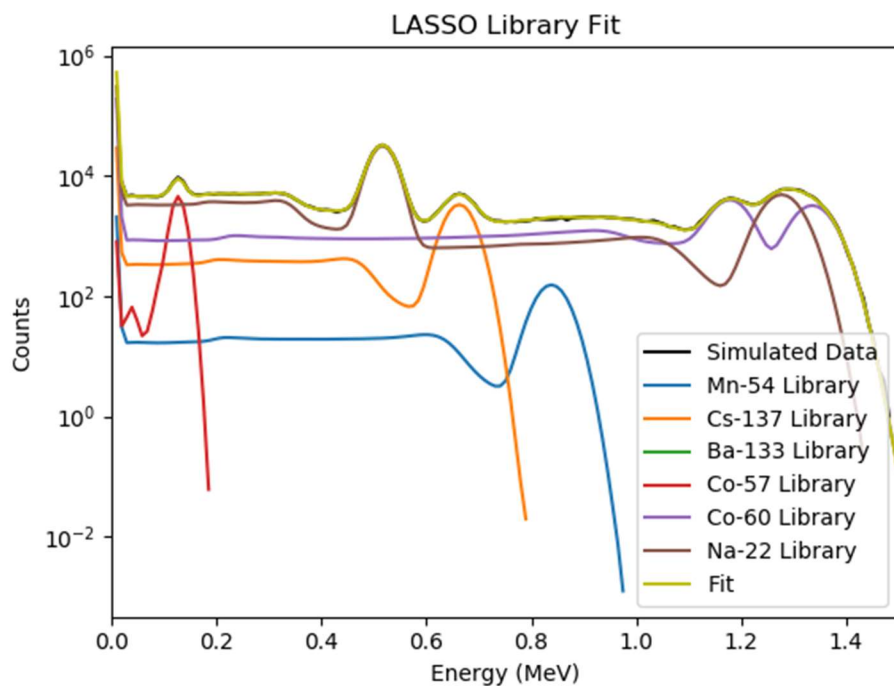


Figure 5-25: LASSO convolution with shielding high count rate fit

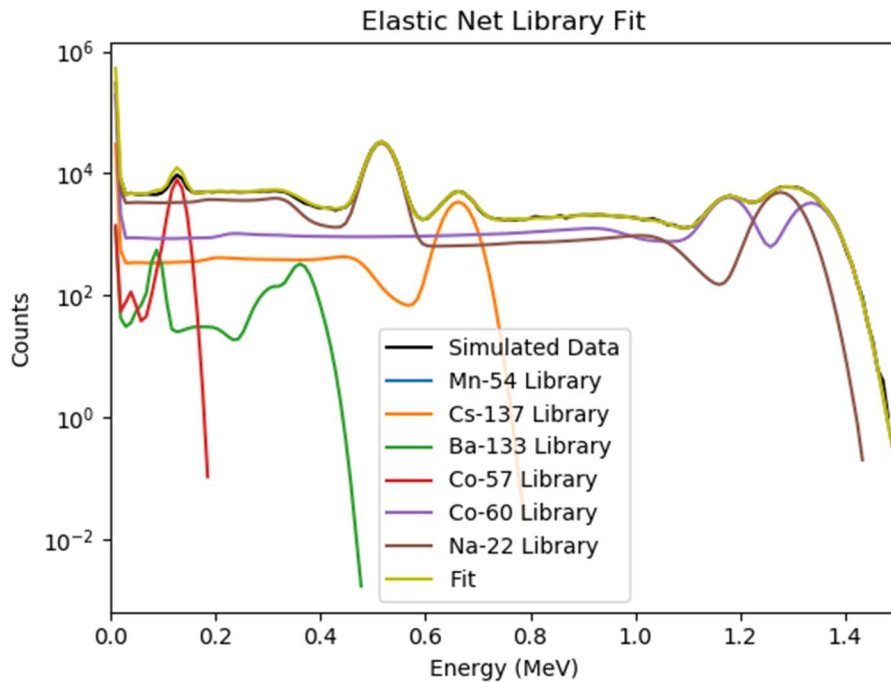


Figure 5-26: Elastic Net convolution with shielding high count rate fit

Table 5-8: Convolution with shielding trial prediction accuracy for LASSO and Elastic Net with varying count rates

	Convolution with Shielding Prediction Accuracy						
	Lasso-Low	EN-Low	Lasso-Med	EN-Med	LASSO-High	Elastic Net-High	
Ba-133	0.65	0.70	0.65	0.90	0.60	0.75	
Na-22	1.00	1.00	1.00	1.00	1.00	1.00	
Mn-54	0.70	0.60	0.50	0.45	0.50	0.50	
Cs-137	0.70	0.80	1.00	0.95	0.95	1.00	
Co-60	1.00	1.00	1.00	1.00	1.00	1.00	
Co-57	0.40	0.50	0.70	0.65	0.60	0.80	

The results demonstrate that each method is effective at accurately selecting the correct model for the convolved peak application. As the count rate is increased, LASSO and Elastic Net demonstrate an ability to decipher contributions of both Co-60 and Na-22 at 100% rate, with a false positive rate of 50%.

CHAPTER 6

Discussion and Conclusions

This dissertation takes a deep look into supervised machine learning variable selection techniques, LASSO and Elastic Net, and their use in advancing nuclear security related technologies. Oil well logging tools provide a soft target opportunity for bad characters to steal radioactive material for use in a dirty bomb. Using a D-T pulsed neutron generator and a digitizer, prompt and delayed detector responses can be obtained, providing a real time background suppression technique. With the background suppressed, it becomes possible to use LASSO and Elastic Net on-line for a real time analysis technique. LASSO and Elastic Net both show promise in the oil well logging application, with LASSO performing slightly better overall.

Several improvements can be made to the overall experiment moving forward. NaI scintillation detectors were used. More modern detectors, such as LaBr or CeBr offer a faster response time, improved resolution, and a higher density. Each of these properties will impact the overall count rate and distinct features for each code to interpret. Additionally, no measures were taken to accurately determine the make up of each of the materials. The research group at Kansas State University provided experimental data with labels of water, limestone, or sand with no additional information. Concentration values of different elements in each of these materials varies widely, as well as other characteristics such as density and porosity. An in-depth chemical analysis in the future would serve as a basis to truly determine the effectiveness of the variable selection and final fits.

Prior to the completion of this dissertation, several oil industry experts mentioned the need to improve cross sectional data for calcium. Some of the fitting issues with the limestone measurement can be attributed to poor cross-sectional data being fed into the simulations. Oil well companies correct the differences using semi-empirical fits of the sort the North Carolina State research group does not have access to.

LASSO and Elastic Net were also used to aim to improve on existing handheld radioisotope identification devices (RIIDs) used by first responders in field applications. Current RIID algorithms have difficulty in situations where clean peaks are not present such as masking and convolved peak cases. Once again, LASSO outperformed Elastic Net in almost every test run. As the count rate increased, the overall effectiveness of each method improved significantly. Even low concentrations of Co-57 were able to be detected at a rate greater than 50%.

Moving forward, LASSO should be considered for use in any radiation detection application that can be solved with linear methods. Elastic Net should also be considered for any application where there is high correlation between data. These methods have been demonstrated to be effective at correctly identifying model parameters that can improve the efficiency of oil well logging operators, potentially saving money and providing incentive to switch to the use of pulsed neutron generators.

REFERENCES

- A.Sood, R.P.Gardner / Nucl. Instr.and Meth.in Phys. Res.B 213 (2004) 100–104.
- Blackadar, J. et al. “Evaluation of commercial detectors.” INMM 44th Annual Meeting, Phoenix, Az, 2003. LA-UR-03-4020. Los Alamos National Laboratory.
- Bob Burkhart, “Neutron Generator and Well Logging”, Sandia National Laboratories, SAND2006-3291C, www.osti.gov/servlets/purl/1264595
- Burr, T and Hamada, M. “Radio-Isotope Identification Algorithms for NaI Gamma Spectra.” Algorithms 2009, 2, 339-360.
- Committee on Radiation Source and Replacement, 2008, Radiation Source Use and Replacement, National Research Council, ISBN 0-309-110115-7, National Academies Press, Washington, DC (NAS-2008)
- E. Bai, K. Chan, W. Eichinger, P. Kump, “Detection of radionuclides from weak and poorly resolved spectra using Lasso and subsampling techniques.” Radiation Measurements, 46 (2011), pp. 1138-1146.
- Evans, R.D., *The Atomic Nucleus*. McGraw-Hill, 1955.
- Friedman, J. et al., “Regularization paths for generalized linear models via coordinate descent.” Journal of Statistical Software (2010), Vol. 3, Issue 1.
- Gardner, et al., 2013, ANS Panel on “Recent Developments in Radiation Source Use and Replacement after the NAS Report of 2008”, Transactions of the American Nuclear Society, Vol. 109, 47.
- R.P. Gardner and A. Sood. “A Monte Carlo simulation approach for generating NaI detector response functions (DRFs) that accounts for non-linearity and variable flat continua”. *Nuclear Instruments and Methods in Physics Research, Section B: Beam Interactions with Materials and Atoms* (Jan. 2004), pp. 87-99.
- R.P. Gardner and C.W. Mayo. “NaI detector nonlinearity for PGNAA applications”. *Applied Radiation and Isotopes* 51.2 (Aug. 1999), pp. 189-195.
- R.P. Gardner and L. Xu. “Status of the monte carlo library least-squares (MCLLS) approach for non-linear radiation analyzer problems.” *Radiation Physics and Chemistry* 78 (2009), pp. 843-851.
- R.P. Gardner, et al. “NaI detector neutron activation spectra for PGNAA application.” *Applied Radiation Isotopes* (2000), 53, pp. 483-97.

Gauraha, N. "Introduction to the Lasso: a convex optimization approach for high-dimensional problems." *Resonance*, April 2018.

Guo, W. et al. "Using the Monte Carlo – Library Least Squares (MCLLS) approach for the in vivo XRF measurement of lead in bone." *Nuclear Instruments and Methods in Physics Research A*, 516 (2004), pp. 586-593.

Han, Xiaogang, Ph.D thesis. North Carolina State University. 2005.

Hastie, Trevor. *The Elements of Statistical Learning: Data Mining, Inference, and Prediction*. 2nd Edition. Springer Series in Statistics. 2009.

Hou, Guojing, Ph.D thesis. North Carolina State University. 2017.

Kim, K. et al. "Theoretical fluxes of gamma rays from the Martian surface." *Journal of Geophysical Research*, Vol. 111, 2006.

Knoll, G. F., *Radiation Detection and Measurement*. 4th Edition. John Wiley and Sons, Inc, 2011.

Kump, P. et at., "Variable selection via RIVAL (removing irrelevant variables amidst Lasso iterations) and its application to nuclear material detection." *Automatica*, 48 (2012), pp. 2107-2115.

Lberman, A.D et. al., "A method to determine the absolute neutron output of small D-T generator", *Nuclear Instruments and Methods in Physics Research Section B*, Volume 79, Issue 1-4, p. 574-578, June 1993

M. Geretschlager, Nucl. Instr. and Meth. B 28 (1987) 289.

MCNP Training Manual

Pibida, L. et al. "Evaluation of handheld radionuclide identifiers." *Journal of Research of the National Institute of Standards and Technology*. Vol 109, No 4, 2004.

Preston R.M. et al, "Neutron generator burst timing measured using a pulse shape discrimination plastic scintillator with silicon photomultiplier readout", *Journal of Instrumentation*, December 8, 2013.

R.P. Gardner, A.M. Yacout, J. Zhang, K. Verghese, Nucl. Instr. and Meth. A 242 (1986) 399.

R.L. Heath, Scintillation Spectrometry, Gamma-Ray Spectrum Catalogue, 2nd Ed., USAEC Report IDO-16880, 1964.

T. Papp, J.L. Campbell, D. Varga, G. Kalinka, Nucl. Instr. and Meth. A 412 (1998) 109.

Serra, Oberto. *Well Logging Handbook*. Ed. Technip, Paris. 2008.

Tibshirani, R. "Regression shrinkage and selection via the lasso." *Journal of the Royal Statistical Society, Series B* 58: 267-288. 1996.

Wu, T. and Lange, K. "Coordinate descent algorithms for Lasso penalized regression." *The Annals of Applied Statistics*, 2008, Vol. 2, No. 1, pp. 224-244.

Y. Jin, R.P. Gardner, K. Verghese, *Nucl. Instr. and Meth. A* 242 (1986) 416.

Yang, Y. and Zou, H. "A coordinate majorization descent algorithm for ℓ_1 penalized learning." *Journal of Statistical Computation and Simulation*. (2014) 84, pp. 84-95.

Zou, H. and Hastie, T. "Regularization and variable selection via the elastic net". *Journal of the Royal Statistical Society Series B*. 67: 301-320. 2005.

Appendix A: MCNP Sample Deck – KSU Application

Room 207 - Salt Water simulation

c

c ----- Cell Cards

c Detectors

```
20 37 -0.00276 -30 imp:n,p=1 $ BF-3 detector 1
21 39 -3.67 -31 imp:n,p=1 $ NaI detector 1
22 38 -0.2677 -32 imp:n,p=1 $ Helium-3 detector 2
23 39 -3.67 -33 imp:n,p=1 $ NaI detector 2
24 30 -11.34 -34 imp:n,p=1 $ Lead Shield, 2 inches
130 6 -0.998207 -115 118 -230 113 imp:n,p=1 $ inside Shell 1
131 6 -0.998207 -115 230 -231 113 imp:n,p=1 $ inside Shell 2
132 6 -0.998207 -115 231 -232 113 imp:n,p=1 $ inside Shell 3
133 6 -0.998207 -115 232 -233 113 imp:n,p=1 $ inside Shell 4
134 6 -0.998207 -115 233 -234 113 imp:n,p=1 $ inside Shell 5
```

c BEE chamber

```
105 0 -40 114 116 113 120 imp:n,p=1 $ room air
106 1 -2.35 40 -41 101 102 103 110 111 112 113 114 imp:n,p=1 $ room walls
107 1 -2.35 -116 115 118 imp:n,p=1 $ BEE walls
108 6 -0.998207 -115 234 113 imp:n,p=1 $ inside BEE
109 5 -2.7 -118 117 imp:n,p=1 $ borehole pipe
110 0 -117 119 #20 #21 #22 #23 #24 imp:n,p=1 $ inside borehole
99 0 41 -99 104 105 106 121 imp:n,p=1 $ void
```

c doors and door shields

```
120 0 -112 imp:n,p=1 $ inner door void
121 0 -110 imp:n,p=1 $ outer door void
122 0 -111 imp:n,p=1 $ outer door plug
123 3 -1.00 -113 118 imp:n,p=1 $ inner wall shield (12 in)
124 3 -1.00 -119 imp:n,p=1 $ inside borehole shield (11 in)
125 3 -1.00 -114 imp:n,p=1 $ inner door shield (2 in)
126 3 -1.00 -120 imp:n,p=1 $ outer door shield (2 in)
127 3 -1.00 -121 imp:n,p=1 $ top wall shield (5 in)
```

c roof voids and shields

```
31 0 -101 imp:n,p=1 $ roof void 1
32 0 -102 imp:n,p=1 $ roof void 2
33 0 -103 imp:n,p=1 $ roof void 3
34 3 -1.00 -104 imp:n,p=1 $ skylight 1 shield
35 3 -1.00 -105 imp:n,p=1 $ skylight 2 shield
36 3 -1.00 -106 imp:n,p=1 $ skylight 3 shield
100 0 99 imp:n,p=0 $ graveyard
```

c ----- Surface Cards

c -- detectors

```
30 rcc -25.5 53.34 -12.7 15 0 0 1.9 $ BF3, OD 1.5"
31 rcc -50.5 53.34 -12.7 7.5 0 0 3.81 $ NaI, OD 3"
```

32 rcc -85.5 53.34 -12.7 15 0 0 1.9 \$ He3, OD 1.5"
 33 rcc -110.5 53.34 -12.7 7.5 0 0 3.81 \$ NaI, OD 3"
 34 RPP 8.5 13.58 49.84 56.84 -16.2 -9.2 \$ Pb Block
 c -- Barriers
 40 RPP -152.40 396.24 -426.72 152.40 -114.30 193.04 \$inside room
 41 RPP -182.88 441.96 -457.20 182.88 -175.26 223.52 \$outside room
 c
 c -- roof voids
 101 RPP -152.40 396.24 30.48 152.40 193.04 223.52 \$ skylight void 1
 102 RPP -152.40 396.24 -175.26 -53.34 193.04 223.52 \$ skylight void 2
 103 RPP -152.40 396.24 -381.00 -259.08 193.04 223.52 \$ skylight void 3
 c -- roof shields
 104 RPP -167.64 411.48 15.24 167.64 223.52 238.76 \$ 6" poly over 1
 105 RPP -167.64 411.48 -190.5 -38.1 223.52 238.76 \$ 6" poly over 2
 106 RPP -167.64 411.48 -396.24 -243.84 223.52 238.76 \$ 6" poly over 3
 c -- doors and door shields
 110 RPP 421.64 441.96 -188.54 -85.72 -114.30 99.06 \$ outer door void
 111 RPP 396.24 421.64 -188.54 -85.72 -114.30 99.06 \$ outer door plug
 112 RPP -182.88 -152.40 -188.54 -85.72 -114.30 99.06 \$ inner door void
 113 RPP -152.40 -121.92 7.62 99.06 -114.30 129.54 \$ inner wall shield
 114 RPP -152.40 -147.32 -198.12 -76.20 -114.30 129.54 \$ inner door shield
 120 RPP 391.16 396.24 -198.12 -76.20 -114.30 129.54 \$ outer door shield
 121 RPP -35.56 86.36 182.88 195.58 -114.30 129.54 \$ top wall shield
 c -- enclosure walls
 115 RPP -152.4 91.44 -45.72 152.4 -114.30 88.90 \$ inside BEE walls
 116 RPP -152.4 111.76 -66.04 152.4 -114.30 88.90 \$ outside BEE walls
 c -- borehole pipe
 117 RCC -152.4 53.34 -12.7 264.16 0 0 10.16 \$ inside borehole
 118 RCC -152.4 53.34 -12.7 264.16 0 0 10.80 \$ outside borehole
 119 RCC -152.4 53.34 -12.7 27.94 0 0 10.16 \$ shielding inside borehole
 99 SO 800 \$ problem boundary
 c -- tally surfaces
 230 C/X 53.34 -12.7 20.80 \$Shell 1
 231 C/X 53.34 -12.7 30.80 \$Shell 2
 232 C/X 53.34 -12.7 40.80 \$Shell 3
 233 C/X 53.34 -12.7 50.80 \$Shell 4
 234 C/X 53.34 -12.7 60.80 \$Shell 5

 c ----- DATA CARDS
 SDEF par=n erg=14 POS 25.4 53.34 -12.7 WGT=12653259
 ACT FISSION=none NONFISS=ALL
 PHYS:N 6j 3
 PHYS:p 100 0 0 0 0 j 0
 CUT:N 2j 0
 c
 c ctme 4400

nps 50000000
 mode n p
 c
 c --- NEUTRON TALLIES
 f12:n 118.1 230 231 232 233 234
 sd12 14478 27884 41289 54695 68101 81507
 f22:n 118.1 230 231 232 233 234
 sd22 1 1 1 1 1 1
 c --- BF3 Near
 f28:N 20
 E28 0 2046i 10
 c --- He3 Far
 f38:N 22
 E38 0 2046i 10
 c --- NaI Near
 f68:P 21
 E68 0 2046i 10
 c --- NaI Far
 f78:P 23
 E78 0 2046i 10
 c
 c -----
 c NBS Concrete (density = 2.35 g/cm^3)
 c -----
 m1 1001.60c -0.0056 \$ hydrogen
 16032.60c -0.0012 \$ sulfur
 8016.60c -0.4983 \$ oxygen
 14000.60c -0.3158 \$ silicon
 13027.60c -0.0456 \$ aluminum
 26000.55c -0.0122 \$ iron
 20000.60c -0.0826 \$ calcium
 19000.60c -0.0192 \$ potassium
 11023.60c -0.0171 \$ sodium
 12000.60c -0.0024 \$ magnesium
 c
 c *****
 c AIR: ANSI/ANS-6.4.3, Dry air; density = 0.0012 g/cm^3
 c Composition by mass fraction
 c *****
 m2 7014.60c -.75519
 8016.60c -.23179
 6000.60c -.00014
 18000.35c -.01288
 c
 c -----
 c material: borated polyethylene d=1.00 g/cm^3 CH2 + 8 wt% B4C

c B-11 5.029; B-10 1.234; C 80.595; H 13.143

c -----

m3 1001.60c -0.13143

5010.60c -0.01234

5011.60c -0.05029

6000.60c -0.80594

c

c -----

c material: polyethylene d=0.95 g/cm^3 CH2

c -----

m4 1001.60c 2

6000.60c 1

c

c -----

c material: aluminum 6061; density=2.7 g/cm^3

c -----

m5 12000 -0.01000 \$ Mg

13027 -0.97200 \$ Al

14000 -0.00600 \$ Si

22000 -0.00088 \$ Ti

24000 -0.00195 \$ Cr

25055 -0.00088 \$ Mn

26000 -0.00409 \$ Fe

29000 -0.00275 \$ Cu

30000 -0.00146 \$ Zn

c -----

c water; density = 0.998207 g/cm^3

c ---

m6 1001.60c 2

8016.60c 1

c -----

c salt water, 0.9%; density = 1.00875 g/cm^3

c ---

m7 1001.60c -0.1101992

8016.60c -0.8801130

11023.60c -0.0035084

17035.70c -0.0041186

17037.70c -0.0013729

c -----

c salt water, 1.8%; density = 1.00875 g/cm^3

c ---

m8 1001.60c -0.1091984

8016.60c -0.8721200

11023.60c -0.0070168

17035.70c -0.0082372

17037.70c -0.0027458

c -----
c salt water, 2.7%; density = 1.00875 g/cm^3
c ---
m9 1001.60c -0.1081111
8016.60c -0.8648888
11023.60c -0.0105252
17035.70c -0.0123561
17037.70c -0.0041187

c -----
c salt water, 3.6%; density = 1.00875 g/cm^3
c ---
m10 1001.60c -0.1071111
8016.60c -0.8568888
11023.60c -0.0140339
17035.70c -0.0164746
17037.70c -0.0054915

c -----
c Sodium; density -0.97
c ---
m11 11000 -0.97

c -----
c Chlorine; density -1.5625
c ---
m12 17000 -1.5625

c -----
c ---- Lead, Inert: Density (11.34 g/cm3)
m30 82000 -1.000000 \$ He

c -----
c ---- BF-3, Proportional: Density (0.00276 g/cm3)
m37 5000 1 \$ B
9000 3 \$ F

c -----
c -----
c ---- Helium-3, Proportional: Density (0.2677 g/cm3)
m38 2003 -1.000000 \$ He

c -----
c ----- NaI Crystal: Density (3.67 g/cm3)
m39 11023.60c 0.500 \$ Na
53127 0.500 \$ I

c -----
c ----- Nickel Additive: Density (8.908 g/cm3)-----
m40 28058.60c -0.68077
28060.60c -0.26223
28061.60c -0.01139
28062.60c -0.03635

28064.60c -0.00926

Appendix B: LASSO Code Sample

```

import pandas as pd
import numpy as np
from numpy import array
import matplotlib.pyplot as plt
from sklearn.model_selection import train_test_split
from sklearn.preprocessing import scale
from sklearn.linear_model import Lasso, LassoCV
from sklearn.metrics import mean_squared_error

libraries = pd.read_csv("NearExplibraries.csv")
target = pd.read_csv("waternearinterp.csv")
energy = pd.read_csv("Energy.csv")

X = libraries[200:1500]
y = target.y[200:1500]
originalenergy = energy[200:1500]

X_train, X_test, y_train, y_test = train_test_split(X, y, test_size=.90)
alphas = 10**np.linspace(6,-2,1000)*.5
lassocv = LassoCV(alphas=None, cv=10, max_iter=100000, normalize=True,
positive=False)
model = lassocv.fit(X_train, y_train)

m_log_alphas = -np.log10(model.alphas_)

plt.figure()

plt.plot(m_log_alphas, np.log10(model.mse_path_), ':')
plt.plot(m_log_alphas, np.log10(model.mse_path_.mean(axis=-1)), 'k', label='Average
across the folds', linewidth=2)
plt.axvline(-np.log10(model.alpha_), linestyle='--', color='k', label='alpha: CV estimate')
plt.legend()
plt.xlabel('-log(alpha)')
plt.ylabel('Mean square error')
plt.title('Mean square error on each fold: coordinate descent')
plt.axis('tight')
plt.show()

lasso = Lasso(max_iter=10000, normalize=True, positive=True)
coefs = []

for a in alphas:

```

```

lasso.set_params(alpha=a)
lasso.fit(scale(X_train), y_train)
coefs.append(lasso.coef_)

label_list=['Sand Near', 'Water Near', 'Limestone Near', 'Iron', 'Copper']
ax = plt.gca()
lineObjects = ax.plot(alphas*2, coefs)
ax.set_xscale('log')
plt.ticklabel_format(axis='y', style='sci', scilimits=(0,0))
plt.locator_params(axis='y', nbins=10)
"""

plt.xlabel('Alpha')
plt.ylabel('Coefficients')
plt.axvline(model.alpha_, linestyle='--', color='k', label='alpha: CV estimate')
plt.title('Optimal Alpha Parameters')
plt.legend(iter(lineObjects), label_list)
plt.show()

lasso.set_params(alpha=lassocv.alpha_)
lasso.fit(X_train, y_train)
mean_squared_error(y_test, lasso.predict(X_test))
print("Best for alphas:")
print(lassocv.alpha_)
"""

print("Best 11-ratio:")
print(lasso.l1_ratio)
"""

print("Coefficients:")
print(pd.Series(lasso.coef_, index=X.columns))
print(mean_squared_error(y_test, lasso.predict(X_test)))
fit = lasso.coef_*X
total = lasso.coef_*libraries
comb = fit.Water_Near + fit.Sand_Near + fit.Limestone_Near + fit.Iron + fit.Copper
full = total.Water_Near + total.Sand_Near + total.Limestone_Near + total.Iron +
total.Copper

plt.semilogy(originalenergy, y, 'k', label='KSU Experimental Data')
plt.semilogy(originalenergy, fit.Water_Near, label='Water Library')
plt.semilogy(originalenergy, fit.Sand_Near, label='Sand Library')
plt.semilogy(originalenergy, fit.Limestone_Near, label='Limestone Library')
plt.semilogy(originalenergy, fit.Iron, label='Iron Library')
plt.semilogy(originalenergy, fit.Copper, label='Copper Library')
plt.semilogy(originalenergy, comb, label='Fit')
plt.legend()

```

```
plt.xlabel('Energy (MeV)')  
plt.ylabel('Counts')  
plt.title('LASSO Library Fit')  
plt.show()  
  
plt.semilogy(energy, target.y, 'k', label='KSU Experimental Data')  
plt.semilogy(energy, total.Water_Near, label='Water Near Library')  
plt.semilogy(energy, total.Sand_Near, label='Sand Near Library')  
plt.semilogy(energy, total.Limestone_Near, label='Limestone Near Library')  
plt.semilogy(energy, total.Iron, label='Iron Library')  
plt.semilogy(energy, total.Copper, label='Copper Library')  
plt.semilogy(energy, full, label='Fit')  
  
plt.legend()  
plt.xlabel('Energy (MeV)')  
plt.ylabel('Counts')  
plt.title('LASSO Library Fit')  
plt.show()
```

Appendix C: Elastic Net Code Sample

```

import pandas as pd
import numpy as np
from numpy import array
import matplotlib.pyplot as plt
from sklearn.model_selection import train_test_split
from sklearn.preprocessing import scale
from sklearn.linear_model import Lasso, LassoCV, ElasticNet, ElasticNetCV,
lasso_path, enet_path
from sklearn.metrics import mean_squared_error
import pylab as pl

libraries = pd.read_csv("NearExplibraries.csv")
target = pd.read_csv("waternearinterp.csv")
energy = pd.read_csv("Energy.csv")

X = libraries[200:1500]
y = target.y[200:1500]
originalenergy = energy[200:1500]

X_train, X_test, y_train, y_test = train_test_split(X, y, test_size=.90)
coefs = []
alphas = 10**np.linspace(10,-2,100)*.5

en = ElasticNetCV(l1_ratio=.99, alphas=None, cv=10, max_iter=100000,
normalize=True, positive=True)
en.fit(X_train, y_train)
ElasticNet = ElasticNet(l1_ratio=.99,max_iter=10000, normalize=True, positive=True)
# Display results
model = en.fit(X_train, y_train)
m_log_alphas = -np.log10(model.alphas_)

plt.figure()
plt.plot(m_log_alphas, np.log10(model.mse_path_), ':')
plt.plot(m_log_alphas, np.log10(model.mse_path_.mean(axis=-1)), 'k', label='Average
across the folds', linewidth=2)
plt.axvline(-np.log10(model.alpha_), linestyle='--', color='k',label='alpha: CV estimate')
plt.legend()
plt.xlabel('-log(alpha)')
plt.ylabel('Mean square error')
plt.title('Mean square error on each fold: coordinate descent')
plt.axis('tight')
plt.show()

```

```

for a in alphas:
    ElasticNet.set_params(alpha=a)
    ElasticNet.fit(scale(X_train), y_train)
    coefs.append(ElasticNet.coef_)

label_list=['Sand Library', 'Water Library', 'Limestone Library', 'Iron Library', 'Copper
Library']
ax = plt.gca()
lineObjects = ax.plot(alphas, coefs)
ax.set_xscale('log')
plt.ticklabel_format(axis='y', style='sci', scilimits=(0,0))
plt.axvline(en.alpha_, linestyle='--', color='k', label='alpha: CV estimate')
plt.locator_params(axis='y', nbins=10)
"""

"""

plt.xlabel('Alpha')
plt.ylabel('Coefficients')
plt.title('Optimal Alpha Parameters')
plt.legend(iter(lineObjects), label_list)
plt.show()
print("Best for alphas:")
print(en.alpha_)
print("Best l1-ratio:")
print(en.l1_ratio_)
print("Coefficients:")
print(pd.Series(en.coef_, index=X.columns))

#evaluate
y_pred = en.predict(X_test)
test_score = mean_squared_error(y_test, y_pred)
print(test_score)

fit = en.coef_*X
total = en.coef_*libraries
comb = fit.Water_Near + fit.Sand_Near + fit.Limestone_Near + fit.Iron + fit.Copper
full = total.Water_Near + total.Sand_Near + total.Limestone_Near + total.Iron +
total.Copper

plt.semilogy(originalenergy, y, 'k', label='KSU Experimental Data')
plt.semilogy(originalenergy, fit.Water_Near, label='Water Library')
plt.semilogy(originalenergy, fit.Sand_Near, label='Sand Library')
plt.semilogy(originalenergy, fit.Limestone_Near, label='Limestone Library')
plt.semilogy(originalenergy, fit.Iron, label='Iron Library')
plt.semilogy(originalenergy, fit.Copper, label='Copper Library')

```

```
plt.semilogy(originalenergy, comb, label='Fit')
plt.legend()
plt.xlabel('Energy (MeV)')
plt.ylabel('Counts')
plt.title('Elastic Net Library Fit')
plt.show()

plt.semilogy(energy, target.y, 'k', label='KSU Experimental Data')
plt.semilogy(energy, total.Water_Near, label='Water Near Library')
plt.semilogy(energy, total.Sand_Near, label='Sand Near Library')
plt.semilogy(energy, total.Limestone_Near, label='Limestone Near Library')
plt.semilogy(energy, total.Iron, label='Iron Library')
plt.semilogy(energy, total.Copper, label='Copper Library')
plt.semilogy(energy, full, label='Fit')

plt.legend()
plt.xlabel('Energy (MeV)')
plt.ylabel('Counts')
plt.title('Elastic Net Library Fit')
plt.show()
```